공학박사 학위논문

# Tailor-made design of complex concentrated alloys

## 컴플렉스 고용 합금의 특성 맞춤형 합금 설계법 개발

2018 년 2 월

서울대학교 대학원

재료공학부

오 현 석

# Abstract

## Tailor-made design of complex concentrated alloys

Hyun Seok Oh

Department of Materials Science and Engineering

College of Engineering

Seoul National University

Complex concentrated alloys (CCAs; CCAs that have more than four elements are also referred to as high entropy alloys) are a new alloy development philosophy in which the base alloy has a significant fraction of multiple principal elements. CCAs have attracted worldwide attention as strong candidates to solve problems owing to their useful performances, such as superior mechanical properties at all temperature ranges and good irradiation resistance.

Much of the interest in CCAs stems from the belief that the atomic-level complexity, which originates from the large number of principal elements would provide profound effects, such as the lattice distortion effect, the sluggish diffusion effect, the irradiation resistance, and the solid-solution strengthening. However, the correlation between the complexity and the resultant properties has not yet been thoroughly understood. As a result, the advantage of so many degrees of freedom for alloy design of CCAs is diminished by a lack of mixing rules, rendering alloy design an empirical try-and-error undertaking. Therefore, to make a useful guide for the new CCA designs, a simple parameter is required to reflect the atomic environments of CCAs in a physically meaningful way so that they can be directly related to

properties.

In CCAs, all constituent elements are solute and solvent, and every element interacts with the stress field of dislocations, thereby increasing or decreasing the elastic strain energy of the system and resulting in solid-solution strengthening. Thus, the solid-solution strengthening effect is one of the representative phenomena that reflect atomic-level complexity in CCAs, which can also be related to macroscopic mechanical and functional properties influenced by the complexity. In this thesis, the relationship between atomic-level complexity and its influence on properties, in particular solid-solution strengthening, is investigated. CCAs with face-centered cubic (FCC) phase consisting of late 3d transition metal elements (i.e., V, Cr, Mn, Fe, Co, and Ni) are mainly discussed (Here we call them 3d CCAs). These alloys have been considered to have outstanding mechanical properties, and some commercial alloys, such as austenitic steels and $\gamma$ matrix of a superalloy, belong to this group, which implies a high possibility of new commercial alloys.

First, we analyzed the local atomic structure of 3d CCAs by X-ray Diffraction (XRD) and Extended X-ray Absorption Fine Structure (EXAFS) to measure the elemental average atomic sizes of consisting elements. From the obtained structural information, we predicted the solid-solution strengths by applying the atomic size difference among the constituting elements to the existing model on the basis of elasticity theory. However, the predicted solid-solution strengths do not match well with the experimentally measured values. In order to interpret this mismatch, we calculated the atomic structure using density function theory (DFT) and found that the fluctuation of bond lengths due to the dissimilar local atomic configurations, which is usually ignored for dilute alloys, has a significant impact on the solid-solution strengthening of CCAs, which introduces higher degree of complexity

problem in CCAs.

As a second approach, we calculated the atomic-level pressure of each element in 3d CCAs, which is the cause of solid-solution strengthening, using DFT calculation. We found that the atomic-level pressure of individual atoms originates from the charge transfer between a center atom and its surrounding atoms. This was also confirmed with an experimental study by measuring volume strain of each element in 3d CCAs using EXAFS and plotting with charge transfer. This means that the atomic-level pressure in 3d CCAs is attributed to the electronic effect rather than the elastic interaction of constituent elements.

In order to utilize this concept for an alloy design strategy, we tried descending the degree of complexities in 3d CCAs. Through a statistical approach, we found that both values of 'deviation of average elemental atomic-level pressure' and 'deviation of atomic-level pressure due to the variance in local atomic configurations' are linearly proportional to each other. This makes it possible to estimate a higher degree complexity (configurational deviations) using a lower degree complexity (elemental deviations), which can be identified experimentally. As a result, we were able to theoretically explain the proportional relationship between electronegativity difference and solid-solution strengths in the 3d CCAs.

Based on the aforementioned discussion, we constructed an electronegativity-mixing entropy diagram that shows the relationship between chemical complexity and complexity induced by deviation of atomic-level pressure, i.e., solid-solution strengthening. All possible combinations of 3d transition metal elements (V, Cr, Mn, Fe, Co, Ni) are included in the diagram. The area of the 3d CCAs has inverse C-shape boundary, which means that (1) the mixing entropy does not have a strong correlation with solid-solution strengthening, and (2) there is a region where the

mixing entropy should be decreased to obtain greater solid-solution strengthening effects. Thus, we concluded that there is no strong correlation between the chemical complexity and the deviation (i.e. complexity) of atomic-level pressure in 3d CCAs.

One may argue that the chemical complexity is no longer important for CCAs as the complexity of atomic-level pressure are closely related to the lattice distortion effect and the sluggish diffusion effect, which are CCA's two 'core effects' among the four. Changing the composition from the Cantor alloy, we developed twin-induced plasticity (TWIP) and transformation-induced plasticity (TRIP) CCAs by decreasing stacking fault energies while maintaining the deviation of atomic-level pressure, i.e., solid-solution strength, in order to show that there are many factors that we can manipulate besides complexity of atomic-level pressure. The change of deformation mechanisms from dislocation gliding to TWIP and TRIP increases the strain hardening rate of the CCAs, enhancing both ultimate tensile strength and the percentage of uniform elongation without loss of yield strengths. The development of these new CCAs was possible due to the freedom in manipulating composition, which implies that chemical complexity is also important for the design of new CCAs for the vastness of composition space.

Additionally, we discussed asymmetry of atomic-level pressure-induced element-specific properties in CCAs. Atomic-level pressure of an element includes the information of anharmonicity of lattice potential and represents the resistance of it against displacement. As a result, element-specific properties, such as atomic displacements, diffusivity, and preferential site of interstitial elements show asymmetric behavior upon atomic-level pressure. Consequently, the deviation of atomic-level pressure dominantly affects the degree of lattice distortion, the diffusivity of substitutional elements, and the solubility of interstitial elements,

which are crucial for engineering applications.

Through this research, we distinguished the previous concept of complexity in CCAs into two categories: chemical complexity for the vastness of composition space and complexity of atomic-level pressure reflecting fluctuation of lattice potential energies. We believe that the tailor-made design of CCAs is possible when both complexities are investigated well for the desired elemental combinations.

**Keyword:** Complex concentrated alloy, Solid-solution strengthening, Atomic-level pressure, Chemical complexity, Electronegativity, Stacking fault energy

**Student Number:** 2012-24162

# Table of Contents

# List of Figures

# List of Tables

# List of Abbreviations

| | |
|---|---|
| APT | Atom Probe Tomography |
| BCC | Body Centered Cubic |
| BSE | Backscattered Electron |
| CCA | Complex Concentrated Alloy |
| DFT | Density Function Theory |
| EBSD | Electron Backscatter Diffraction |
| ECCI | Electron Channeling Contrast Imaging |
| EDM | Electrical Discharge Machining |
| EDS | Energy Dispersive X-ray Spectroscopy |
| EXAFS | Extended X-ray Absorption Fine Structure |
| FCC | Face Centered Cubic |
| FIB | Focused Ion Beam |
| FWHM | Full Width Half Maximum |
| HCP | Hexagonal Close Packed |
| HEA | High Entropy Alloy |
| IM | Intermetallic |
| IPF | Inverse Pole Figure |
| KAM | Kernal Average Misorientation |
| LPE | Lattice Potential Energy |
| MEPP | Maximum Entropy Production Principle |
| MSAD | Mean Squared Atomic Displacement |
| PDF | Pair Distribution Function |
| pRDF | Pseudo Radial Distribution Function |

| | |
|---|---|
| RDF | Radial Distribution Function |
| SEM | Scanning Electron Microscopy |
| SFE | Stacking Fault Energy |
| SS | Solid Solution |
| STS | Stainless Steel |
| TRIP | Transformation Induced Plasticity |
| TWIP | Twin Induced Plasticity |
| UTS | Ultimate Tensile Strength |
| VEC | Valence Electron Concentration |
| XRD | X-ray Diffraction |

# List of Symbols

| | |
|---|---|
| $a$ | Lattice constant of solid solution |
| $a_0$ | Lattice constant of pure host element |
| $B$ | Bulk modulus |
| $C_{el}$ | Charge transfer of center element |
| $c$ | Solute concentration |
| $c_i$ | Composition if ith element |
| $c_n$ | Concentration of nth element |
| $d$ | Interatomic distance between a solute B atom and a solvent A atom in A-B solution |
| $d$ | Partial spacing |
| $d_0$ | Interatomic distance in pure A atom |
| $E_{ela}$ | Elastic strain energy |
| $E_l$ | Solute/dislocation interaction energy |
| $E_t$ | Total energy of the system |
| $f(x_i, y_i)$ | Dimensionless pressure field |
| $f_1(w_c)$ | Dislocation core structure |
| $G$ | Gibbs free energy |
| $H$ | Fusing enthalpy |
| $i, j, k, l, m, n$ | The number of the elements near the center atom |
| $K$ | Correction factor of lattice parameter |
| $P$ | Atomic-level pressure |
| $P_{dis}$ | Pressure field of the dislocation at the solute site |
| $P_i$ | Atomic-level pressure of atom i |

| | |
|---|---|
| $P_{ij}$ | Local atomic-level pressure of an element i at atomic site j |
| $P_{sol}$ | Pressure field of the solute atom at the dislocation |
| $R$ | Gas constant |
| $R_0$ | Metallic radius of a pure element |
| $r$ | Effective atomic radius |
| $r_a$ | Average atomic radius of solvent |
| $r_{ij}$ | Interatomic distance between atom i and j |
| $S$ | Mixing entropy |
| $S_{conf}$ | Configurational entropy of mixing |
| $T$ | Temperature |
| $T^{2nd}$ | Second phase formation temperature |
| $T^{s}$ | Solidus temperature |
| $T_m$ | Melting temperature |
| $V$ | Central force potential |
| $V_h$ | Volume of a spherical hole |
| $V_{s,f}$ | Volume of a solute after relaxation |
| $V_{s,i}$ | Initial volume of a spherical inclusion |
| $\bar{V}$ | Effective atomic volume |
| $\overline{V_n}$ | Volume of element in the alloy |
| $x_n$ | Composition of nth component |
| $x_i$ | Atom fraction of element i |
| $\alpha$ | Coordinate of a solute atom relative to the dislocation |
| $\alpha$ | Line tension parameter |
| $\Gamma$ | Stacking fault energy |

| | |
|---|---|
| $\gamma$ | Eshelby constant |
| $\Delta G^{\gamma \to \alpha}$ | Molar gibbs energy of $\gamma$-austenite to $\varepsilon$-martensite |
| $\Delta V_{dis}$ | Misfit volume of the dislocation at the solute site |
| $\Delta V_{sol}$ | Misfit volume of the solute atom at this site |
| $\Delta \bar{V}$ | Average misfit volume of the solute |
| $\Delta S_{mix}$ | Mixing entropy |
| $\Delta \sigma_{fr}$ | Frictional stress |
| $\Delta \sigma_{gb}$ | Grain boundary strengthening |
| $\Delta \sigma_{ppt}$ | Precipitation hardening |
| $\Delta \sigma_{ss}$ | Solid solution strengthening |
| $\Delta \sigma_{\rho_i}$ | Initial dislocation density |
| $\Delta \chi_{Allen}$ | Electron negativity difference between consisting elements |
| $\delta$ | Misfit parameter |
| $\epsilon$ | Size misfit factor of solute |
| $\varepsilon_u$ | Ultimate tensile strain |
| $\varepsilon_{\alpha\beta}$ | Applied strain |
| $\varepsilon_v$ | Atomic volume strain |
| $\lambda$ | Slip distance in the dislocation |
| $\mu(E)$ | Element-resolved absorption |
| $\nu$ | Poisson's ratio |
| $\rho$ | Molar surface density along (1 1 1) planes |
| $\sigma^2_{\Delta V_n}$ | Variance of misfit volume of solute atom according to the local environment |
| $\sigma^{\gamma/\varepsilon}$ | Interfacial energy of $\gamma$ and $\varepsilon$ phase boundary |

| | |
|---|---|
| $\sigma_i^{\alpha\beta}$ | Stress tensor at atom i |
| $\sigma_u$ | Ultimate tensile strength |
| $\Phi_1$ | Total stress in the system |
| $\chi_{ith}$ | Electronegativity of ith element |
| $\bar{\chi}$ | Average electronegativity |
| $\Omega_B^*$ | Atomic volume of solute B obtained by the linear extrapolation of the volume plot to 100% solute B |
| $\Omega_A$ | Atomic volume of solvent A |
| $\Omega_i$ | Atomic volume of the ith atom |
| $\Omega_{sf}$ | Volume size factor |

# Chapter 1. Introduction

## 1.1. Complex concentrated alloy: a new philosophy of alloy design

Metallic alloys are humankind's most important materials for manufacturing and multiple products in the fields of transportation, energy, safety, and infrastructure for thousands of years owing to their excellent strength and damage tolerance. Historically, metallurgists have developed new metallic alloys such as bronze and steels by combining a base metal element with small amounts of one or more solute elements to achieve desirable engineering properties, such as strength and ductility. The underlying philosophy in this traditional alloy design is "modifying" the mechanical and functional properties of base elements by adding small amounts of solute elements.

During the last century, the number and amount of alloying elements, i.e., chemical complexity, in newly developed alloys have drastically increased to improve the performances in order to address the demands of rapidly developing industries (Figure 1.1.A, Table 1.1). Such alloys are characterized by multi-functionality and excellent performances upon various applications, ranging from lightweight Al alloys (ex. aircraft aluminum) for aircraft to high-temperature strength Ni-based superalloys (ex. Inconel series) for turbine blades.

Recently, a new alloy development philosophy, which is so-called high entropy alloy (HEA), was proposed where the base alloy contains multiple principal elements (≥4) with nearly equiatomic concentrations being between 35 and 5 at.% [1, 2]. HEAs have been reported to have useful performances including high toughness [3, 4], corrosion resistance [5], high-temperature strength [6, 7], as well

as a good irradiation resistance [8-11]. In addition, the concept of HEAs shifts the focus away from the corners of alloy phase diagrams toward their centers [12], vastly increasing the number of possible alloy systems with new and useful properties. Thus, HEAs attracted worldwide attention as a new generation of alloys to resolve the challenges of modern industries with remarkable properties never seen before.

Much of the interest in HEAs is predicated on the belief that the maximized chemical complexity (Figure 1.1B) with many principal elements would produce profound intrinsic core properties, such as the high entropy effect, the lattice distortion effect, the sluggish diffusion effect, and the cocktail effect, which overcome the phase stability-property trade-off from Hume-Rothery rule [1, 2, 13, 14]. Thus, early design of HEAs focused on increasing the number of principal elements and the configurational entropy to maximize the benefits of chemical complexity. Recently, however, several researches have shown that the nature of elements is more important for the complexity-related properties than their mere numbers [4, 15-17]. A representative example of this argument is remarkably higher fracture toughness of equiatomic CrCoNi alloy with medium configurational entropy than equiatomic CrMnFeCoNi alloy (Figure 1.2 [4]). This introduces a new challenge, because not every combination of elements would be successful in achieving beneficial complexity-induced properties. Thus, a new definition of an alloy group, so-called complex concentrated alloy (CCA), was proposed; this refers the group of alloys that have at least two principal elements (≥5 at.%) covering an overall area of concentrated alloys from conventional binary systems to HEAs. The term “complex” is added to “concentrated alloy” in order to evoke and emphasize our interests on the vastness of composition space and the complexity-related properties of this alloy group.

**Table 1.1.** Some representative alloy systems and alloying elements.

| Alloy system (base element) | Name | Alloying elements ( >5 at.% ) |
|---|---|---|
| Cu | Copper | Cu |
| | Bronze | Cu, Sn |
| | Brass | Cu, Zn |
| Fe | Wrought Iron | Fe |
| | Cast Iron | Fe, C |
| | Hadfield | Fe, Mn |
| | Ferritic, Martensitic | Fe, Cr |
| | Austenitic, Duplex | Fe, Cr, Ni |
| | Triplex, Light weight | Fe, Mn, Al |
| | DP, TRIP, TWIP | Fe, Mn |
| Al | Duralumin | Al, (Cu) |
| | AlMgSi | Al, Mg, Si |
| | Aircraft Al | Al, Sc |
| | Al-Li | Al, Ni |
| Mg | Mg | Mg |
| | AZ series | Mg, Al, Zn |
| Ni | Ni-Cr | Ni, Cr |
| | Inconel, Hastelloy | Ni, (Co, Fe), Al, Cr |
| | Single crystal | Ni, Co, Cr, Al, (Mo, W, Ta, Re) |
| Ti | Ti | Ti |
| | Ti64 | Ti, Al, V |
| | Ti2448 | Ti, Nb, Sn, (Zr) |
| | Shape memory | Ti, Ni, (Cu) |
| Refractory | Zircaloy | Zr |
| | W-Re | W, Re |
| | Masc | Nb, Ti, Si, Cr, Al, (Hf) |
| Amorphous (complex) | Vitreloy | Zr, Cu, Ni, Al, Ti |
| | Matglas | Fe, Ni, P, B |
| Complex concentrated alloy (complex) | Cantor | Cr, Mn, Fe, Co, Ni |
| | Seokov | W, Ta, Mo, Nb, V |
| | CrCoNi | Cr, Co, Ni |
| | DP TRIP | Fe, Mn, Co, Cr |
| | VCrMnFeCoNi | V, Cr, Mn, Fe, Co, Ni |

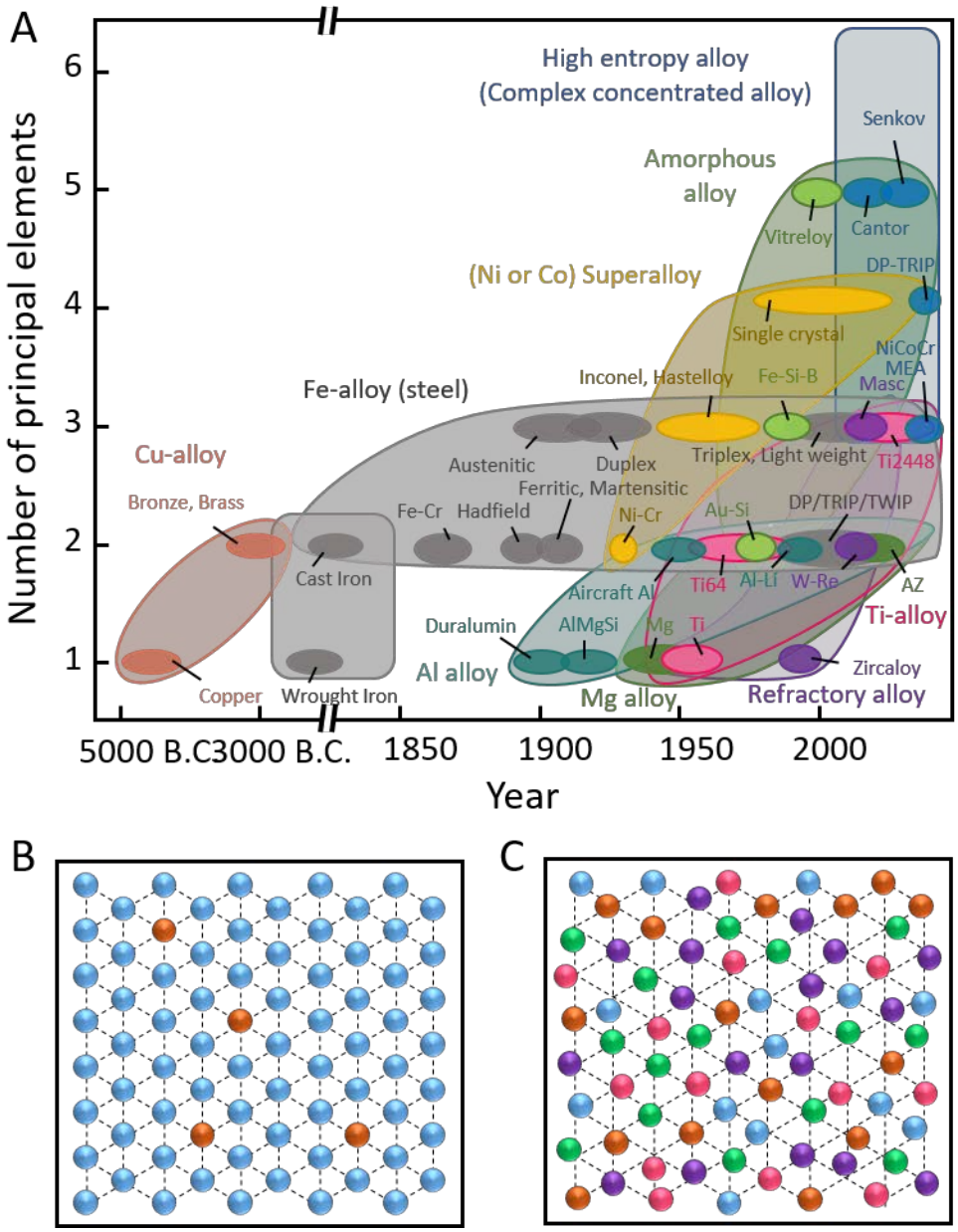


**Figure 1.1.** (A) A historical sketch showing an upward trend in the number of principal elements constituting general alloy systems over the past several centuries. It includes Cu alloy, Fe alloy, Al alloy, Mg alloy, Ti alloy, refractory alloy, superalloy (Ni or Co based), amorphous alloy and high entropy alloys. (B) Dilute alloy. (C) Complex concentrated alloy.

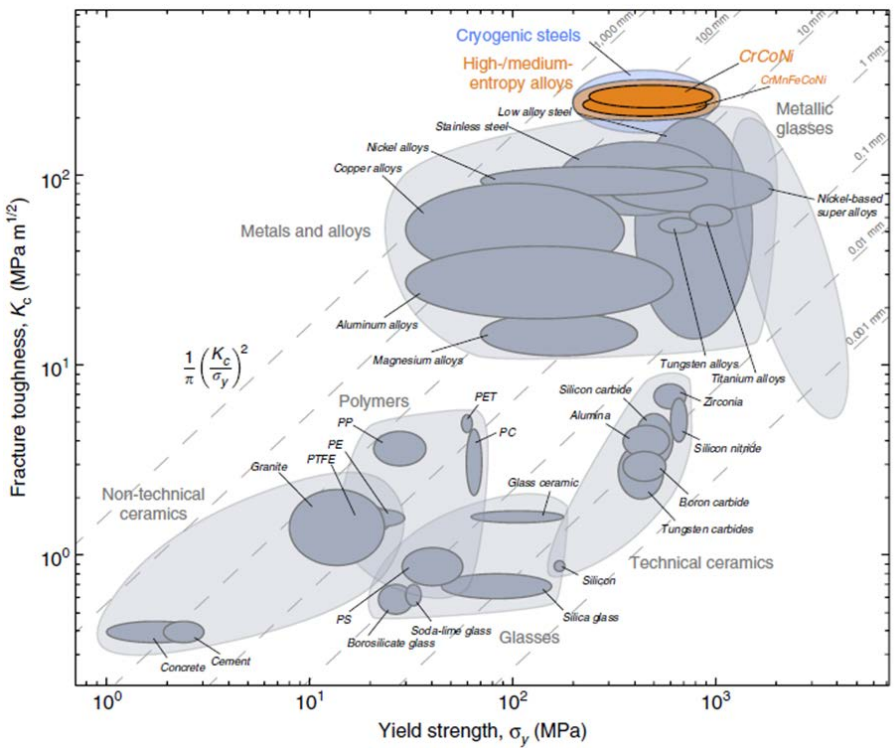


**Figure 1.2.** The investigated medium-entropy alloy CrCoNi compares favorably with materials classes like metals and alloys and metallic glasses. Its combination of strength and toughness (that is damage tolerance) is comparable to cryogenic steels, for example, certain austenitic stainless steels and high-Ni steels, and exceeds all high- and medium-entropy alloys reported to date. Reprinted from [4] (Creative Commons CC BY).

## 1.2. Motivation and scope

It is important to understand the fundamental aspects of the complexity-related properties in order to construct suitable alloy design strategies for CCAs. Several studies have been conducted to understand the properties using experiments or simulations (Table 1.2.; the detailed discussion is presented in Chapter 2). However, in spite the importance, the fundamental aspects of the complexity and its influence on the properties in CCAs are not well understood. Furthermore, the essential properties of constituent elements change depending on the local atomic configuration which is significantly complex and unpredictable in CCAs (Figure 1.1B). Hence, it is difficult to identify the exact role of the individual elements and predict the properties of CCAs without simulations, e.g., density functional theory (DFT). As a result, the advantage of so many degrees of freedom for alloy design of CCAs is diminished by a lack of quantitative mixing rules, rendering alloy design an empirical try-and-error undertaking. Therefore, in order to make a useful guide to design new CCAs, a parameter is required to describe the atomic-level complexity of CCAs in a physically meaningful way so that they can be directly related to properties.

Here, we applied the concept of atomic-level pressure in order to describe the local atomic structure and the atomic-level complexity of CCAs. We were inspired by elegant explanations for diverse phenomena in metallic glasses and liquids using atomic-level pressure, which are even more complex than CCAs with topological disorder, including topological instability, glass transition, mechanical failure, and structural relaxation [18]. Furthermore, the concept of atomic-level pressure has been used to describe the distribution of stress fields of solutes and the resultant

solid-solution strengthening of dilute alloys (See Chapter 3). Thus, we expected that atomic-level pressure can be a signature of atomic-level complexity, which enables the tailor-made alloy design approach of CCAs by nicely describing and explaining the structure-property relationships in CCAs.

In this thesis, the following issues of CCAs are addressed using the concept of atomic-level pressure:

- Origin of the atomic-level pressure in CCAs
- Categorize the "atomic-level complexity" in CCAs: "Chemical complexity" and "Complexity of atomic-level pressure"
- Relationship between two different level of complexities in CCAs: elemental difference and configurational difference
- Prediction of solid-solution strengthening
- Role of chemical complexity for the vastness of alloy design
- Correlation between atomic-level pressure and the lattice distortion
- Other properties of CCAs related to atomic-level pressure

3d CCAs, which consist of late 3d transition metal elements (V, Cr, Mn, Fe, Co, and Ni) with face-centered cubic (FCC) phase, are chosen as a model system, as the system is known to have outstanding mechanical properties, and some commercial alloys, e.g., austenitic steels and gamma matrix of superalloys, belong to the system, making high expectation of commercialization. Through this research, strategies for the tailor-made design of 3d CCAs are established focusing on the relationship between the atomic-level complexity of local atomic structure and properties. We used the strategies for designing new 3d CCAs with remarkably high mechanical properties exceeding previously reported 3d CCAs.

**Table 1.2.** Previous researches for the complexity induced properties in CCAs.

| | Tool | Main consideration | Reference |
|---|---|---|---|
| Phase stability | Statistics<br>Thermodynamics | Heat of mixing<br>Atomic size difference | [19-21] |
| | DFT | Formation enthalpy of ICs | [22] |
| Solid solution strengthening | DFT | Lattice distortion | [16, 23] |
| | Experiment + Theory | Misfit volume | [17, 24-26] |
| Diffusivity | Quasi-static model | Mean difference<br>in interaction energy | [27, 28] |
| Thermal conductivity | DFT | Blurred electronic band | [8] |

## 1.3. Outlines for each chapter

The outlines for each chapter are:

Chapter 2: Core effects from the atomic-level complexity of CCAs. Basic concepts of the core effects of CCAs are briefly reviewed to give a backdrop against which atomic-level complexity hypotheses can be discussed and evaluated.

Chapter 3: Fundamentals of atomic-level pressure. A brief survey on the subject of atomic-level pressure, focusing on the theoretical aspects and the application of atomic-level pressure to solid-solution strengthening theory.

Chapter 4: Experimental procedures. Brief introductions to all the experimental methods used in this thesis including sample preparation, microstructural characterization, mechanical analysis, and density functional theory calculation.

Chapter 5: Failure of structural analysis on the solid-solution strengthening of 3d CCAs. Measurements of the local structure of 3d CCAs by XRD and EXAFS for solid-solution strengthening are presented. The lattice distortions studies in the CrMnFeCoNi CCA by experiment and theory are also presented. Two different degrees of complexity, elemental deviation and configurational deviation, are also defined.

Chapter 6: Solid-solution strengthening of 3d CCAs – Atomic-level pressure. The correlation between the deviation of atomic-level pressure and solid-solution strengthening is provided with the quantitative design of new 3d CCAs with high solid-solution strengthening. In order to derive the parameter, descending the order of complexity problem is discussed.

Chapter 7: Design of new 3d CCAs to overcome strength-ductility trade-off.

Separating the control of strength (solid solution strengthening) and ductility (stacking fault energy) in 3d CCAs is discussed. Atomic-level complexity is categorized as chemical complexity and complexity of atomic-level pressure.

Chapter 8: Asymmetry of atomic-level pressure-induced element-specific properties in CCAs. The asymmetric behavior of properties induced by the atomic-level pressure is discussed including lattice distortion, diffusion, and preferential sites of interstitial solutes.

Chapter 9: Summary and outlook. This thesis is summarized and the possible further work is suggested.

# Chapter 2. Core effects from the atomic-level complexity of CCAs

The atomic-level complexity of CCAs leads to some important properties that are much less pronounced in conventional alloys: the high entropy effect; the lattice distortion effect; the sluggish diffusion effect; and the ‘cocktail’ effect [29-33]. Initially, these four core effects have been used to describe the multi-principal element character of HEAs, which are now being extended to the CCAs. The high entropy effect, which tends to stabilize the high-entropy phases, vastly increase the compositional space for new alloy development. The lattice distortion effect results in low electrical, thermal conductivity, and solid-solution strengthening for engineering applications. In addition, the sluggish diffusion effect is related to the creep resistance and irradiation resistance. Furthermore, the cocktail effect is not a hypothesis but a phrase describing synergistic mixture where the exceptional properties come from unexpected synergies.

These 4 core effects made a great contribution to the attention of CCAs. In this chapter, fundamental concepts of the three hypothesis, the high entropy effect, the lattice distortion effect, the sluggish diffusion effect, are briefly reviewed. We focused on critical concepts and important findings of each effect. Some arguments on the effects will be introduced together.

## 2.1. The high entropy effect

The high entropy effect proposes that phases with high configurational entropy tend to be stabilized over competing intermetallic compounds in equilibrium or non-equilibrium conditions. This was first proposed by Yeh [2] and became the signature concept of CCAs. This effect is very counterintuitive because the multi-component systems would contain many element pairs with high mixing enthalpy that may form intermetallic compounds. Thus, the high entropy effect has been searched by many researchers to investigate the phase stability of high entropy solid solutions [34-40].

The high-entropy effect is mainly used to explain two different stabilization mechanisms of high entropy phases, which are the contribution of configurational entropy for the Gibbs free energy at thermodynamic equilibrium conditions, and stabilization of high entropy phase during non-equilibrium quenching conditions (the maximum entropy production principle).

The high-entropy effect in the equilibrium condition states that the solid solution phases with high configurational entropy have lower Gibbs free energies than intermetallic compounds stabilizing their formation, particularly at higher temperatures. The Gibbs energy $G$ of a phase is

$$G = H - TS, \qquad \text{Eq. 2-1}$$

where $H$ is the fusion enthalpy, $T$ is the temperature, and $S$ is the mixing entropy. In an ideal solid solution or regular solid solution, the configurational entropy of mixing $S_{conf}$ has the form as

$$S_{conf} = -R \sum_i x_i ln x_i, \qquad \text{Eq. 2-2}$$

where $R$ is the gas constant and $x_i$ is the atom fraction of element $i$. From Eq. 2-2, disordered solid solutions with equi-molar-ratios has the configurational entropy and become more stable when assuming an ideal or regular solid solution.

However, in most cases, solid solutions are sub-regular, which have a large heat of mixing and non-random configuration of constituent elements (Figure 2.1B). Furthermore, the mixing enthalpy of intermetallic compounds is more pronounced than the mixing entropy of solid solution phases. Senkov et al. [20] screened the thermodynamic stability of 130000 alloys using the CALPHAD to calculate the phase diagram of each alloy and found that solid solution alloys become less common as the number of the components increases as depicted in Figure 2.2, which shows the distributions of CCAs by categories. Moreover, solid solution (SS) alloys consist only of one or more solid solution phases while intermetallic compound (IM) alloys consist of one or more intermetallic phases. Consequently, SS+IM alloys contain both solid solution and intermetallic phases. For SS alloys, the fraction of the solid solution is larger at melting temperature ($T_m$) than 600℃. IM alloys have opposite tendency to the SS alloys. As the number of components increases, the fraction of both SS and IM alloys decreases while the fraction of SS+IM alloys increases. This tendency was explained by the difference of increasing rates between the configurational entropy (ln(N)) and the number of binary interaction pairs (2/N(N-1)). The probability of at least one element pair with a mixing enthalpy larger than the configurational entropy increases with increasing number of components. This shows that the high entropy effect may not contribute to the real phase stability of solid solution alloys from a thermodynamic point of view.

For the non-equilibrium thermodynamic condition, the high entropy effect is

explained according to the maximum entropy production principle (MEPP) [41], which states that high entropy tends to stabilize the high entropy phases rather than intermetallic phases. Thus, it can be applied for phase stability at the as-cast state and welding performance of CCAs. This concept is similar to a widely accepted concept in metallic glass society called the “confusion principle.” [42] The principle states that the higher glass forming ability of multi-component system, rather than simple binary systems. Unlike the confusion principle, a small number of HEA or CCAs papers (less than 10 papers) cite the original article of MEPP. However, this concept would be one of the major ones showing the entropy induced phase stabilization of high entropy phases.

There are several other factors that should be considered for the entropy of CCAs. Vibrational, electronic, and magnetic entropies were examined in CrMnFeCoNi CCA using ab-initio calculation [14, 43]. Surprisingly, the contribution of vibrational entropy is much larger than configurational entropy value at the finite temperature (Figure 2.3). Even electronic and magnetic entropies can contribute up to 50% of the configurational entropy, which means that the actual situation of the entropy is much more complex than the simple consideration of configurational entropy.

This section briefly reviewed the high entropy effect. In the equilibrium condition, the high entropy effect competes with the high mixing enthalpy where the mixing enthalpy effect dominates the phase stability. In the non-equilibrium condition, MEPP may contribute to the phase stability, e.g., welding condition. However, the entropy may not be dominantly affected by the configurational entropy. Therefore, more systematic research for the high entropy effect of CCAs is required.

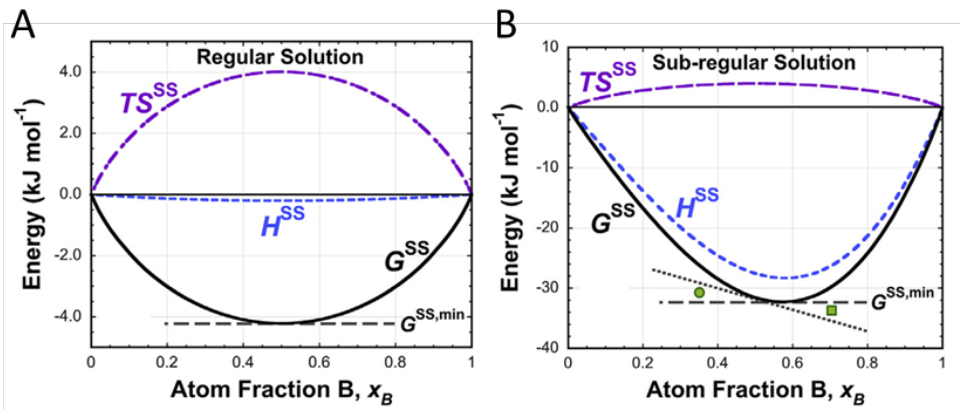


**Figure 2.1.** The integral molar entropy, enthalpy and Gibbs energy at 700K for negative deviations from ideal behavior in (A) a regular solution Co-Ni, and (B) a sub-regular solution Ce-Ni. Reprinted from [14] (CC BY NC ND).

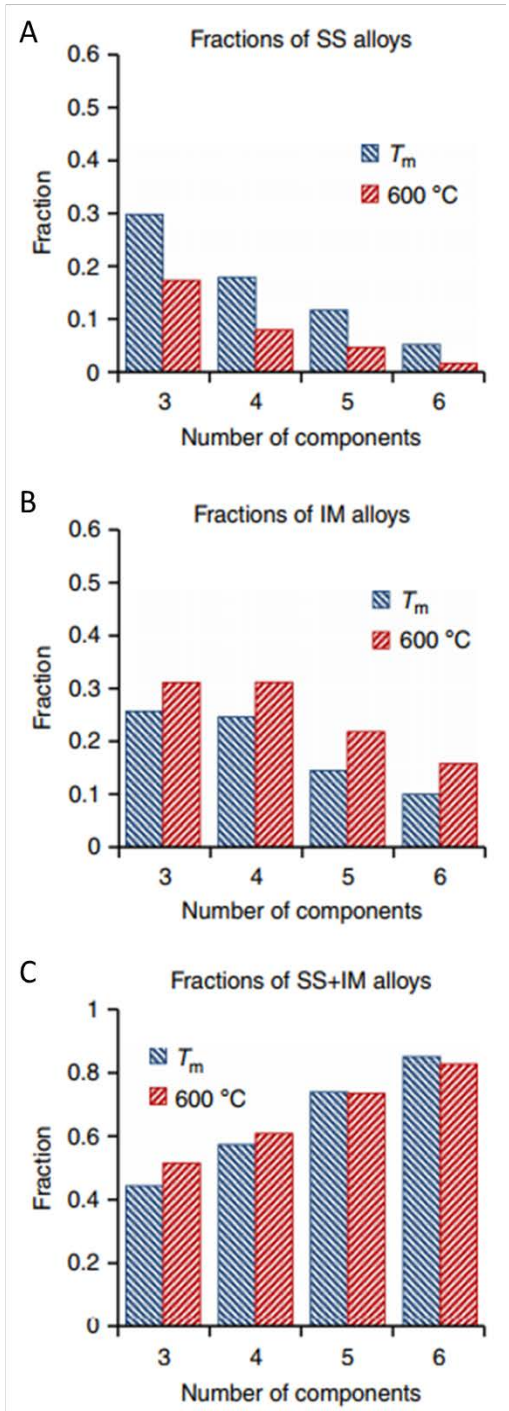


**Figure 2.2.** Fraction of alloys having (A) SS, (B) IM, and (C) SS+IM alloys at 600℃ and melting temperature $T_m$. Reprinted from [20] (CC BY).

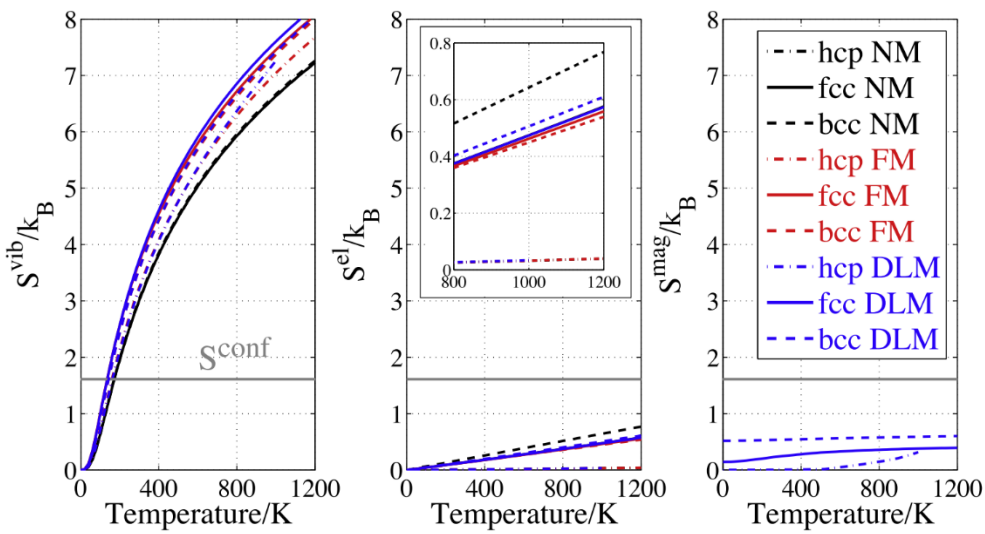


**Figure 2.3**. Ab-initio calculated temperature dependence of the vibrational entropy $S^{vib}$, electronic entropy $S^{el}$, and the magnetic entropy $S^{mag}$ in the CrMnFeCoNi CCA. Gray horizontal lines indicate the configurational entropy $S^{conf}$. Reprinted from [43] with permission through "Copyright Clearance Center".

## 2.2. The lattice distortion effect

In dilute alloys, a solute atom is surrounded by dissimilar solvent atoms. Thus, the local atomic environment is symmetric and the solute atom is fixed in its original lattice position. In this case, the solvent atoms are repulsed or attracted to the solute atom, leading to lattice distortion. In CCAs, all constituent elements are solute and solvent. As a result, the local atomic environment is asymmetric and all atoms are displaced from their original lattice sites. This can lead to more severe lattice distortion than in conventional alloys.

The concept of severe lattice distortion of a CCA was first proposed by Yeh et al. [44] for HEAs and widely become one of the four proposed 'core effects' [45, 46]. In their paper, Yeh et al. studied the lattice distortion of a CuNiAlCoCrFeSi alloy series with different numbers of incorporated elements through quantitative analyses of XRD intensity levels. By increasing the number of elements, the variation of the XRD peak intensities of these alloys decreased greatly beyond the thermal effects. The authors insisted that the decreased XRD intensity levels originate from the intrinsic lattice distortion caused by the addition of multi principle elements with different atomic sizes, as shown in Figure 2.4. The roughening of atomic planes from the differently sized atoms contributes to the XRD scattering effect beside thermal effect.

Guo et al. [47] studied the local atomic structure of equiatomic ZrNbHf with single body-centered cubic (BCC) phase using high-energy synchrotron X-ray and neutron scattering by means of a pair distribution function (PDF) analysis. Figure 2.5 shows the first two peaks of the radial distribution function (RDF) of ZrNbHf. The width of the second shell is much wider than the first shell. This type of

broadening implies that the lattice becomes distorted away from the average body-centered cubic (BCC) structure. The authors insisted that the distortion of this alloy stems from the different metallic radii of constituent elements (Zr:1.60, Hf:1.59, and Nb:1.46 Å).

The above works proposed that the atomic size difference from the mixture of multi-principle elements in a CCA is the origin of the lattice distortion. Based on this, several geometrical atomic packing models [48, 49] have been established to explain the lattice distortion caused by atomic size differences. Furthermore, the atomic size difference factor has been proposed to predict the solid solution strengthening effect and additional entropy terms of a CCA [14, 50]. However, there are several challenges arising from the complex atomic configuration of CCAs. First, the effective atomic radius differs from the original metallic radius [16, 23]. Second, the role of the number of elements with regard to atomic size difference is unclear.

Atomic stress arises from the difference between the central atom and the surrounding atoms. This stress changes the atomic sizes and positions and is, thus the origin of lattice the distortion [51]. Effective atomic radii of the constituent elements in CrMnFeCoNi CCA were studied by Extended X-ray Absorption Fine Structure (EXAFS) and DFT calculations [23]. The atomic sizes differ with the metallic radii and are affected by charge transfer and magnetism. Furthermore, the local atomic sizes differ significantly from their average sizes of each element due to the complexity of local atomic configurations. Thus, using the metallic radii as a precursor of the effective radii should be regarded as a simple approximation and may be inaccurate when used to describe the actual situation.

Owen et al. [15] measured the lattice strain of CrMnFeCoNi CCA in comparison with five compositionally simpler materials within an identical system

using neutron radiation. The local lattice strain in this system was assessed through a detailed evaluation of the PDF peak widths corresponding to the first six coordination shells. As shown in Figure 2.5A, the CrMnFeCoNi CCA exhibited the highest full-width half maximum (FWHM), which indicates the highest level of local lattice strain. However, this value was not markedly larger than those of Ni-33Cr or Ni-37.5Co-25Cr. Thus, the level of strain was not disproportionately greater than in the other alloys. Furthermore, due to its lowest melting point, the CrMnFeCoNi CCA is expected to have the highest thermal vibration, which contributes to the peak broadening. Thus, the authors concluded that there is no indication suggesting severe lattice distortion in the CrMnFeCoNi CCA compared to that in other binary or ternary alloy systems. The irrelevance with regard to the number of constituent elements coupled with the lattice distortion of CCAs was more clearly shown by Okamoto et al. [16] through their comparison of the DFT-calculated mean-squared atomic displacements (MSAD) of sub-alloys of the CrMnFeCoNi CCA (Figure 2.5B)

Most studies of the lattice distortion focus on 3d CCAs. Recently, the lattice distortions of refractory metal-based CCAs with single BCC phase (refractory CCAs) were calculated through ab-initio calculations [52]. These results revealed that refractory CCAs have much greater lattice distortion than 3d CCAs (Figure 2.6). Furthermore, the atomic size mismatch evaluated from the empirical atomic radii was not accurate enough to predict the lattice distortion effects, as in 3d CCAs. This indicates that the challenges discussed in this section are common issues of all CCAs regardless of the element groups.

In this section, several core works pertaining to the lattice distortion effect of CCAs are briefly reviewed. Lattice distortion is related to the elastic strain energy of the CCAs and the cause of solid-solution strengthening, sluggish diffusion,

irradiation resistance, and electrical and thermal conductivity, among other outcomes. However systematic attempts to quantify and rationalize the lattice distortion have yet to be offered. Further approaches to measure and model lattice distortions are therefore required.

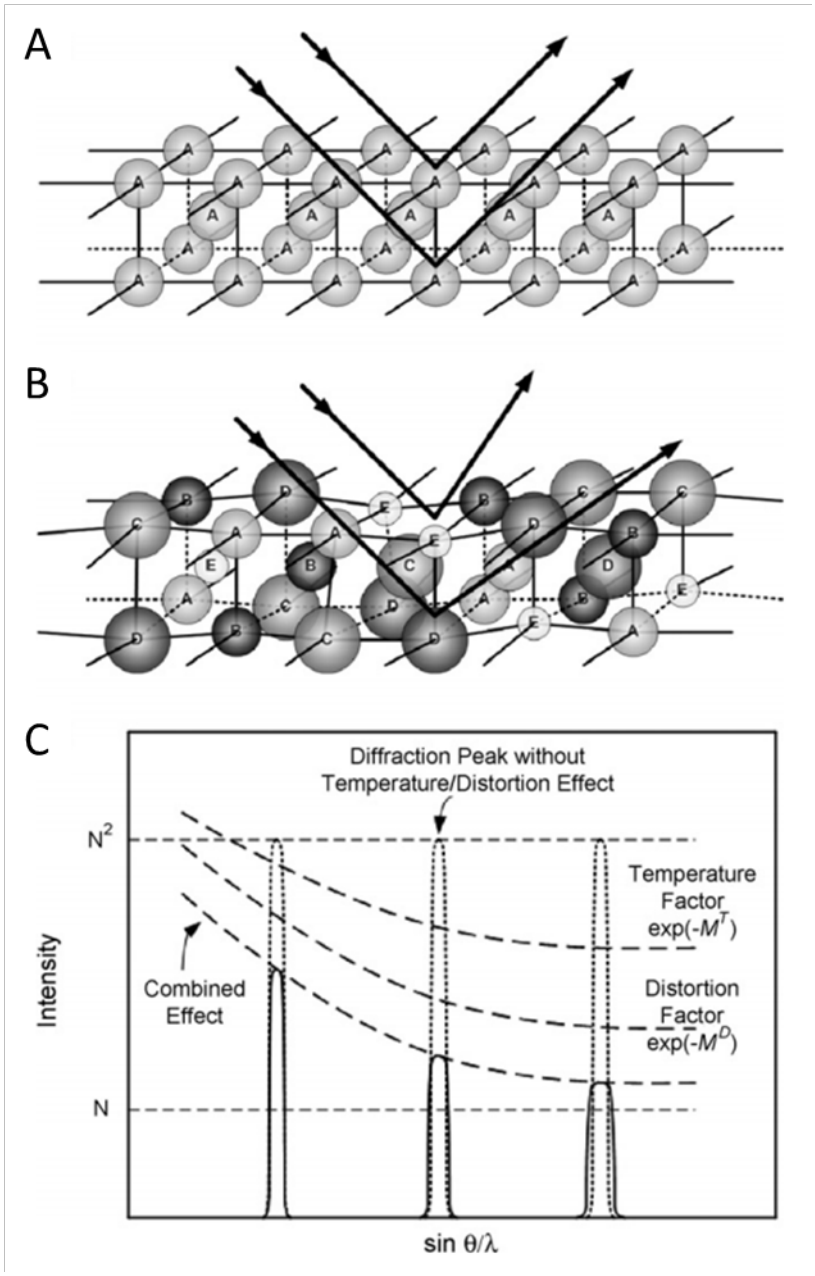


**Figure 2.4.** Schematic illustration of lattice distortion of CCA and the effect to the Bragg diffraction: (A) Pure element; (B) Distorted lattice of CCA; (c) Decrease of X-ray intensity due to the thermal and statistical lattice distortion effect. Reprinted from [44] with permission through "Copyright Clearance Center".

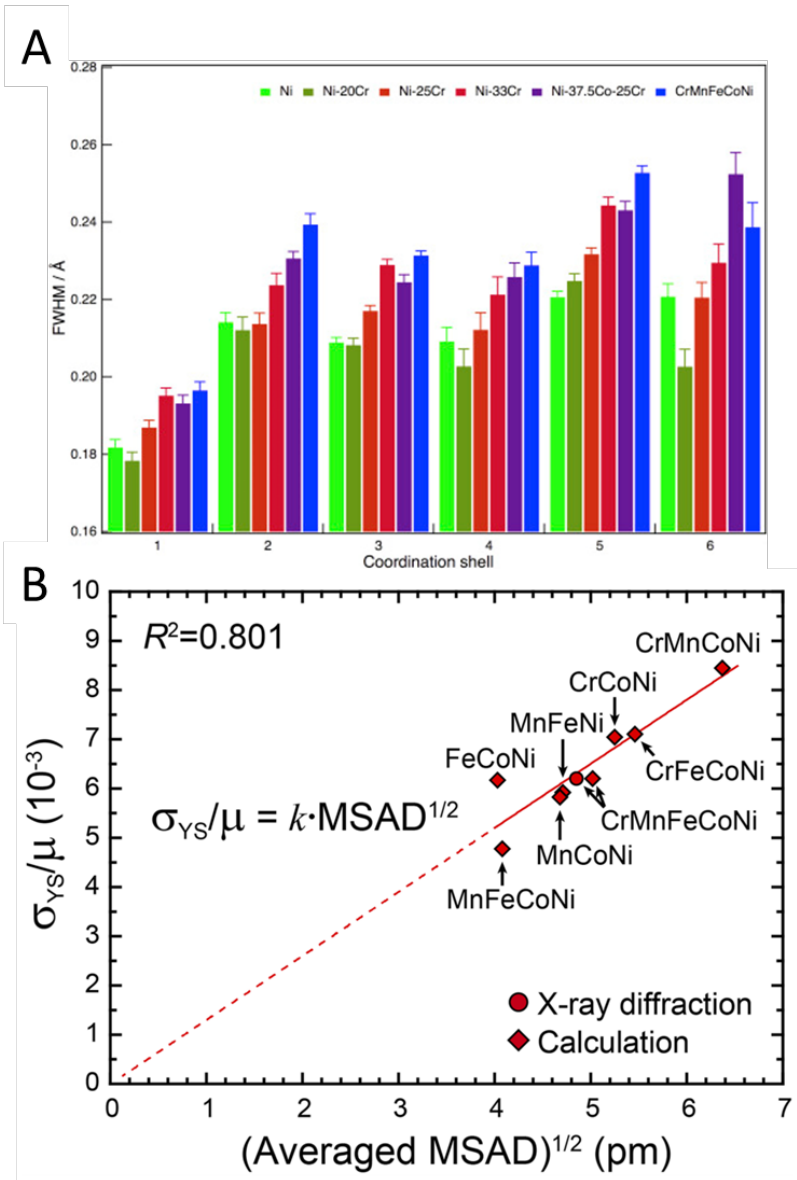


**Figure 2.5.** Comparison of lattice distortion between sub alloys of CrMnFeCoNi CCA. (A) Experimentally measured lattice distortion through full width half maximum values of pair distribution peaks. (B) The relationship between normalized yield strength and DFT-calculated mean squared atomic displacement of each alloy. Reprinted from [15]-(A), [16]-(B) (CC BY).

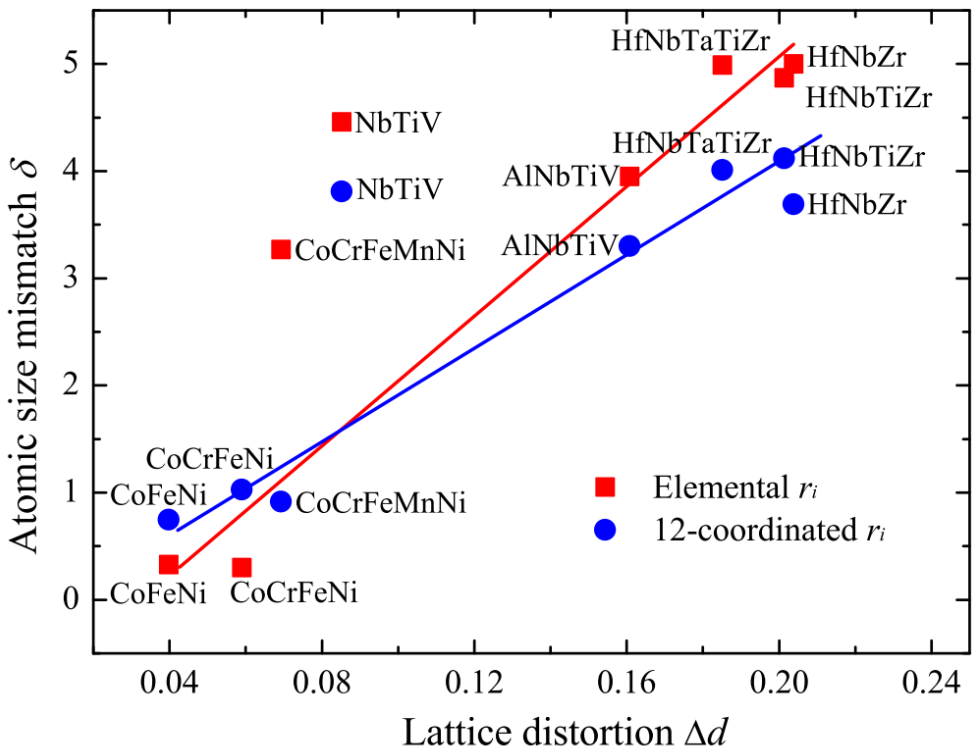


**Figure 2.6.** Comparison between atomic size mismatch δ from empirical atomic radii versus the ab-initio predicted lattice distortion Δd for bcc HfNbZr, HfNbTiZr, HfNbTaTiZr, NbTiV, and AlNbTiV and for fcc CoFeNi, CoCrFeNi, and CoCrFeMnNi. Reprinted from [52] with permission through "Scientific Publishing and Remittance Integration Services".

## 2.3. The sluggish diffusion effect

The sluggish diffusion effect was proposed as one of the four core effects of HEA (and of CCAs as well). This effect is related to the practical features of high-temperature applications, such as grain growth in relation to creep properties [53], the nucleation and growth of unexpected phases [2], irradiation resistance [54] and oxidation resistance. Thus, a better understanding of the sluggish diffusion effects of CCAs is essential. However, in spite its importance, actual measurements and fundamental discussions of the diffusion kinetics have been reported for only a few CCAs.

Owing to the compositional complexity, measuring the diffusion kinetics of CCAs is difficult. Early considerations of this hypothesis were based on secondary observations. Yeh et al. [2] were the first to propose the sluggish diffusion effect for the CuCoNiCrAlFe equimolar alloy. In the as-cast state, this alloy contains nanosized precipitates due to spinodal decomposition (Figure 2.7). The authors focused on the small size of the precipitates and suggested that the long-range diffusion for phase separation was sluggish. Similarly, the sluggish diffusion was interpreted to be responsible for the formation of the nanostructure of as-cast $Al_XCoCrCuFeNi$ [55], the retention of nanocrystals in AlCrMoSiTi, and the absence of the formation of low-temperature phases in $Al_{0.5}CoCrCuFeNi$ [56] during furnace cooling. Conceptually, the sluggish diffusion kinetics for the formation of a new phase is related to the cooperative diffusion of elements to achieve equilibrium partitioning among different phases [56]. The diffusion rate of each element in a CCA differs. However, phase transformation or grain growth requires the redistribution of all elements to reach the desired composition. Thus, by means of

slowly diffusing elements, such phenomena can be kinetically destabilized and their occurrence prevented.

Conceptual and quantitative studies of the sluggish diffusion kinetics of a CCA were proposed by Tsai et al [27]. Using the quasi-chemical seven-bond interaction energy (SBIE) model (Figure 2.8), Tsai et al. suggested that a multi-component CCA has greater lattice potential energy (LPE) fluctuations than a conventional alloy during atomic migration. During the migration of the central atom, a difference in the interaction energies of neighboring atomic configurations before and after migration determines the size of the LPE fluctuation (Figure 2.8A). CCAs have large LPE fluctuations for two the main reasons of the large mixing enthalpy and the large number of seven-bond energy states. First, CCAs have a high solubility of strong bonds originating from the dilute nature of each element in the multi-element mixture. Thus, high heat from mixing can be achieved in CCAs. Second, CCAs with a large number of elements have divergence in their LPEs. In such a case, the distribution of LPE is more continuous and the resultant degree of LPE fluctuation becomes larger. In consequence, CCAs have large LPE fluctuations and the LPE fluctuation leads to a significantly longer occupation time of a specific element at a low-energy site, thus resulting in the suppression of atomic or vacancy migration (Figure 2.8B).

Not only the cohesive energy of bonding in CCAs, which is represented by the mixing enthalpy, but also the elastic strain energy and packing density can affect the sluggish diffusion kinetics of CCAs. With experimental results and by means of mechanistic analyze, Chang et al. [57], proposed that suppressed interdiffusion kinetics in CCAs come from the elastic strain energy and high packing density, and, thermodynamically, strong cohesion energy. The model predicted the activation

energies of the interdiffusion of Cu atoms at a series of diffusion barriers with multi-principle elements from Ti to TiTaCrZrAlRu alloys, and it could successfully explain the suppressed interdiffusion kinetics of high-entropy systems.

Direct measurements of diffusion kinetics of CCAs are rare [27, 58-61], as the compositional complexity makes diffusion measurements difficult. The first measurement of diffusion kinetics was performed for 3d CCAs using thermocouples [27, 58]. The activation energy of diffusion, normalized by the melting temperature, of CrMnFeCoNi CCA is slightly higher than those of other ternary alloys (Fe-Cr-Ni) and pure elements. Similar to this work, several measurements or calculations of diffusion kinetics of 3d CCAs have been reported. In most cases, CrMnFeCoNi CCA has the lowest diffusivity as compared to other CCAs. However, the differences are small and less than one order of magnitude. This implies that the diffusion kinetics of 3d CCAs are not essentially sluggish relative to the diffusion in pure metals and conventional alloys.

In this section, the fundamental concepts and a number of works on the sluggish diffusion effect in CCAs are briefly introduced. Although it is frequently used as a representative characteristic of CCAs, systematic studies of this effect are still lacking. Direct measurements of diffusion kinetics have been performed only for 3d CCAs and some researchers argue that the sluggish diffusion effect of a CCA may be false. However, the concept of sluggish diffusion in CCAs was derived from diffusion theories, which means that the concept is accurate despite the differences in degrees within different CCAs. The elements existing in 3d CCAs are very similar to each other, and the diffusion kinetics appears to be less sensitive to the degree of chemical complexity as compared to other effects such as solid-solution strengthening. Therefore, systematic studies of various types of CCAs are needed.

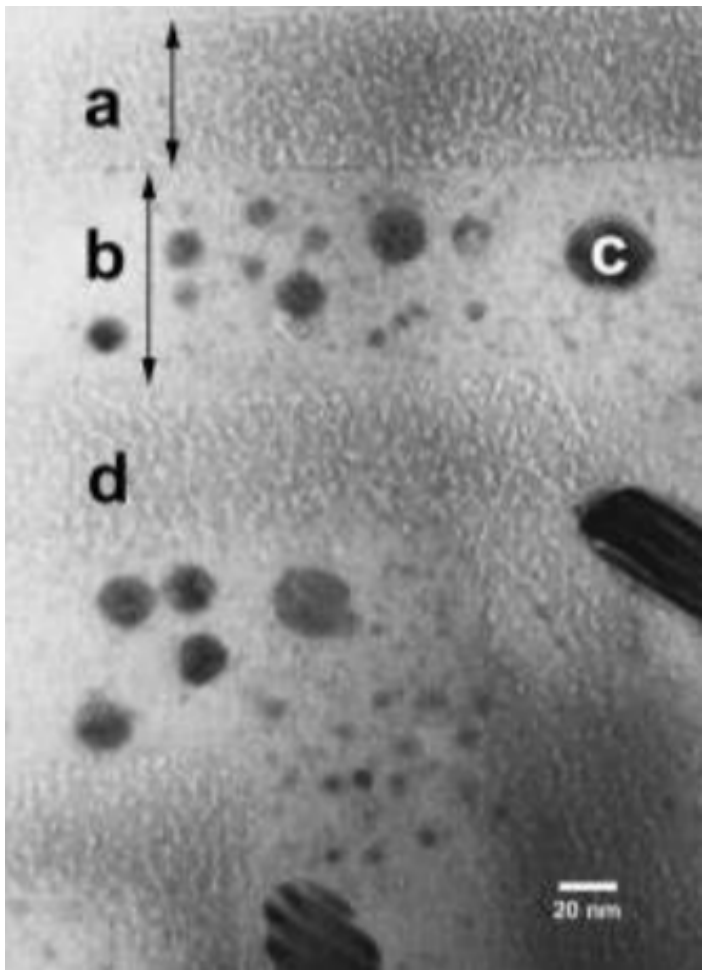


**Figure 2.7.** TEM bright-field image of as-cast CuCoNiCrAlFe alloy. a: indicates inter-spinodal plate, disordered bcc phase (A2), b: spinodal plate, ordered bcc phase (B2), c: nanoprecipitation inspinodal plate, close to fcc phase, d, nanoprecipitation in inter-spinodal plate, disordered bcc phase (A2). Reprinted from [2] with permission through "Copyright Clearance Center".

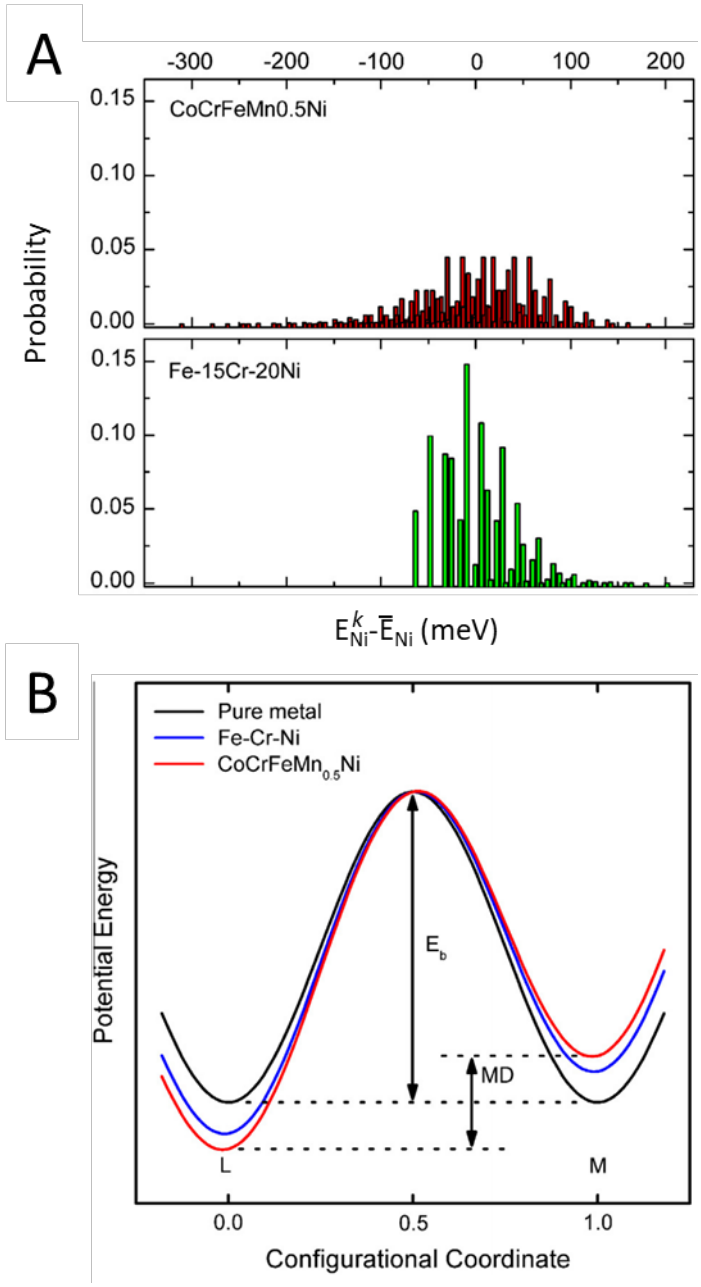


**Figure 2.8.** Quasistatic model showing the sluggish diffusion of CCAs. (A) Probability distributions of SBIE for Ni in $CrMn_{0.5}FeCoNi$ and Fe-Cr-Ni. (B) Schematic diagram of the difference of fluctuation of LPE within different alloys during the migration of a Ni atom. Reprinted from [27] with permission through "Copyright Clearance Center".

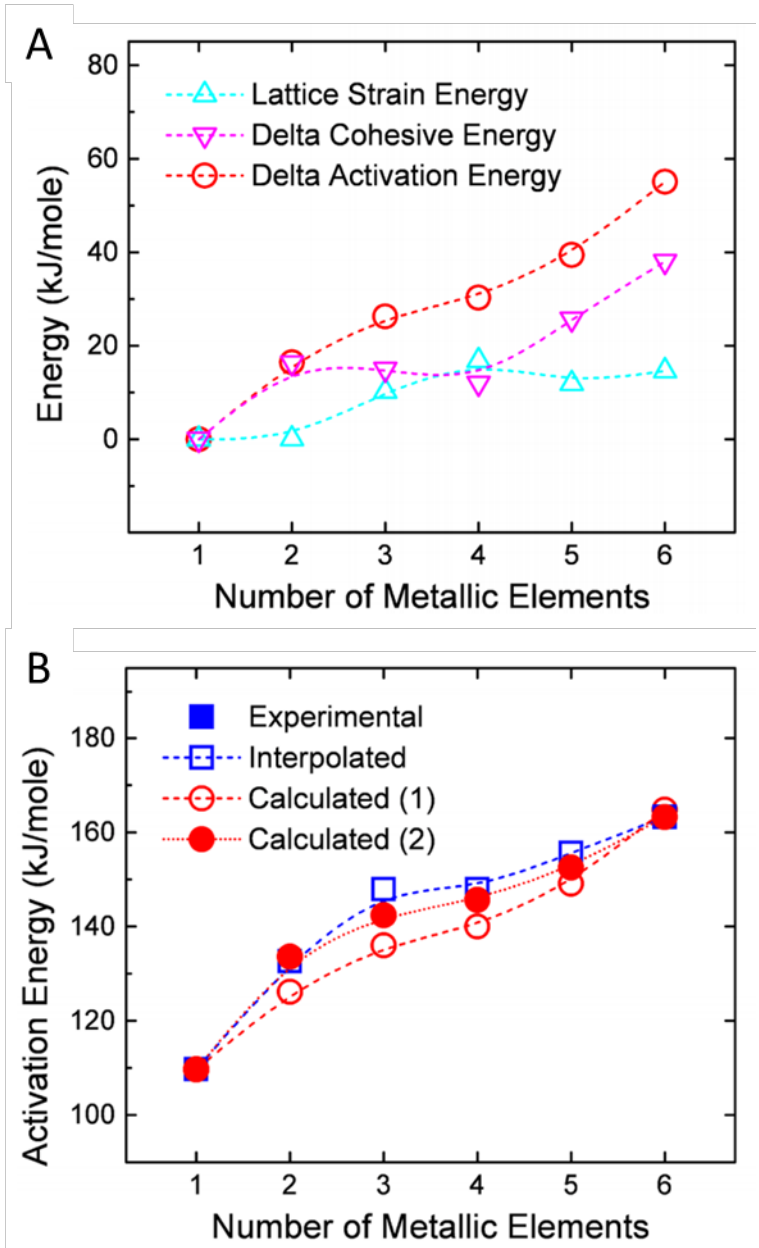


**Figure 2.9.** (A) Contribution of each source of activation energies of Cu diffusion in/through nA alloys from Ti to TiTaCrZrAlRu. (B) Comparison between experimentally measured and theoretically calculated activation energies. Reprinted from [57] (CC BY-NC-ND 3.0).

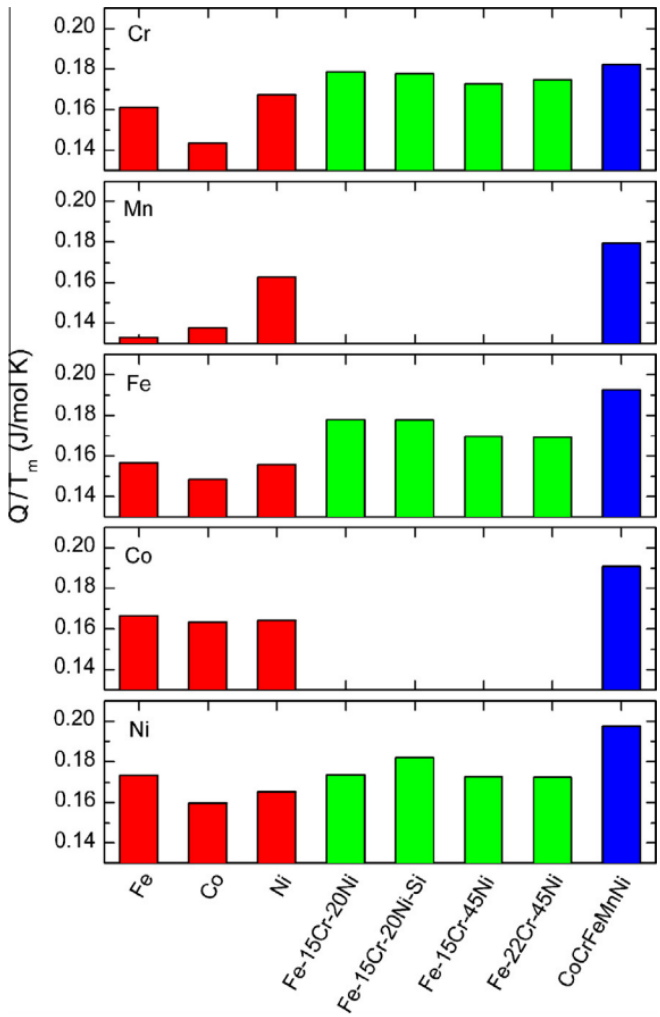


**Figure 2.10.** Activation energies of diffusion for each element in different CCAs including CrMnFeCoNi, Fe-Cr-Ni and pure elements. Reprinted from [27] with permission through "Copyright Clearance Center".

## 2.4. Summary

In this chapter, the core effects of CCAs —the high entropy effect, the lattice distortion effect, and the sluggish diffusion effect — are briefly reviewed. It has been expected that these core effects may provide information about the important advantages of CCAs. However, in spite the level of interest, early considerations of these hypotheses rely on secondary observations, and the fundamental aspects remain not well understood. As a result, the advantage of the numerous degrees of freedom is diminished by a lack of quantitative alloy design rules, rendering alloy design an empirical trial-and-error undertaking. Therefore, more studies are needed to establish the basic features of these effects and to provide practical guidelines for the tailor-made designs of CCAs to maximize the benefits of the effects.

In the following chapters, the fundamental aspects of the core effects are investigated, in particular the lattice distortion effect. The concept of atomic-level pressure, which is the origin of the core effects, is introduced to provide an explanation of the lattice distortion and solid-solution strengthening effects of CCAs. Through this research, the guidelines for tailor-made designs of CCAs are presented focusing on the atomic-level complexity and its influence on the properties.

# Chapter 3. Fundamentals of atomic-level pressure

Atomic-level pressure arises when the nature of a solute atom —size, elastic moduli, electronic state— is different from the surrounding environment. The atomic-level pressure increases the elastic energy of the system and is the most important origin of an alloy including diffusivity, strengthening, and thermal or electrical conductivity. Meanwhile, the concept of atomic-level pressure has been used to explain the diverse phenomena in metallic glasses and liquids, including topological instability, glass transition, mechanical failure, and structural relaxation [18]. Considering that amorphous alloys are even more complex than CCAs with the topological disorder, the atomic-level pressure is expected as a useful parameter to describe the local structure in a physically meaningful way to explain the complexity-induced properties of CCAs.

In dilute alloys, the atomic-level pressure of solute element is consistent to the solute position as a solute atom is always surrounded by solvents. On the other hand, the atomic pressure of solutes in CCAs is dependent on not only the center element itself but the interaction with the surrounding environment, resulting in configurational pressure difference. Thus, it is important to investigate the origin of atomic-level pressure and its influence on the properties. In this chapter, the concept of atomic-level pressure is introduced. The classical concept of atomic-level pressure based on continuum elasticity and newly developed energy based concept are reviewed.

## 3.1. Classical concept of atomic-level pressure

Classically, atomic-level pressure is expected to arise when the size or elastic moduli of a solute atom is different from the matrix. The atomic-level pressure increases the elastic energy of the system, resulting in complexity-induced phenomena such as solid-solution strengthening. The classical concept of atomic-level pressure was derived from elasticity theory. In this section, (1) classical concept of atomic-level pressure which was drawn by Eshelby inclusion problem, and (2) application of the concept to solid-solution strengthening theory are introduced.

### 3.1.1. Eshelby inclusion problem

In continuum linear elasticity theory, atomic-level pressure of a solute atom is dealt with Eshelby's inclusion problem [62]. Eshelby proposed the problem to investigate the elastic field of a heterogeneous inclusion in a matrix. The procedure is following:

> "
>
> Cut round the region which is to transform and remove it from the matrix.
>
> Allow the unconstrained transformation to take place.
>
> Apply surface tractions chosen so as to restore the region to its original form.
>
> Put it back in the hole in the matrix and rejoin the material across the cut.
>
> " [62]

Following the procedure, a solute atom is regarded as a spherical inclusion, whose initial volume is $V_{s,i}$, forced into a spherical hole of slightly different size,

$V_h$, in an infinite and continuum elastic media. Then, if $V_{s,i}$ is larger than $V_h$ (Figure 3.1.A), (1) the solute atom should be compressed to fit to the hole, and (2) expands during relaxation pushing neighboring atoms away. When $V_{s,i}$ is smaller than $V_h$ (Figure 3.1.B), (2) the solute atom should be expanded to fit to the hole, and (2) shrinks during relaxation attracting neighbor atoms. After the relaxation, the volume of the solute changes to $V_{s,f}$ and atomic-level pressure is

$$P = B\varepsilon_v, \qquad \text{Eq. 3-1}$$

where B is the bulk modulus of a solute atom and $\varepsilon_v$ $(= (V_{s,i} - V_{s,f})/V_{s,f})$ is the atomic volume strain. Considering the elastic constraint from the matrix $((1+\nu)/3(1-\nu))$, P in Eq. 3-1 can be also described using $V_{s,i}$ and $V_h$ as

$$P = (1+\nu)/3(1-\nu)\, B\varepsilon, \qquad \text{Eq. 3-2}$$

where $\nu$ is the Poisson's ratio and $\varepsilon = (V_{s,i} - V_h)/V_h$.

## 3.1.2. Solid-solution strengthening and atomic-level pressure

Atomic-level pressure of solute atoms interacts with stress field of dislocations raising or lowering the elastic strain energy of the system. In most cases, this interaction energy disturbs the movement of dislocations, which is so-called solid-solution strengthening [63]. Theory of solid-solution strengthening of dilute or concentrated alloys have been propounded by many researchers, e.g. Mott and Nabarro [64, 65], Cottrell [63], Fleischer [66, 67], Labusch [68], Friedel [69], Haasen [70], and recently Curtin [71-73]. In most cases, the solute/dislocation interaction energy $E_I$ is described by

$$E_I = P_{dis}\Delta V_{sol}, \quad \text{Eq. 3-3}$$

where $P_{dis}$ is the pressure field of the dislocation at the solute site and $\Delta V_{sol}$ is the misfit volume of the solute atom at this site. For example, Cottrell-Bilby formula, a famous formula of $E_I$, has the form as

$$E_I = \frac{4}{3} G\epsilon r_a^3 \lambda \frac{1+\nu}{1-\nu} \frac{sin\,\alpha}{r}. \quad \text{Eq. 3-4}$$

where $G$ is the shear modulus, $\epsilon$ is the size misfit factor of solute, $r_a$ is the average atomic radius of solvent, $\lambda$ is the slip distance in the dislocation, $r$ and $\alpha$ are coordinates of a solute atom relative to the dislocation. Eq. 3-4 implies that the atomic-level pressure can be approximated by the size misfit factor of the solute element which can be obtained by compositional dependence of lattice parameter.

From Maxwell-Betti reciprocal principle, the $E_I$ can be also calculated by

$$E_I = P_{sol}\Delta V_{dis}, \quad \text{Eq. 3-5}$$

where $P_{sol}$ is the pressure field of the solute atom at the dislocation and $\Delta V_{dis}$ is the misfit volume of the dislocation at the solute site. Formally, $E_I$ values obtained by Eq. 3-3 and Eq. 3-5 are equal to each other. Usually, Eq. 3-3 has been used to model the elastic interaction energy from experimental data. However, Eq. 3-5 can directly show the effect of atomic-level pressure on elastic interaction energy of solute elements.

### 3.1.3. Solid-solution strengthening in CCAs

A parameter-free and predictive model for the solid-solution strength of CCAs

with single FCC phase has been developed by C.Varvenne [25], assuming the effective matrix as

$$\tau_{y0} = 0.051\alpha^{-\frac{1}{3}}\mu\left(\frac{1+\nu}{1-\nu}\right)^{\frac{4}{3}} f_1(w_c) \times \left[\frac{\sum_n c_n\left(\Delta\bar{V}_n^2+\sigma_{\Delta V_n}^2\right)}{b^6}\right]^{\frac{2}{3}}, \qquad \text{Eq. 3-6}$$

where $\alpha$ is the line tension parameter, $\mu$ is the shear modulus, $\nu$ is the Poisson's ratio, $f_1(w_c)$ is the parameter for dislocation core structure, $c_n$ is the composition of nth element, $\Delta\bar{V}$ is the average misfit volume of the solute, $\sigma_{\Delta V_n}^2$ is the variance of misfit volume of solute atom according to the local configurations (i.e. local environments), $b$ is the Burgers vector. $\left[\frac{\sum_n c_n\left(\Delta\bar{V}_n^2+\sigma_{\Delta V_n}^2\right)}{b^6}\right]^{\frac{2}{3}}$ shares the same meaning of $\Delta V_{sol}$ in Eq. 3-3, which means the local volumetric strain causes the atomic-level pressure. The spatial distribution of concentrated solutes is considered by $2/3$, which follows the Labusch's approach.

There is another contribution of element properties, which is so-called modulus effect [74]. Solute atoms alter both the overall bulk modulus and the overall shear modulus. This result in the modification of the line tension by a global effect. Furthermore, solute atoms change the line energy due to the change in the elastic strain energy [66, 67]. In Varvenne's model, Eq. 3-6 includes the modulus effects automatically by atomistical calculation of core interactions [71].

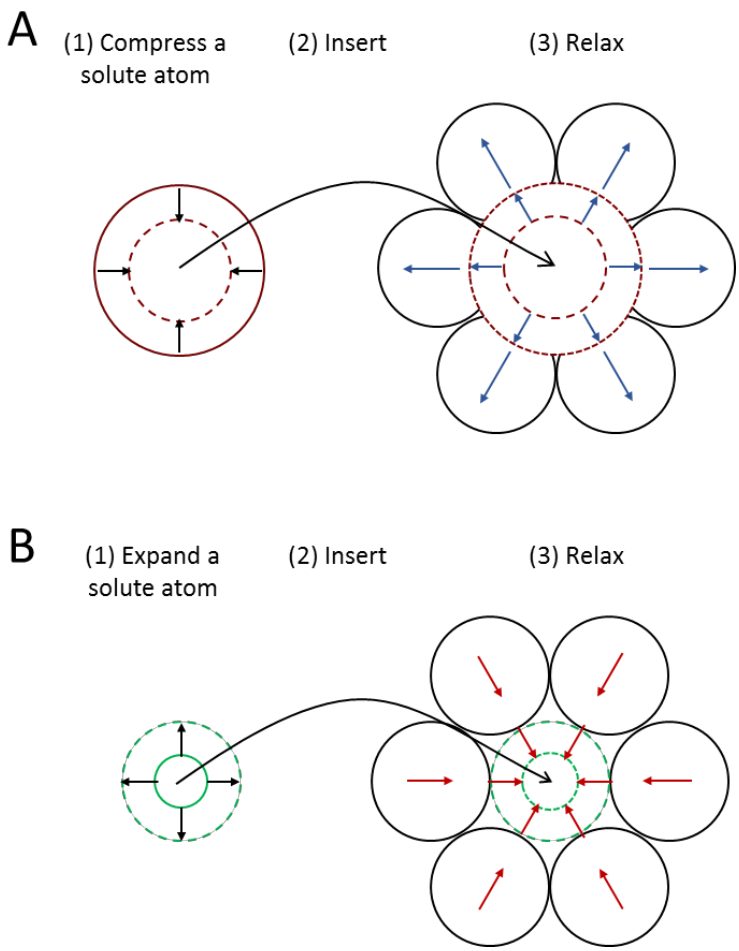


**Figure 3.1.** Schematic illustration showing the classical view of atomic-level pressure by Eshelby inclusion model. (A) The size of solute atom is larger than the solvent atoms. (B) The size of solute atom is smaller than the solvent atoms.

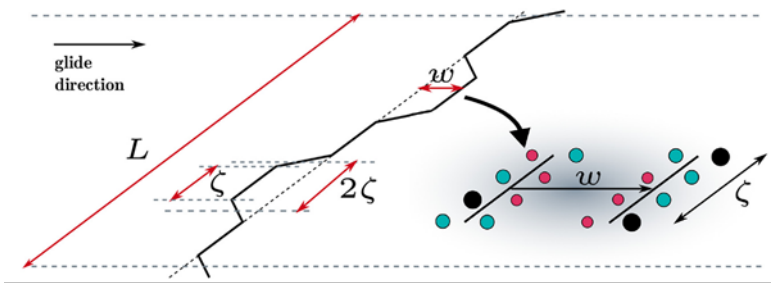


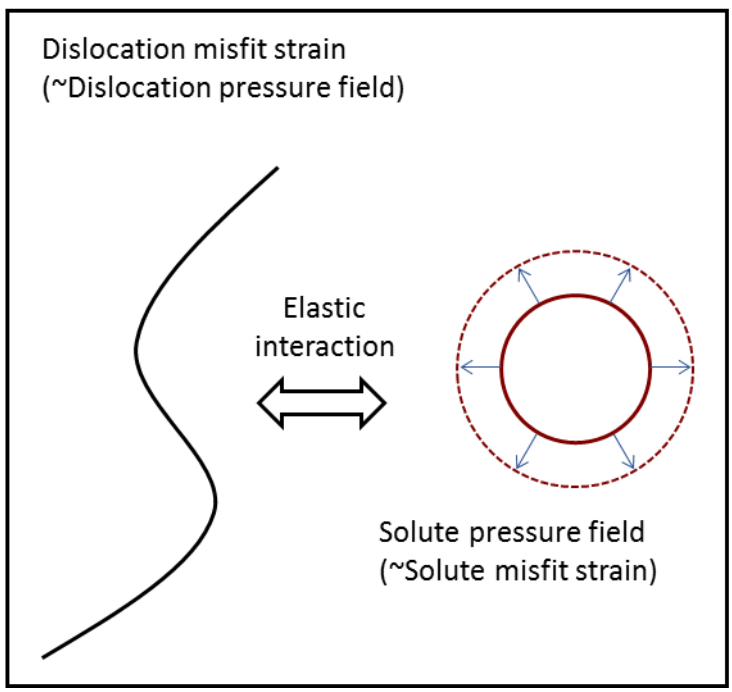


**Figure 3.2.** (A) Schematic of the low-energy wavy configuration of the dislocation as it moves through the random field of solutes in CCAs. Reprinted from [25] with permission through "Copyright Clearance Center". (B) Schematic of the elastic interaction between a dislocation and a solute atom.

## 3.2. Atomic-level pressure: Energy perspective

"What was lacking was a set of parameters to describe the local structure of a liquid and glass in such a way that they can be directly related to physical properties." – Takeshi Egami, 2011 [18]

The theory of atomic-level stress in amorphous alloy has been developed in Egami's pioneering works [18, 75-77]. As liquid and glass have the topological disorder, it was difficult to measure and describe the atomic structure and to predict the properties. Atomic-level stress theory has been developed in order to resolve the challenges: (1) Describe the local structure, (2) Predict the properties of disordered systems. In this section, Egami's early work for the derivation of atomic-level stress and the application to the properties of amorphous alloys are reviewed. The detailed description can be found in [18, 75-77].

In the case of crystalline alloys, most researches focus on the interaction between defects and atomic-level pressure of solute atoms. However, since amorphous alloys have topologically disordered structure without long-range order, it is difficult to define defects as in crystalline alloys. Instead, atomic-level pressure's energy-related aspects itself attracted more attention [75].

The total energy of the system $E_t$ can be described by total summation of central force potential $\mathrm{V}$ of every atomic pairs as

$$E_t = \sum_{ij} V(r_{ij}), \qquad \text{Eq. 3-7}$$

where $r_{ij}$ is the interatomic distance between atoms $i$ and $j$. When homogeneous strain is applied to the system, the total energy of the system $E_t$ is expanded as

$$E_t = E_0 + \Phi_1 \varepsilon^{\alpha\beta} + \frac{1}{2!}\Phi_2 \left(\varepsilon^{\alpha\beta}\right)^2 + \cdots, \qquad \text{Eq. 3-8}$$

where $\varepsilon^{\alpha\beta}$ is the applied strain and $\alpha$ and $\beta$ are Cartesian coordinates. $\Phi_1$ is the total stress in the system, which is the summation of $\sigma_i^{\alpha\beta}$, a stress tensor at atom i, as

$$\Phi_1 = \sum_i \Omega_i \, \sigma_i^{\alpha\beta}, \qquad \text{Eq. 3-9}$$

where $\Omega_i$ is the atomic volume of the ith atom. The stress tensor at atom i becomes

$$\sigma_i^{\alpha\beta} = \frac{1}{\Omega_i} \sum_j \frac{dV(r)}{dr}\Big|_{r_{ij}} \frac{r_{ij}^{\alpha} r_{ij}^{\beta}}{r_{ij}}, \qquad \text{Eq. 3-10}$$

Expanding $V(r)$ around the potential minimum at $a$, $\sigma_i^{\alpha\beta}$ becomes

$$\sigma_i^{\alpha\beta} \cong \frac{ab}{\Omega_i} \sum_j \left(\frac{r_{ij}}{a} - 1\right) r_{ij}^{\alpha} r_{ij}^{\beta}, \qquad \text{Eq. 3-11}$$

The $b$ is related to the slope of $V$, thus elastic constants. Atomic-level pressure of atom i $P_i$ is the trace of atomic-level stress as

$$P_i = -\frac{1}{3} Tr\left(\sigma_i^{\alpha\beta}\right). \qquad \text{Eq. 3-12}$$

If average atomic distance around the central atom is shorter than average of potential minimum distance ($r < a$), positive pressure arises at the central atom, expanding the size, pushing the neighbor atoms to minimize the energy (Figure 3.3.). On the other hand, if average atomic distance is longer than potential minimum ($r > a$), negative pressure arises at the central atom, shrinking the size, attracting the neighbor atoms (Figure 3.3.). It is consistent with elastic point of view in section 3.1.1.

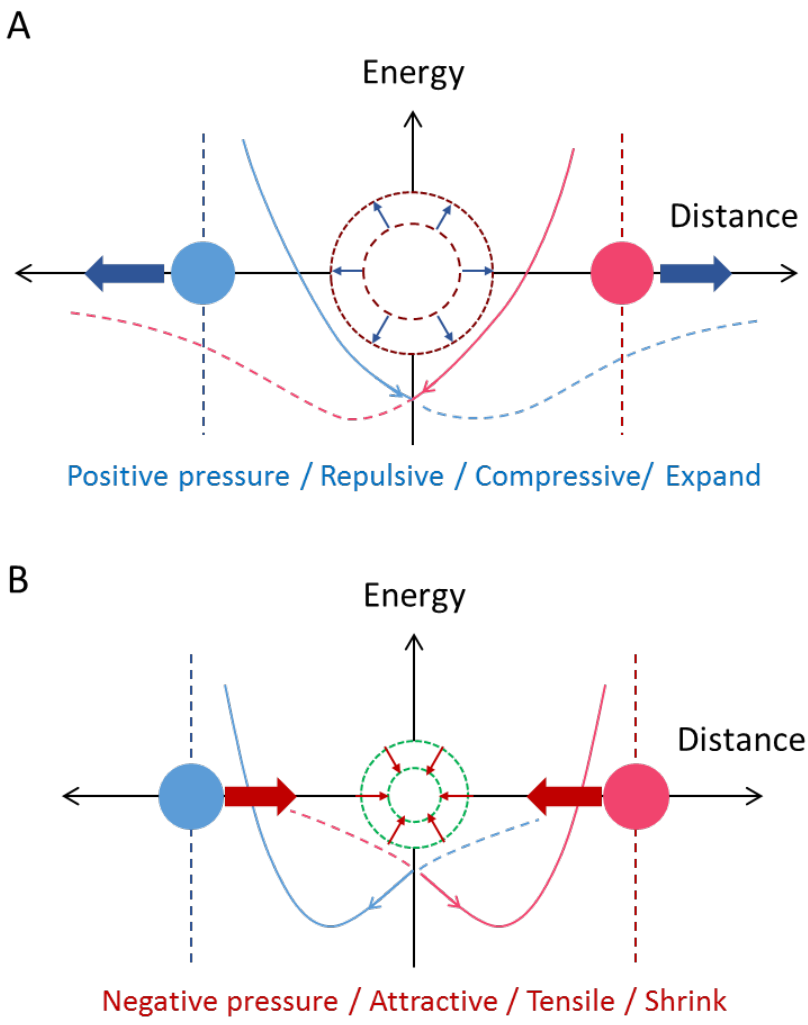


**Figure 3.3.** Schematics of atomic-level pressure in energy perspective. Atomic-level pressure reflects the average properties of interatomic potential between a center atom and surrounding atoms. (A) Positive pressure arises when the distance between a solute atom and surrounding atoms are shorter than the minimum energy. (B) Negative pressure arises when the distance between a solute atom and surrounding atoms are longer than the minimum energy.

## 3.3. Summary

In this chapter, the concept of atomic-level pressure is briefly introduced. There are two main streams of the research of atomic-level pressure. Classically, the theory of atomic-level pressure has been developed to explain the solid-solution strengthening effect of crystalline alloys. As the theories have been developed for dilute alloys, the atomic-level pressure is usually approximated by the size misfit of a solute element. More recently, the concept of atomic-level pressure is proposed to explain the topological instability and the mechanical properties of amorphous alloys. In this case, the atomic-level pressure is defined based on the view point of interatomic potential energy.

Most CCAs are crystalline and the pressure induced phenomena, such as solid solution strengthening, are consistent with classical view. However, a CCA is similar to amorphous alloys in that it has chemical complexity (complex atomic configurations). Therefore, it is important to integrate the advantages of both approaches used in each material in order to interpret the fundamental aspects of atomic-level pressure in a CCA.

# Chapter 4. Experimental procedures

## 4.1. Sample preparation

Samples in this thesis are prepared by conventional preparation methods. For preparing the master alloys, arc or induction melting was employed depending on the purposes. Arc melting was used to quickly manufacture the large number of samples. Induction melting was used to make large samples with specific compositions. The as-cast ingots were homogenized followed by grain refinement to optimize the microstructure.

### 4.1.1. Casting

- Arc melting: The alloy ingots lighter than 50g were prepared by arc melting method using metallurgical ingredients above 99.9 wt % purity under Ti-gettered high purity Argon atmosphere. The buttons were re-melted more than five times to ensure compositional homogeneity. When the alloy includes Mn or Cr, the elements were put under other constituents to minimize evaporation. The buttons were suction casted into the water-cooled copper mold with rectangular shape cavities.

- Induction melting: The alloy ingots heavier than 1kg were cast in a vacuum induction furnace using high purity elements above 99.8 wt % purity. This induction melting was employed to minimize the evaporation of Mn.After complete melting, the liquid alloy was poured into a Cu-mold of (20x50x150 $mm^3$).

### 4.1.2. Post processing

- Homogenization: The as-cast ingots were homogenized to remove the artifacts such as pores or elemental segregation. Arc melted ingots were homogenized at 1050~1200 °C for 24~48h in an Ar atmosphere and eventually quenched in water. For large induction melted ingots, in order to effectively remove the artifacts, the as-cast ingots were hot rolled at 900 °C with a rolling reduction ratio of 50%, followed by homogenization at 1200 °C for 3 h in an Ar atmosphere and eventually quenched in water.

- Grain refinement: The homogenized samples were cold rolled with a rolling reduction ratio of 70~85% followed by annealing above recrystallization temperature in an Ar atmosphere followed by water quenching. The reduction rate was 7% per pass from 0 to 50%, and 5% from 50% to the final reduction ratio. The diameter of the roll was 40cm and rolling speed was in the range of 1 to 3 rpm.

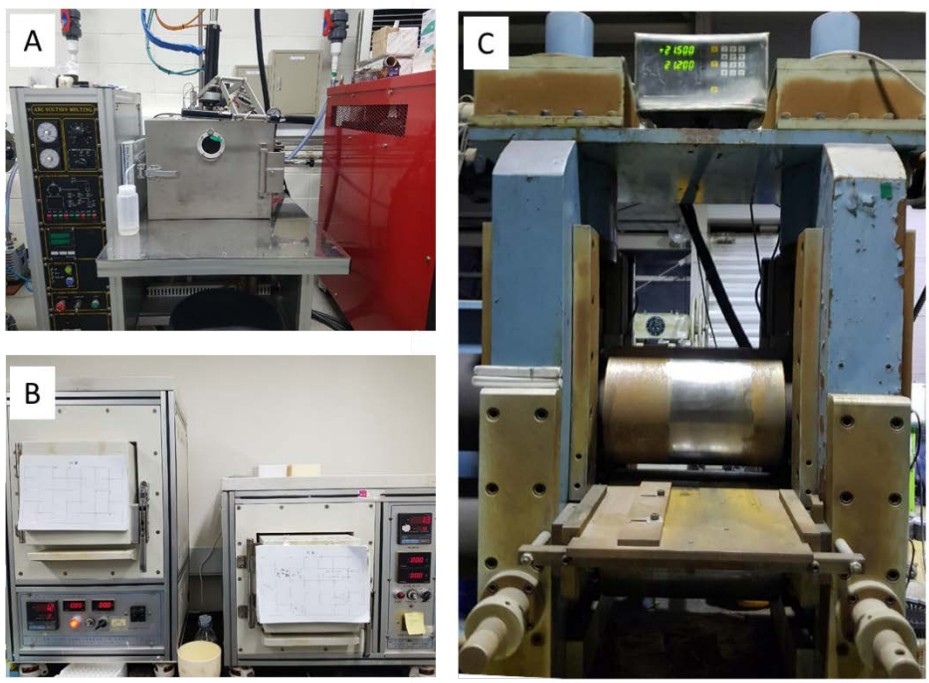


**Figure 4.1**. Machines for the sample preparation in this study. (A) Arc melting, (B) Box furnace, (C) Rolling machine.

## 4.2. Microstructural characterization

### 4.2.1. X-ray diffraction

Initial characterization of the alloys such as phase constitution and crystal structures and lattice parameters were measured by X-ray diffraction (XRD, Bruker, Germany) using monochromatic Co (λ=0.1789 nm) and Cu Kα (λ=0.1541 nm) radiation. XRD patterns collected from the bulk samples typically over 20-100° in 2θ, using a step size of 0.02°.

### 4.2.2. Extended X-ray Absorption Fine Structure

The bulk samples were mechanically ground into a ribbon below 15 μm-thickness, with SiC abrasive paper down to P4000. Extended X-ray Absorption Fine Structure (EXAFS) was carried out on the 7D beamline of the Pohang Accelerator Laboratory (PLS-II, 3.0 GeV, Pohang, Korea). The X-ray absorption spectra for Cr, Mn, Fe, Co and Ni of each sample were taken in a transmission mode under a He atmosphere. The higher-order harmonic rejection was achieved by detuning the Si(111) monochromator crystals to 15%–30% for each element edge. The beam size was 1.5×4 mm in the horizontal and vertical directions to include more than 100 grains for uniformity. The X-ray absorption spectra for Cr, Mn, Fe, Co, and Ni were taken in a transmission mode under ambient conditions. All element foils were measured as a reference to calibrate for any inconsistency in the energy shifts during the data collection. The obtained datasets were properly aligned and processed using the program Athena in the IFEFFIT 1.2.11d suite of software programs [78]. The smooth pre-edge function has been removed by linear extrapolation to avoid

instrumental background and absorption from other edges [79]. The resulting element-resolved absorption μ(E) was afterward normalized by using atomic-like absorption profiles. Careful fits to the measured data were carried out using the Artemis program included in the IFEFFIT software package. The fitted data for the first single scattering path included photoelectron waves with wave numbers of 3–10.5 $Å^{-1}$ and interatomic distances of 1–3 Å for each element (Cr, Mn, Fe, Co, Ni).

### 4.2.3. Scanning Electron Microscopy

The microstructures of the alloys were characterized using multiple Scanning Electron Microscopy (SEM) techniques, which are Energy-Dispersive X-ray Spectroscopy (EDS), Electron Backscattered Diffraction (EBSD), and Electron Channeling Contrast Imaging (ECCI). The chemical uniformity of 3d CCAs was investigated using a field emission SEM (SU-70, Hitachi) with EDAX detector. EBSD measurements were performed using a Zeiss-Crossbeam XB 1540 focused ion beam SEM with a Hikari camera and the TSL OIM data-collection software. Back-scattered electron (BSE) imaging and ECCI analyses were carried out using a Zeiss-Merlin instrument.

In chapter 7, we used coupled ECCI technique to observe the deformed microstructure of designed new CCAs. The coupling of ECCI with EBSD has been recently proven as a powerful technique to provide an efficient and fast approach to image crystal defects, such as dislocations, cells, twins and stacking faults, under controlled diffraction conditions by SEM [80-83]. The coupled ECCI in this thesis was performed in the following order:

1. Obtain an orientation of a specific grain (Euler angle) via EBSD.

2. Determine the rotation and tilt angles of the sample stage for Bragg condition considering the position of EBSD camera and BSE detector. This information can be determined with the help of the TOCA software.
3. Take the image in BSE mode. High acceleration voltage (~ 30kV) and short working distance (7~8mm) were used to obtain high contrast images.

### 4.2.4. Atom probe tomography

In Chapter 5, compositional homogeneity of CrMnFeCoNi CCA was probed by the atomic scale using atom probe tomography (APT, LEAP 5000 XS, Cameca Inc., Düsseldorf, Germany) to verify a single-phase solid solution in the present samples. Needle-shaped specimens for APT, having radii of curvature smaller than 100 nm, were produced using a focused ion beam (FEI Helios Nanolab 600i). A wedge-shaped piece of the sample was taken from the sample in a standard FIB lift-out procedure, placed on a Si micro-tip array. Then the samples were subjected to annular FIB milling procedure at a low acceleration voltage of 30 kV (0.23 nA). Final milling with 5 kV (40 pA) was done to minimize Ga + implantation into the samples. The APT data was acquired at a base temperature of 50 K, using voltage run, at a repetition rate of 200 kHz, and 15% amplitude, 1% target evaporation rate. The APT data was reconstructed using Cameca IVAS 3.6.10.

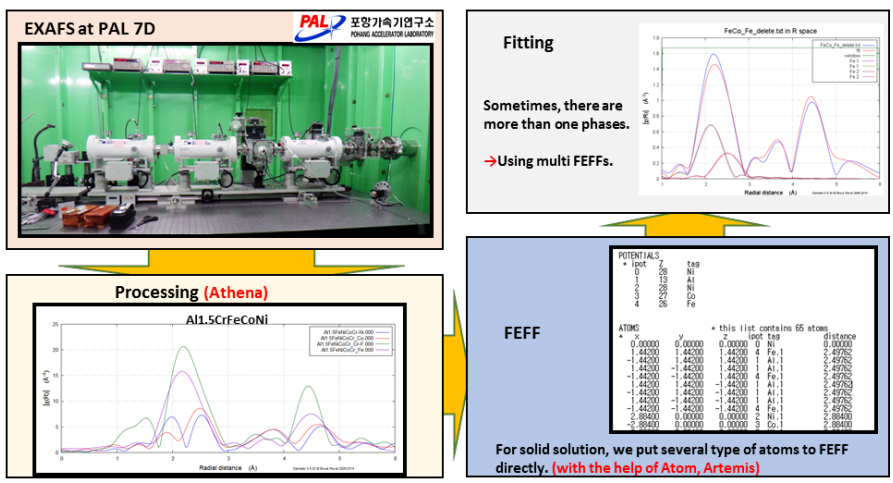


**Figure 4.2.** The measuring and fitting process of EXAFS.

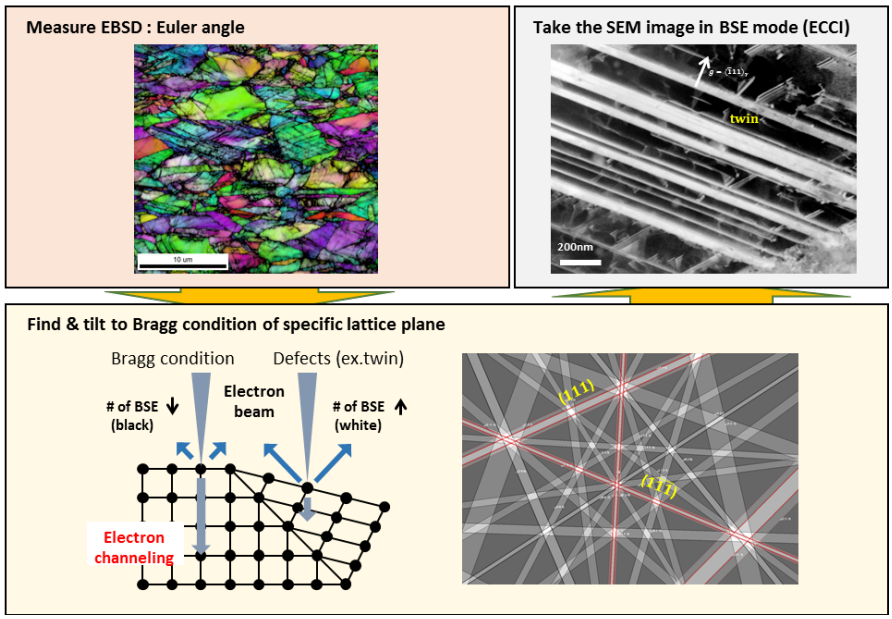


**Figure 4.3**. The measuring and analyzing process of ECCI.

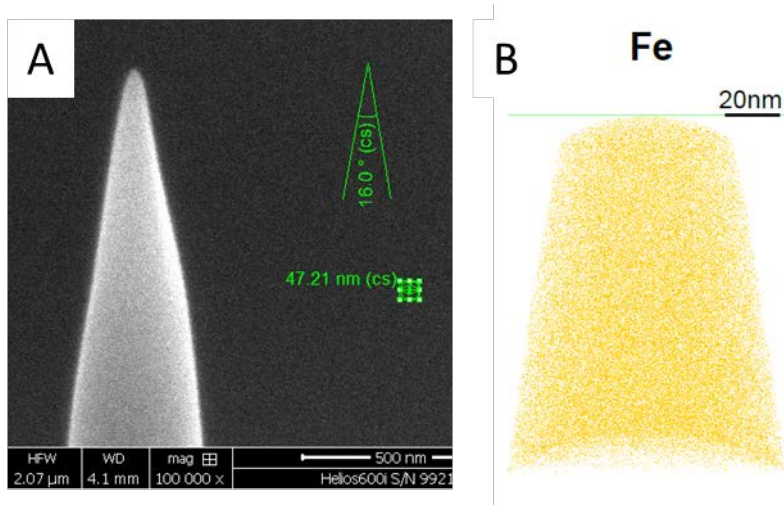


**Figure 4.4.** (A) SEM image of APT tip. (B) Three-dimensional APT tip reconstruction of Fe atom position in the tip.

## 4.3. Mechanical analysis

### 4.3.1. Tensile test

Flat specimens for tensile testing, with a thickness of from 1~2 mm, were sectioned from the recrystallized alloys by electrical discharge machining (EDM). Oxidation layer occurred during EDM cutting was removed by mechanical grinding. The gauge length and width of the tensile specimens were 10~25 mm and 2.5~3 mm, respectively. The size and shapes of the samples were determined depending on the purpose of the tensile tests. Uniaxial tensile tests were carried out (Instron 5967, Instron, Norwood, USA) at room temperature at the strain rate of $1\times10^{-3}$ $s^{-1}$. At least 3 samples for each material were tensile-tested to confirm reproducibility. The strain evolution during the tensile test was measured by AVE camera.

### 4.3.2. Digital image correlation

The local strain evolution during the tensile test was determined by digital image correlation (DIC) using the Aramis V6.3.0 software (Figure 4.6). DIC is the digital image analysis method based on the recognition of geometrical changes of surface patterns before and after straining. The surface of an un-deformed tensile sample is meshed as a reference image into square facets using sprayed patterns applied to a polished surface. Then every facet of the deformed image is mapped to find the best-fit facet of the reference image (registration process). Comparing with the reference image, the displacement field of the deformed image can then be calculated.

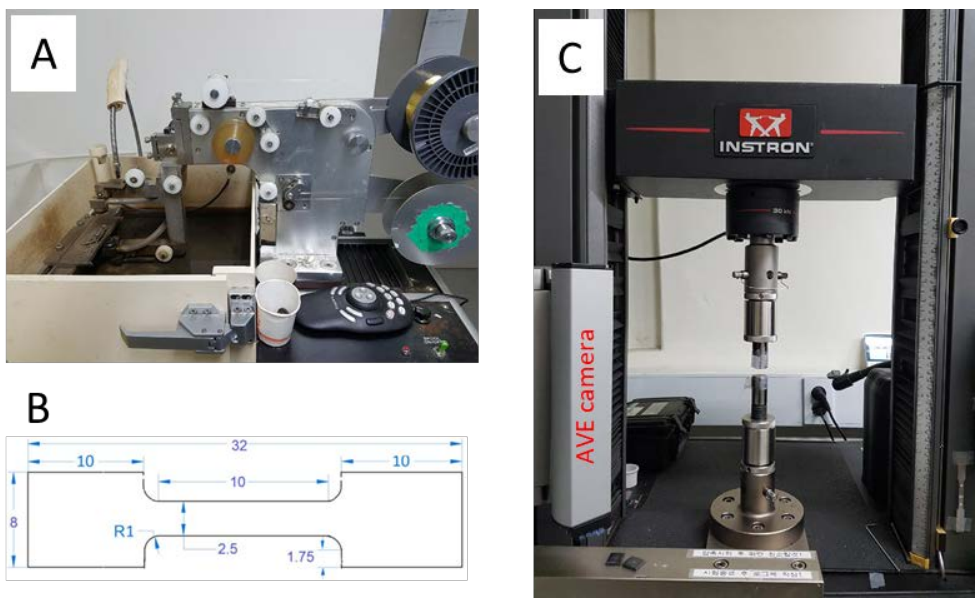


**Figure 4.5.** (A) The overview of electrical discharge machining used in this study. (B) An example of dog-bone type tensile sample. (C) The overview of tensile test machine.

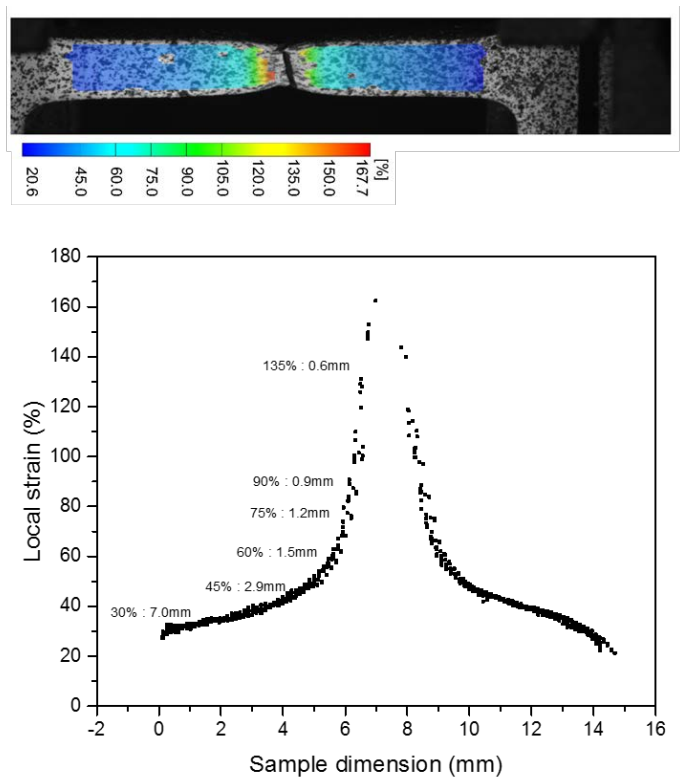


**Figure 4.6.** Digital image correlation strain map showing the local strain distribution of the tensile sample of equiatomic CrMnFeCoNi CCA after fracture.

## 4.4. Density functional theory calculation

First-principles calculations in Chapter 5 were carried out in the framework of DFT with the VASP code[84, 85]. The calculation was performed employing the generalized gradient approximation (GGA) in the Perdew–Burke–Ernzerhof (PBE) parametrization as exchange-correlation functional [86] and the projector-augmented wave (PAW) method [87] [88] as implemented in the VASP code. The electronic wave functions were expanded in terms of a plane-wave basis set with an energy cut-off of 350 eV. The chemical disorder was simulated utilizing the concept of special quasi-random structures (SQS) [89]. We compared 56 atom SQS (5×5×5 primitive cells) and 125 atom SQS (5×5×5 primitive cells), and used 125 atom SQS minimizing the nearest and next-nearest neighbor pair correlation functions. A 4×4×4 Γ-centered k-point mesh and the Fermi surface was smeared by using Methfessel–Paxton smearing method with a smearing parameter $\sigma$=0.1 eV. The DFT calculations have been performed by Duancheng Ma and analyzed together with Fritz Körmann, Blazej Grabowski and Gerard Paul Leyson.

First-principles calculations in Chapter 6 and Chapter 8 were done using the locally self-consistent multiple scattering methods using the DFT [77]. The geometry optimization was done using VASP code. The supercell size of the calculation was 256. The calculations of local stress were performed using LSMS in the atomic sphere approximation (ASA). DFT calculations have been performed by Sai Mu (geometry optimization) and Khorgolkhuu Odbadrakh (atomic-level pressure calculations) advised by Takeshi Egami in Oak Ridge National Laboratory.

# Chapter 5. Failure of structural analysis on the solid-solution strengthening of 3d CCAs

The physical, chemical, and mechanical properties of metallic solid solutions are affected by a difference in atomic size between the solvent and solute elements. In an alloy, the addition of the substitutional solute atom into the matrix causes a local distortion of the neighboring solvent atoms moving away from their ideal lattice positions and changes the magnitude of the macroscopic lattice constants of the system. The development of a strain field associated with these distortions results in an elastic interaction with other defects (e.g. gliding dislocations), giving rise to solid-solution strengthening [74, 90-92]. Therefore, the atomic size misfit, which is the local lattice distortion caused by solute atoms, is a critical factor for solid-solution strengthening and other properties related to atomic-level complexity of CCAs.

Solid solution strengthening models of CCAs have been developed mainly by Toda-Caraballo [50, 93] and Varvenne [25] by extension of a classical solid-solution strengthening model for binary systems. In both approaches, atomic size misfit is the critical factor to predict the solid-solution strength. Atomic size misfit of a solute in dilute alloys has been investigated to predict the strengthening potency and there is huge amount of experimental [94-96] and simulated results [72, 97-109]. However, the situation is complex in CCAs. Because every element is nearly equally concentrated, the solute and solvent atoms cannot be clearly defined in CCAs, and all atoms in CCAs have their own displacements from their ideal lattice positions resulting in severe lattice distortion. As a consequence, the definition and the method to measure the atomic size misfit of CCAs is difficult and has not been fully

investigated yet (See Section 2.2).

There are two ways of measuring atomic size misfit parameter in solid solutions. The first is volume size factor, which measures the changes of lattice parameters by XRD with respect to the compositional changes of solutes. The second is misfit strain, which measures the interatomic distances between solute and solvent atoms, which can be obtained from EXAFS. In this chapter, both methods have been performed to analyze the structure of CCAs and to obtain the atomic size misfit parameter. However, the obtained atomic size misfit parameter does not match well with the previously reported solid-solution strengths of 3d CCAs. The implication of the mismatch between atomic size misfit of CCAs and solid-solution strengths is discussed through the consideration of DFT calculation results.

## 5.1. Solid-solution strength of 3d CCAs

There are 11 CCAs that are equiatomic binary, ternary and quaternary alloys based on the elements Fe, Ni, Co, Cr, and Mn previously shown to be single-phase FCC solid solutions [110]. The solid-solution strength values of these alloys are measured by Wu [17] through tensile tests at different temperatures in the range 77-673K. For the tensile tests, the 3d CCAs with equiaxed microstructures and similar grain sizes (24–48 μm) are prepared.

Figure 5.1A shows the engineering stress vs. engineering strain curves of the equiatomic CrMnCoNi CCA as a function of temperature. In order to calculate the solid-solution strength, the temperature dependent yield strength in Figure 5.1B was fitted with [17]

$$\sigma_y(T) = \sigma_a exp\left(\frac{-T}{C}\right) + \sigma_b, \qquad \text{Eq. 5-1}$$

where $\sigma_a$, $C$ and $\sigma_b$ are fitting constants. Considering Peierls stress equation, $\sigma_a$ becomes Peierls stress at 0 K, which means the solid-solution strength in FCC alloys. The measured solid-solution strength of CCAs are displayed in Table 5.1.

**Table 5.1.** Measured solid-solution strength of the 3d CCAs [17].

| | Solid-solution strength (MPa) |
|---|---|
| $Ni_{100}$ (Ni) | 46 |
| $Co_{50}Ni_{50}$ (CoNi) | 130 |
| $Fe_{50}Ni_{50}$ (FeNi) | 341 |
| $Mn_{33.3}Co_{33.3}Ni_{33.3}$ (MnCoNi) | 302 |
| $Mn_{33.3}Fe_{33.3}Ni_{33.3}$ (MnFeNi) | 283 |
| $Cr_{33.3}Co_{33.3}Ni_{33.3}$ (CrCoNi) | 489 |
| $Fe_{33.3}Co_{33.3}Ni_{33.3}$ (FeCoNi) | 292 |
| $Cr_{25}Mn_{25}Co_{25}Ni_{25}$ (CrMnCoNi) | 491 |
| $Mn_{25}Fe_{25}Co_{25}Ni_{25}$ (MnFeCoNi) | 282 |
| $Cr_{25}Fe_{25}Co_{25}Ni_{25}$ (CrFeCoNi) | 443 |
| $Cr_{20}Mn_{20}Fe_{20}Co_{20}Ni_{20}$ (CrMnFeCoNi) | 423 |

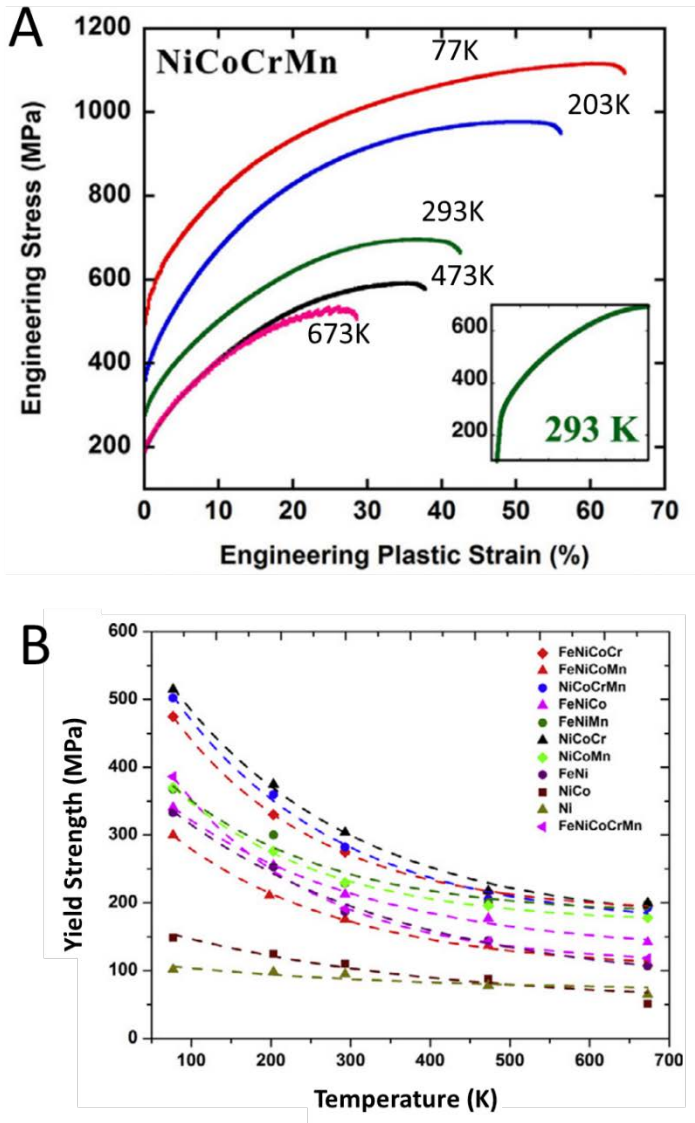


**Figure 5.1.** (A) Engineering stress vs. engineering plastic strain obtained in tension as a function of temperature for the equiatomic CrMnCoNi CCA. The representative insets show magnified regions around the yield points. (B) The temperature dependence of the 0.2% offset yield stress of the 3d CCAs. The dashed lines are curve fits to the form of Eq. 5-1. Reprinted from [17] with permission through "Copyright Clearance Center".

## 5.2. Structural analysis by XRD and EXAFS

### 5.2.1. Sample preparation

The single phase 3d CCAs from Ni to CrMnFeCoNi were prepared by arc melting followed by post processes (Table 5.2). The detailed process is described in Section 4.1. The annealing condition of each sample was taken from [17] for the formation of single FCC phase.

**Table 5.2.** Sample preparation method.

| Sample | Casting | Homogenization | Cold rolling | Annealing |
|---|---|---|---|---|
| Ni | Arc | 1200°C, 24h | 75% (4→1mm) | 800°C, 0.5h |
| CoNi | Arc | 1200°C, 24h | 75% (4→1mm) | 800°C, 1h |
| FeNi | Arc | 1200°C, 24h | 75% (4→1mm) | 900°C, 1h |
| MnCoNi | Arc | 1100°C, 24h | 75% (4→1mm) | 900°C, 1h |
| MnFeNi | Arc | 1100°C, 24h | 75% (4→1mm) | 900°C, 1h |
| CrCoNi | Arc | 1200°C, 24h | 75% (4→1mm) | 1000°C, 1h |
| FeCoNi | Arc | 1200°C, 24h | 75% (4→1mm) | 900°C, 1h |
| CrMnCoNi | Arc | 1100°C, 24h | 75% (4→1mm) | 1000°C, 1h |
| MnFeCoNi | Arc | 1100°C, 24h | 75% (4→1mm) | 1000°C, 1h |
| CrFeCoNi | Arc | 1200°C, 24h | 75% (4→1mm) | 900°C, 1h |
| CrMnFeCoNi series | Induction | Hot rolled (50%) 1200°C, 3h | 85% (10→1.5mm) | 900°C, 3min |

### 5.2.2. Measurement of misfit parameter by XRD

In dilute alloys, the volume size factor $\Omega_{sf}$ is defined as [94]

$$\Omega_{sf} = \left(\frac{\Omega_B^* - \Omega_A}{\Omega_A}\right). \quad \text{Eq. 5-2}$$

where $\Omega_A$ is the atomic volume of solvent A and $\Omega_B^*$ is obtained by a linear extrapolation of the volume plot to 100% solute B. Eq. 5-2 can be expressed in the differential form as

$$\Omega_{sf} = \frac{1}{\Omega_A} \cdot \frac{\partial \Omega}{\partial \mathrm{c}}, \quad \text{Eq. 5-3}$$

where c is the solute concentration. Thus, the volume size factor represents the rate of change of atomic volume with solute concentration c. What we can get from the XRD experiment is the linear derivative of the lattice constant against the solute concentration. In this case, the misfit parameter $\delta$, is defined as

$$\delta = \frac{1}{a_0} \cdot \frac{\partial a}{\partial c}, \quad \text{Eq. 5-4}$$

where $\mathrm{a}_0$ is the lattice constant of pure host element and $\mathrm{a}$ is the lattice constant of the solid solution. Considering the relationship between atomic volume and lattice constant $a$ ($\Omega_A = a^3/4$), $\Omega_{sf}$ becomes

$$\Omega_{sf} = \frac{1}{a_0^3} \cdot \left(\frac{\partial a^3}{\partial \mathrm{c}}\right) = 3\delta. \quad \text{Eq. 5-5}$$

We applied the same process in order to measure the volume misfit parameter in Eq. 3-5. The lattice parameters of 3d CCAs are measured by a high energy x-ray in advanced photon source, Argonne National Laboratory, as shown in Table 5.3. The atomic sizes of each element are calculated applying Vegard's law [111]

assuming that the average volume of an alloy is a linear superposition of its constituent parts as

$$\bar{V} = \sum_{n} c_n \bar{V}_n, \qquad \text{Eq. 5-6}$$

where $c_n$ is the concentration of element n and $\bar{V}_n$ is the volume of element n in the alloy. For accurate fitting, only lattice parameters of 4 and 5 component alloys are used. The results are summarized in Table 5.4 and the volume in alloy are Cr: 11.44 Å$^3$, Mn: 12.59 Å$^3$, Fe: 11.37 Å$^3$, Co: 11.28 Å$^3$, and Ni: 11.53 Å$^3$.

Figure 5.2 shows that the quality of the fits that are assessed by comparing the predicted lattice parameter from the experimental values. The fits for 4 and 5 components show good correlation, but, the fits for 1, 2, and 3 component alloys are not reliable, which implies that there is a big variance between the atomic volumes in CCAs.

In dilute alloys, the lattice constants and average atomic volumes of the solid solutions vary linearly with the solute concentrations [112]. This is because the solute atoms are surrounded by the same solvent atoms. However, in concentrated solid solutions, the amount of solute clusters and the local configurations around solute atoms change according to solute concentrations. As a result, the change in lattice parameter with solute concentration is no longer linear. [94]. Thus, a linear extrapolation should be made in a very narrow concentration region to reliably approximate the atomic sizes. This shows the limitation of measuring average atomic sizes by concentration-extrapolation methods in CCAs.

**Table 5.3.** Measured lattice parameters of the 3d CCAs.

| | Alloy | Lattice constant at 300K (Å) |
|---|---|---|
| 1 | Ni | 3.524 |
| 2 | $Co_{50}Ni_{50}$ | 3.536 |
| 3 | $Fe_{50}Ni_{50}$ | 3.587 |
| 4 | $Mn_{33.3}Co_{33.3}Ni_{33.3}$ | 3.605 |
| 5 | $Mn_{33.3}Fe_{33.3}Ni_{33.3}$ | 3.621 |
| 6 | $Cr_{33.3}Co_{33.3}Ni_{33.3}$ | 3.565 |
| 7 | $Fe_{33.3}Co_{33.3}Ni_{33.3}$ | 3.574 |
| 8 | $Cr_{25}Mn_{25}Co_{25}Ni_{25}$ | 3.604 |
| 9 | $Mn_{25}Fe_{25}Co_{25}Ni_{25}$ | 3.602 |
| 10 | $Cr_{25}Fe_{25}Co_{25}Ni_{25}$ | 3.573 |
| 11 | $Cr_{20}Mn_{20}Fe_{20}Co_{20}Ni_{20}$ | 3.597 |
| 12 | $Cr_{20}Mn_{14}Fe_{26}Co_{26}Ni_{14}$ | 3.591 |
| 13 | $Cr_{20}Mn_{10}Fe_{30}Co_{30}Ni_{10}$ | 3.582 |

**Table 5.4.** Fitted atomic sizes and atomic volumes of Cr, Mn, Fe, Co, Ni.

| | Cr | Mn | Fe | Co | Ni |
|---|---|---|---|---|---|
| Atomic size (Å) | 3.577 | 3.693 | 3.569 | 3.56 | 3.586 |
| Atomic volume ($Å^3$) | 11.442 | 12.592 | 11.365 | 11.280 | 11.528 |

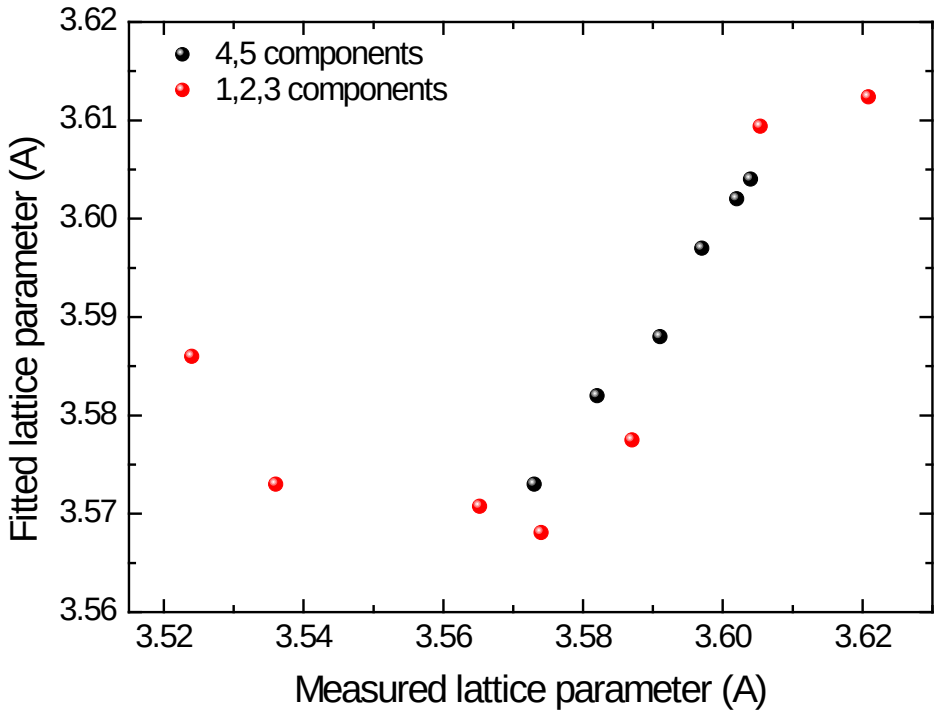


**Figure 5.2.** Comparison between fitted lattice parameters and measured lattice parameters of 3d CCAs. The fitting is performed using 4 and 5 component alloys.

### 5.2.3. Measurement of misfit strain by EXAFS

In order to avoid inaccuracies with the concentration-extrapolation method of the lattice parameter, we applied the EXAFS method that can directly measure the average atomic sizes. In dilute alloys, the atomic radius of solute B can be obtained by [112, 113]

$$r_B = d - \frac{d_0}{2}, \qquad \text{Eq. 5-7}$$

where $d$ is the interatomic distance between a solute B atom and a solvent A atom in the A-B solution. In addition, $d_0$ is the interatomic distance in pure A atom based on the fact that all solute atoms are surrounded only by unlike solvent atoms. In CCAs, on the other hand, many different elements can be neighboring atoms, but, it is difficult to measure the individual atomic pairs as long as the consisting elements have similar atomic sizes. Therefore, to reduce the number of variables, we calculated average bond lengths of each element, called effective atomic size. Furthermore, inelastic scattering and multiple scattering in a disordered system cannot be accurately estimated by the DFT. To avoid difficulties mentioned previously, only the first shell (nearest neighbor atoms) was fitted, which consists of only a single scattering path.

The measured bond lengths are plotted at Figure 5.3A and the error of bond length is the statistical error from fitting the Gaussian function. The lattice parameter was calculated by averaging the bond lengths of each edge. We concluded that the measured effective atomic sizes using EXAFS are accurate by comparing with the lattice parameter measured by XRD (Figure 5.3B).

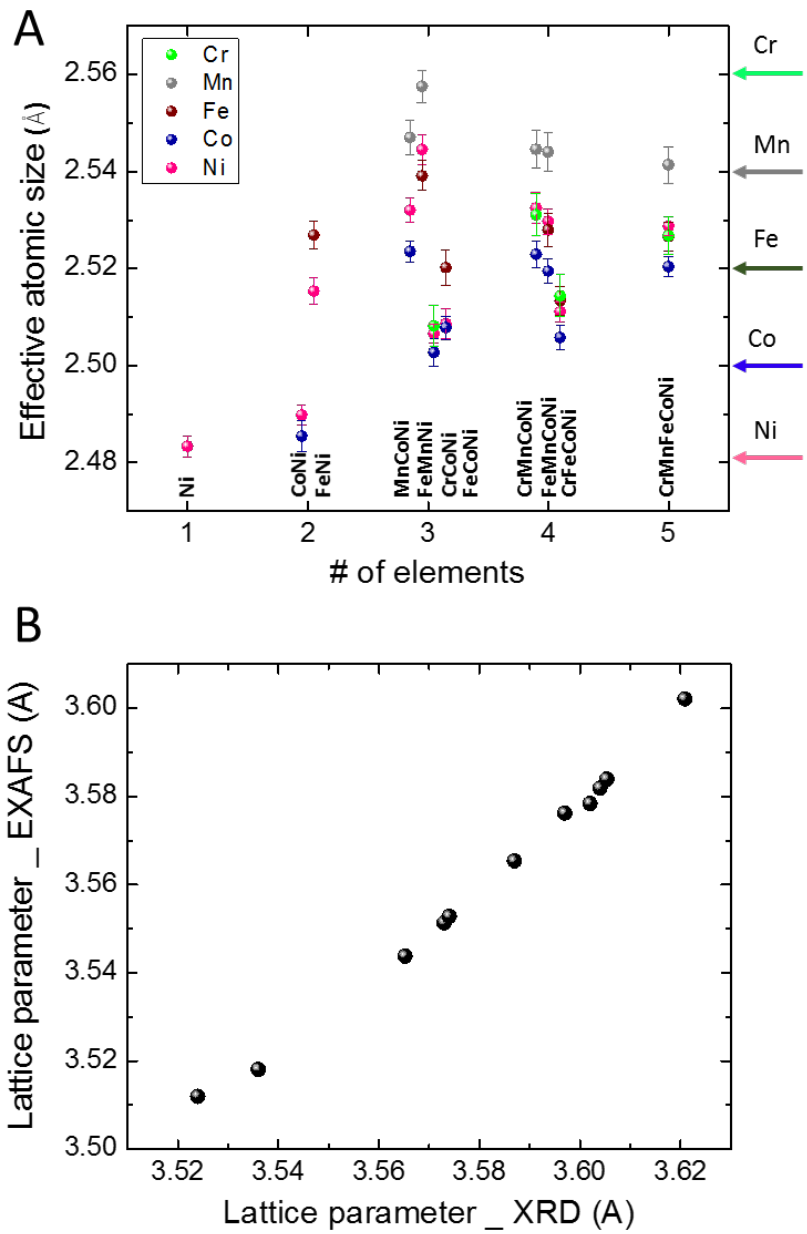


**Figure 5.3.** (A) Effective atomic sizes of each elements. (B) The comparison of lattice parameter obtained by EXAFS and XRD.

We calculated the solid-solution strength of the 3d CCAs as shown in Table 5.5 inputting the measured effective atomic sizes to Eq. 3-6. The individual atomic volumes were calculated with $4\bar{V} = a^3 = 2\sqrt{2}r^3$, where $r$ is the effective atomic radius and $\bar{V}$ is the corresponding effective atomic volumes.

There are two interesting features of the theoretically calculated solid-solution strength. First, 3d CCAs containing Cr and Mn show deviation from the linearity. Cr containing alloys usually have larger strength than predicted, while Mn containing alloys have smaller strength. Second, the absolute values from theoretical calculation are one order smaller than the experimentally measured values. This means that there may be other factors that contribute to the solid-solution strength more than the simple deviation of effective atomic volumes inside the CCAs. In particular, $\sigma_{\Delta V_n}^2$ in Eq. 3-6, which is the variance in atomic volumes due to the fluctuation in local atomic configurations, is ignored in the present approach due to the lack of data.

**Table 5.5.** Experimental data on the fcc Ni-Co-Fe-Cr-Mn family CCAs. Burgers vector b and shear modulus are measured at room temperature [17].

| | b (Å) | Poisson ratio | Shear modulus (GPa) | Misfit volume ($Å^3$) | Solid solution strength (shear) (MPa) | Solid-solution strength (yield) (MPa) |
|---|---|---|---|---|---|---|
| Ni | 2.483 | 0.31 | 76 | 0 | 0 | 0 |
| CoNi | 2.488 | 0.29 | 84 | 0.0287 | 1.94 | 5.94 |
| FeNi | 2.521 | 0.34 | 62 | 0.0776 | 5.95 | 18.22 |
| MnCoNi | 2.534 | 0.23 | 77 | 0.1324 | 10.73 | 32.83 |
| MnFeNi | 2.547 | 0.24 | 73 | 0.1066 | 7.68 | 23.49 |
| CrCoNi | 2.506 | 0.3 | 87 | 0.0301 | 2.15 | 6.59 |
| FeCoNi | 2.512 | 0.35 | 60 | 0.0760 | 5.86 | 17.93 |
| CrMnCoNi | 2.533 | 0.25 | 78 | 0.1055 | 8.51 | 26.05 |
| MnFeCoNi | 2.530 | 0.22 | 77 | 0.1199 | 9.19 | 28.13 |
| CrFeCoNi | 2.511 | 0.28 | 84 | 0.0444 | 3.26 | 9.99 |
| CrMnFeCoNi | 2.529 | 0.26 | 80 | 0.0936 | 7.71 | 23.59 |

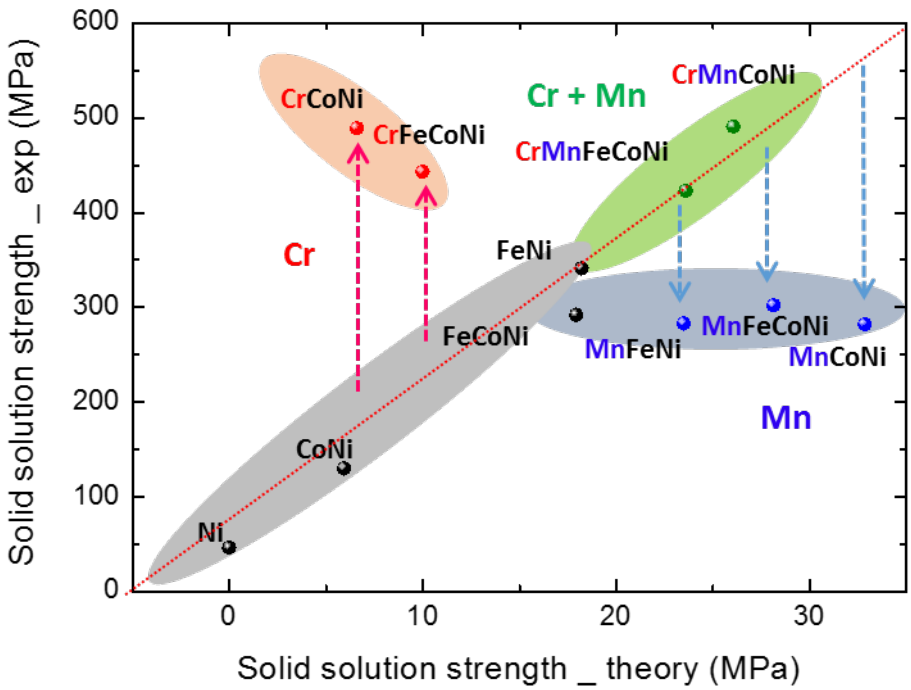


**Figure 5.4.** Experimentally measured solid-solution strength of 3d CCAs plotted against theoretically calculated solid-solution strength using volume misfit obtained from EXAFS measurement.

## 5.3. DFT Simulation for local atomic structure

As discussed in Section 5.2, there may be an additional contribution for the solid-solution strength rather than the mean misfit volume of elements, due to the fluctuations in the misfit volumes themselves. In this work, we, therefore, conducted a combined experimental (EXAFS) and theoretical (DFT) study to investigate element resolved the local fluctuation of atomic volumes and its impact the solid-solution strengthening. As an application, we have chosen the well-studied prototype equiatomic FCC FeCoNiCrMn CCA, also known as Cantor alloy.

### 5.3.1. Homogeneity of CrMnFeCoNi CCA

Recent findings showed phase decomposition in the CrMnFeCoNi CCA [114]. Thus, before measuring the EXAFS, we probed the compositional homogeneity of present CrMnFeCoNi CCA at the atomic scale using APT. The results shown in Figure 5.5A reveal no indication of any compositional decomposition on the nm-scale. The normalized homogenization parameter μ values or p-values obtained by a frequency distribution analysis (Figure 5.5B) are close to 0 for all five elements, revealing a random distribution of the involved elements in the present alloy. This is a direct consequence of single phase formation of the present CrMnFeCoNi CCA.

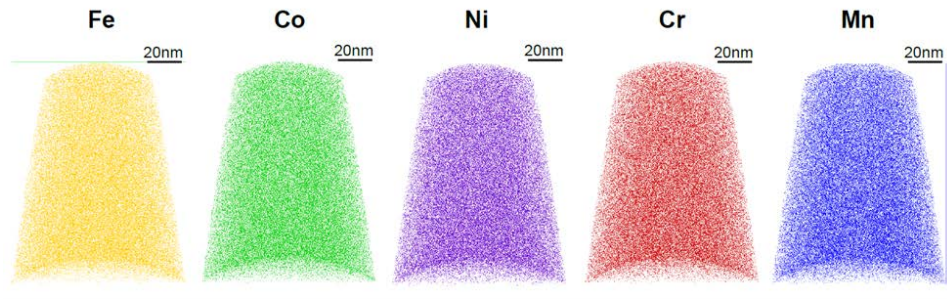


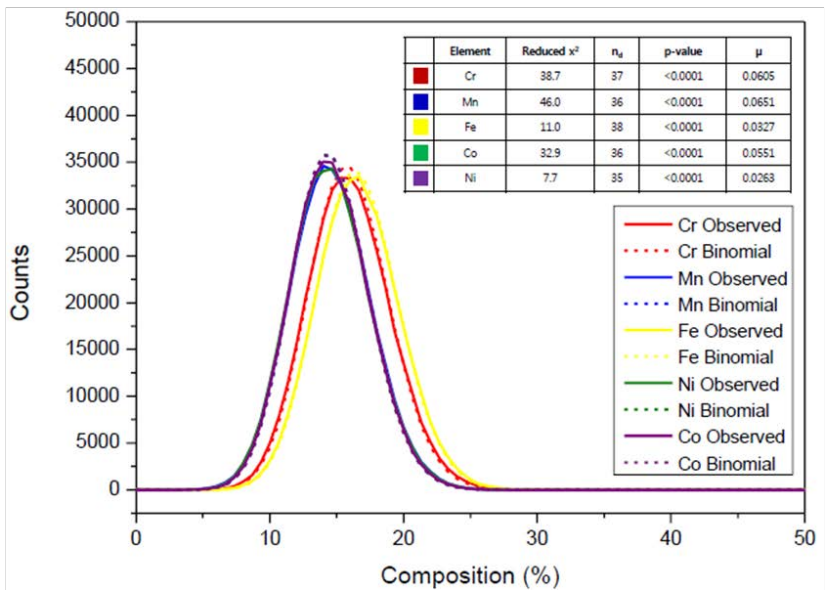


**Figure 5.5.** APT results showing single phase formation of CrMnFeCoNi CCA. Reprinted from [23].

### 5.3.2. Comparison between DFT calculated and EXAFS measured bond length

From the different SQS supercell realizations, 1500 individual element-specific bonds for each of the five constituent were extracted for the reliable statistics of the distribution of bond lengths (Figure 5.6A). As an example, a few of the bonds for Mn are noted in Figure 5.6A, and a histogram for the distribution of local bond distortion (variation of local bond lengths) of Mn is shown in Figure 5.6B. The obtained bond distribution was fitted with a Gaussian function to quantify the mean value as well as the variation (standard deviation) of local bond length. The experimentally-measured averaged distortion by EXAFS is indicated by the red solid line. The variation of local bond length is much larger than the actual deviation between theory and experiment for the mean averaged distortions.

The distribution of bond distortion, i.e., bond length, of all individual elements are shown in Figure 5.7A–E. In Figure 5.7F-J, the calculated mean bond lengths from DFT calculation derived from the Gaussian fits (open black circles), as well as the standard mean values (filled black circles) agree well with the experimentally measured bond length by EXAFS (red open squares). Average values of measured bond lengths of individual elements by EXAFS (~3.576Å) were used as a global mean bond length. The agreement between DFT calculated and EXAFS measured mean bond lengths (or distortions), which we have found for the magnetic results, is completely lost when comparing to the non-spin polarized calculations. This means that magnetism significantly affects the local bond fluctuations and is required for realistic simulations.

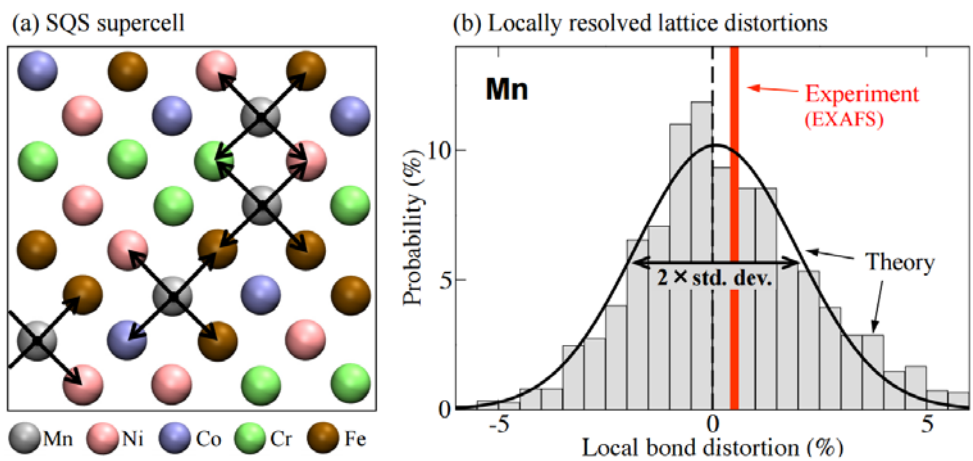


**Figure 5.6.** (A) Projection of the employed special quasi-random structure (SQS) supercell onto the (100) plane. (B) Lattice distortion historgram of Mn-bonds in FeCoNiCrMn, based on 1500 evaluated Mn-bonds. The experimentally-measured averaged distortion by EXAFS is indicated by the red solid line. Reprinted from [23].

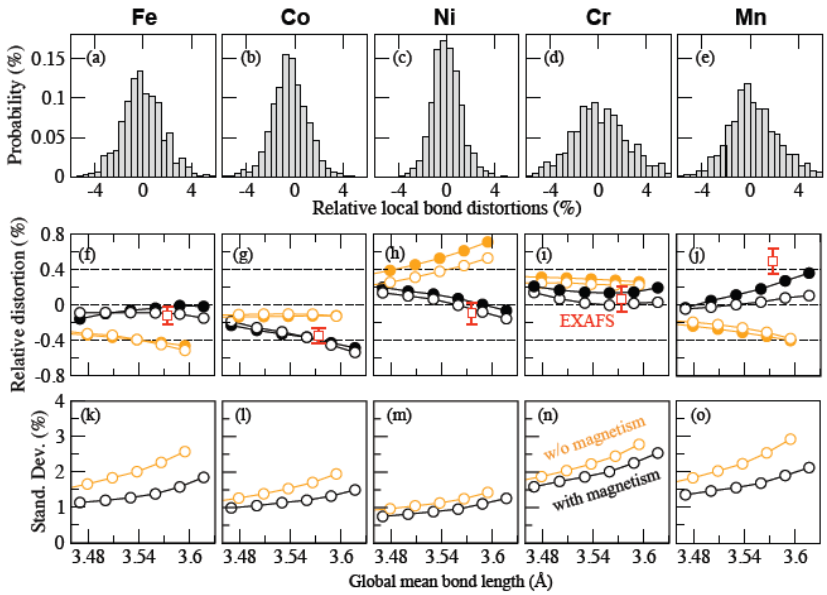


**Figure 5.7.** (A–E) Distribution of relative local bond distortions for Fe, Co, Ni, Cr and Mn in total 3750 individual atomic bonds. (F–J) Experimental EXAFS data is marked with red open squares and compared to the theoretical mean bond length (black filled circles), as well as the mean value derived from a Gaussian fit (black open circles) for different volumes. Non-spin polarized calculations are shown for comparison (open and filled orange circles). (K–O) Standard deviation of the Gaussian fits of the pair distribution of relative bond distortion in (A-E) revealing the much larger local bond fluctuations compared to actual mean, averaged values. Reprinted from [23].

### 5.3.3. Elemental and Configurational deviation of bond length

In Figure 5.7F–O, we show the mean values of the bond lengths and the corresponding standard deviations obtained by Gaussian fitting of bond distribution in Figure 5.7A-E. A direct outcome of this comparison is the relatively small values of mean distortion (<1%), compared to the fluctuation (standard deviation) of the individual bond lengths caused by the difference of atomic configurations (1~2%). In other words, the overall magnitude of the local bond fluctuations (configurational deviation) is an order of magnitude larger than the deviation of averaged bond lengths of each element (elemental deviation). This observation has significant implications for the solid-solution strengthening mechanism in CCAs according to Eq.3-6. In dilute alloys, atomic size misfit parameter usually approximated to the average misfit volume of the solute element ($\Delta\bar{V}$ in Eq.3-6). However, Figure 5.7 shows that the fluctuation of the local bond length (i.e. local volume fluctuation, $\sigma^2_{\Delta V_n}$ in Eq.3-6) from configurational difference cannot be ignored.

In order to further elucidate the role of individual elements, we show in Table 5.6 the element-element resolved mean bond distortions, i.e., elemental deviation, and corresponding standard deviations, i.e., configurational deviation. Interestingly, atomic bonds containing Cr or Mn have strong local bond fluctuations. This indicates that CCAs with Cr and Mn can have significant solid-solution strengthening effects, although the overall mean distortions appear to be rather small. This can explain the failure of structure-based analysis of solid-solution strengthening of CCAs through EXAFS measurement.

**Table 5.6.** Element-resolved mean bond distortions and standard deviation of the fcc FeCoNiCrMn HEA. Cr and Mn induce strong local bond fluctuations for all considered elemental pairs [23].

| Mean distortion (in %) | | | | | |
|---|---|---|---|---|---|
| | Cr | Mn | Fe | Co | Ni |
| Cr | 0.66 | 0.54 | 0.18 | -0.67 | 0.02 |
| Mn | 0.54 | 0.71 | 0.22 | -0.22 | 0.12 |
| Fe | 0.18 | 0.22 | 0.34 | -0.72 | -0.06 |
| Co | -0.67 | -0.22 | -0.72 | -0.43 | -0.08 |
| Ni | 0.02 | 0.12 | -0.06 | -0.08 | 0.04 |
| Standard deviation (in % of distortion) | | | | | |
| | Cr | Mn | Fe | Co | Ni |
| Cr | 3.06 | 3.01 | 2.09 | 1.88 | 1.38 |
| Mn | 3.01 | 2.74 | 1.99 | 1.40 | 1.16 |
| Fe | 2.09 | 1.99 | 1.58 | 1.21 | 1.15 |
| Co | 1.88 | 1.40 | 1.21 | 1.14 | 1.03 |
| Ni | 1.38 | 1.16 | 1.15 | 1.03 | 0.89 |

## 5.4. Summary

In this chapter, we analyzed the local structure of 3d CCAs by XRD and EXAFS to obtain an atomic size misfit value, which is the key factor for the elastic interaction energy of solutes, i.e., solid-solution strengthening. However, the predicted solid-solution strengths from the structural information do not match with the experimentally measured ones. In order to interpret this mismatch, we calculated the atomic structure of CrMnFeCoNi CCA using DFT and compared the local fluctuation of bond lengths (configurational deviation) and the deviation of macroscopic mean bond lengths of each element (elemental deviation). The local fluctuations are an order of magnitude larger than the deviation of mean values, indicating that the fluctuation of local bond lengths due to the difference in atomic configurations should not be ignored for the prediction of solid-solution strengthening. Thus, ‘the difference in the element-specific average property among two (or more) elements in solid solution’ and ‘the variations around the average due to dissimilar local atomic environments (configurations) in one element’ should be defined separately as different degrees of complexity in CCAs. This is considered to be a major feature that distinguishes CCAs from existing dilute alloys.

# Chapter 6. Solid-solution strengthening of CCAs – Atomic-level pressure

It is shown in Chapter 5 that a classical structure-based analysis of solid-solution strengthening of CCAs is associated with several limitations due to the complex atomic environments involved. In order to address this challenge, a set of new parameters with the following advantages is needed:

1. The parameters should be directly related to physical properties such as the solid-solution strengthening and the degree of complexity.
2. The factors that influence the parameters should be easily identified.
3. Practically, environmental information pertaining to the parameters should be predictable using elemental information which can be measured by experiments.

In this chapter, the solid-solution strengthening of CCAs is analyzed using an atomic-level pressure concept by both simulations and experiments. The atomic-level pressure calculation was done using a locally self-consistent multiple scattering methods based on DFT (See Chapter 4.4). By applying atomic-level pressure, we found that solid-solution strengthening in 3d CCAs originates from the deviation of atomic-level pressure due to charge transfers among the elements. The binary VNi explored here to investigate the validity of our finding showed higher yield strength levels than CrCoNi and CrMnFeCoNi CCAs. As a result, we suggest the complexity of atomic-level pressure as a new category of atomic-level complexity reflecting the fluctuation of local-atomic potential.

## 6.1. Deviation of the atomic-level pressure and solid-solution strengthening

Figure 6.1 shows the DFT-calculated atomic-level pressures on each element in the 3d CCAs in Table 5.2, from CoNi to CrMnFeCoNi, plotted against the local atomic volume, the size of the Wigner-Seitz cell. The order of the mean atomic volumes from the calculation is in good agreement with the experimental results from EXAFS measurements. The ranges of the atomic volume and atomic-level pressure vary depending on the alloys used.

The pressure of the central atom is determined by the interaction with the surrounding atoms. As shown in Figure 6.1, all atoms in CCAs are under different pressures and have different volumes, even when in the same element. The variance of the pressure represents the complex atomic configurations of CCAs.

In the equilibrium state, the total energy of the system is at its minimum; thus, the total average atomic-level pressure $\langle P \rangle$, which is increased in terms of its energy due to the volume strain, is zero [18], as determined by

$$\langle P \rangle = \frac{\sum_{i=1}^{m} \sum_{j=1}^{n} P_{ij}}{mn} = 0, \qquad \text{Eq. 6-1}$$

where $P_{ij}$ is the local atomic-level pressure of element i at atomic site j, $m$ is the number of elements, and $n$ is the number of atoms of each element. In consequence, the elastic strain energy $E_{ela}$ of the system can be described by the deviation (variance) of the pressure $\sigma^2(P)$ as

$$E_{ela} \propto \langle P^2 \rangle \cong \langle P^2 \rangle - \langle P \rangle^2 = \sigma^2(P). \qquad \text{Eq. 6-2}$$

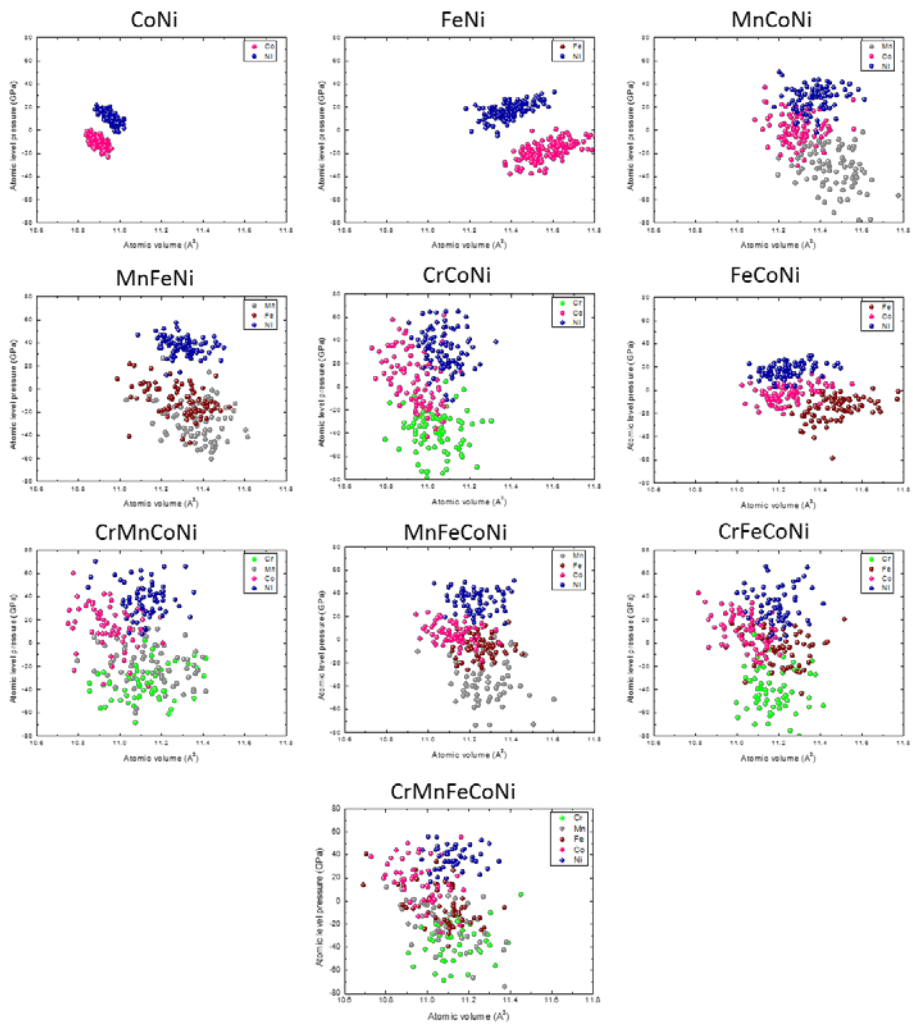


**Figure 6.1.** Atomic-level pressure versus atomic volume relation in 3d CCAs including CoNi, FeNi, MnCoNi, MnFeNi, CrCoNi, FeCoNi, CrMnCoNi, MnFeCoNi, CrFeCoNi, CrMnFeCoNi.

In Figure 6.2, the zero temperature flow stress, i.e., the solid-solution strength, of the 3d CCAs are plotted against $\sigma(P)$. The linear relationship clearly shows that the solid-solution strengthening in these alloys originates from the elastic strain energy of highly concentrated solute atoms. The elastic strain energy from the atomic-level pressure of the solutes interacts with the elastic strain energy of the dislocations. This interaction is based on a reduction of the strain energy of each sources; e.g., dislocations would be attracted to energetically favorable fluctuations of the solutes, and vice versa. During the gliding, a dislocation should overcome the energy barrier which originates from the difference in the potential energies between favorable and an unfavorable solute configurations. The energy barrier is proportional to the standard deviation of the potential energy change and thus the deviation of elastic interaction energies [71]. Therefore, as the deviation of the pressure increases, the interaction between dislocations and solutes increases, inhibiting the motion of dislocations.

An interesting point in Figure 6.2 is that CrCoNi has the largest deviation of the pressure and solid-solution strength. Previously, it was reported that the strength and toughness of CrCoNi exceed those of all high-entropy alloys and most multi-phase alloys [4]. The authors insisted that this is attributed to the continuous steady strain hardening from pronounced dislocation activity and deformation-induced nano-twinning. However, no detailed discussion of more fundamental reasons was presented, in particular for the large solid-solution strengthening effect in this alloy. Here, it is shown that a large deviation of the atomic-level pressure causes the high strength in this alloy. Thus, one of the most important characteristics contributing to the solid-solution strengthening is the deviation (i.e. complexity) of atomic-level pressure.

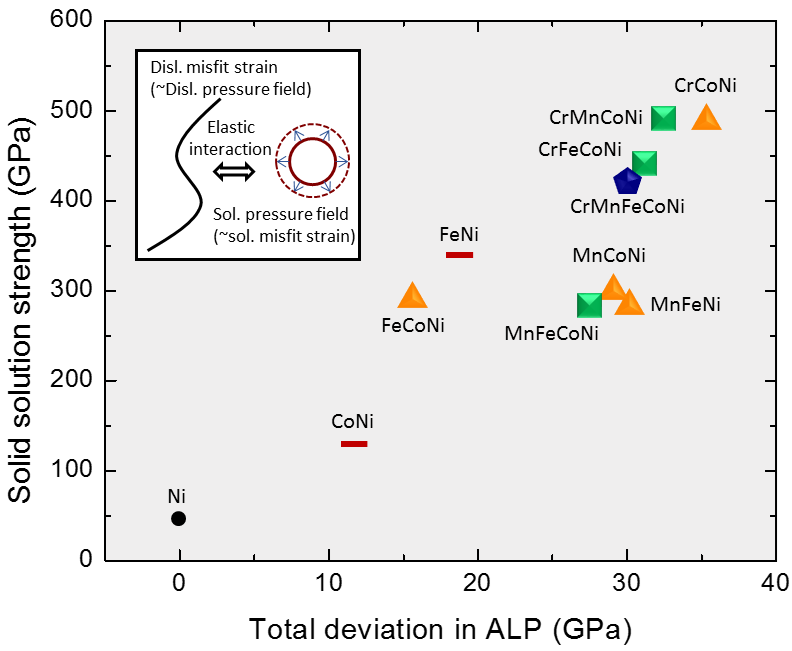


**Figure 6.2.** Total deviation of the atomic-level pressure in 3d CCAs versus solid-solution strengthening relation. Inset describes the elastic interaction between a dislocation and a solute atom, which is a dilatational source.

## 6.2. The origin of the atomic-level pressure in 3d CCAs

One striking feature of Figure 6.1 is that the atomic-level pressure does not correlate with the atomic volume. In terms of elasticity, the atomic-level pressure, i.e., the misfit volume, of a solute atom should follow the order of the size of the solute and matrix atoms (see Section 3.1). However, in current 3d CCAs, the average atomic-level pressures of each element follow only the order of the atomic number and not the atomic volume. Thus, the breakdown of the relationship between the atomic volume and atomic-level pressure implies other sources which are deeply related to the atomic number.

There are two main origins of atomic-level pressure reported in the literature: the atomic size difference and the charge transfer between a central atom and the surrounding atoms. Figure 6.3A shows the relationship between the charge transfer and atomic-level pressure in 3d CCAs. A linear trend between the atomic-level pressure and charge transfer is clearly observable. Furthermore, the total deviation of the charge transfer in each alloy shows a good linear correlation with the solid-solution strength. This means that the atomic-level pressure of the 3d CCA originates from the charge transfer rather than the difference in the atomic size, as schematically described in Figure 6.3C.

Two factors can be considered as the reasons why the charge transfer plays a major role in the atomic-level pressure of 3d CCAs. First, due to the complexity of the constituting elements, the local environment in CCAs can change to accommodate the atomic size effect by means of un-symmetric lattice distortion. This means that there is another way to relax the size misfit instead of changing the atomic sizes by means of pressure. This relaxation behavior has been reported in

glass and liquid states, [51, 115] and is one possible factor in CCAs. Second, the atomic sizes of Cr, Mn, Fe, Co, Ni are very similar at approximately 1.25Å. Thus, the pressure from the size misfit would be low [51].

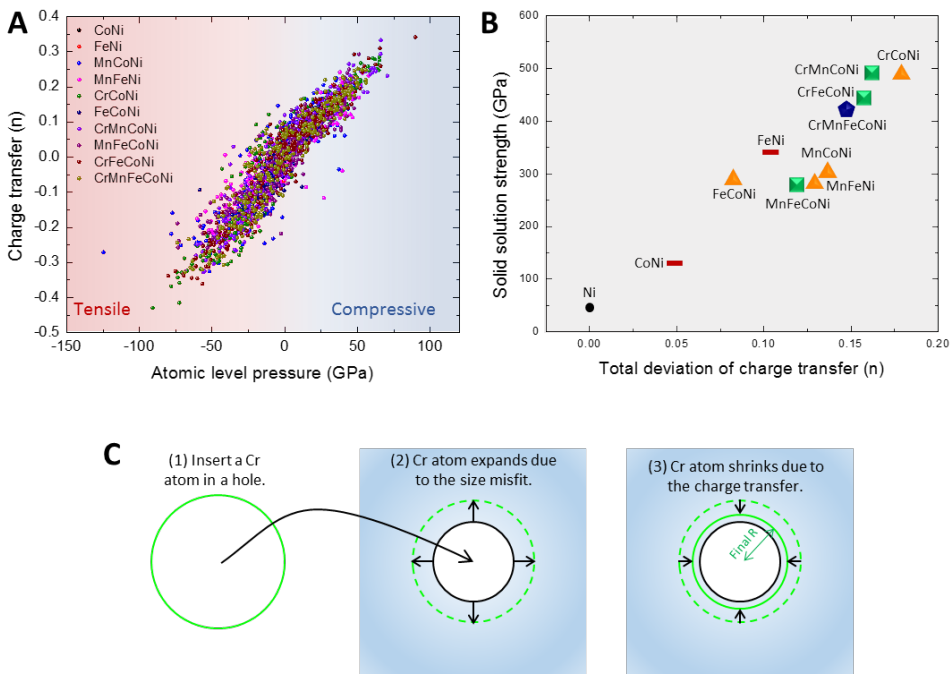


**Figure 6.3.** (A) Relationship between atomic-level pressure and the charge transfer of 3d CCAs. (B) Total deviation of the charge transfer in CCAs versus solid-solution strengthening relation. (C) Schematic diagram showing the generation of pressure from two sources, which are size misfit and charge transfer.

## 6.3. Descending degrees of complexity

As discussed in Section 5.3, CCAs have two different levels of complexity: the difference in the averaged properties of each element and the fluctuation of properties caused by the difference in local atomic configurations. Usually, the averaged properties of each element can be determined from experiments by measuring the compositional dependencies among the properties. However, the fluctuation of properties caused by the difference in local atomic configurations is difficult to measure or predict in experiments. Furthermore, the knowledge gained before the experimentation or calculations is merely information about the elements, such as the atomic size, electronegativity, and valence electron concentration, and not information about the individual atoms in the final alloys. Thus, from a practical point of view, a parameter of the total complexity of CCAs should be predictable according to the elemental average measurable properties.

Total deviation of the pressure can be further decomposed into the elemental and configurational deviations. In order to decompose the deviation of the pressure, we defined the elemental deviation $\sigma(\langle P\rangle_i)$ and configurational deviation $\sqrt{\langle\sigma^2(P)_i\rangle}$, where $\langle P\rangle_i$ is the average pressure of element i, and $\sigma(P)_i$ is the standard deviation of the pressure of element i. Statistically, the total deviation of the atomic-level pressure can be described in the Pythagorean form, as

$$\sigma^2(P) = \sigma^2(\langle P\rangle_i) + \langle\sigma^2(P)_i\rangle. \qquad \text{Eq. 6-3}$$

We devised a complexity diagram as a means by which to visualize the nature of the total (black), elemental (pink), and configurational (teal) deviation, as shown in Figure 6.4. The relationship in Eq. 6-3 is symbolized by a right-angle triangle. The

longest line intersects the center of the circle. The diameter, i.e., the size, of the circle implies the magnitude of the total deviation of pressure. The angle of the triangle represents the size ratio between each type of deviations.

As shown in Figure 6.4A, all triangles have a similar shape, with similar angles. The minimum angle is that of CoNi (22.7°), and the maximum angle is that of CrCoNi (33.7°). This implies that the proportions of the contribution of both types of deviation to the total deviation of the pressure are similar in the present CCAs. This also applies to the charge transfer (Figure 6.4B).

Figure 6.4C shows the probability distribution of the charge transfers in FeNi. When the center atom (Fe or Ni) is surrounded by the identical atoms, there is no pressure. On the other hand, when the ratio of unlike atoms among the surrounding atoms becomes large, the interaction between the center atom and the surrounding atoms becomes stronger, resulting in large positive or negative pressure. This implies that the stronger the mean interactions between the elements are, the greater the deviation becomes due to environmental fluctuations. For a binary alloy, assuming symmetricity and perfect linearity, the ratio between the elemental deviation and the configurational deviation becomes $\sqrt{6}$ (~2.45). Indeed, the ratios in all of the present CCAs were between 2.02 and 2.41.

In this section, we discussed how to lower the level of complexity in 3d CCAs for practical purposes. The linear relationships between the elemental and environmental deviations of pressure and charge transfer were revealed. This result makes it possible to predict a higher level of complexity (configurational deviation) with a lower level of complexity (elemental deviations), which can be identified experimentally.

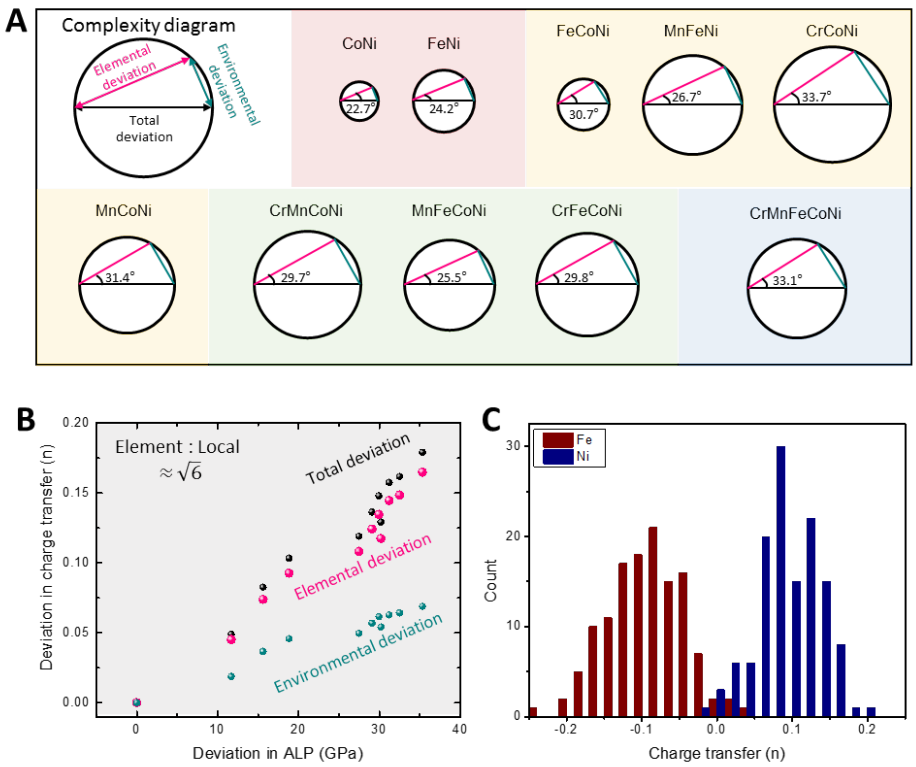


**Figure 6.4.** Descending the degrees of complexity (A) Complexity diagram showing elemental (pink), configurational (teal), and total (black) deviation of atomic-level pressure in equiatomic 3d CCAs. (B) Total (black), elemental (pink) and configurational (teal) deviation of charge transfer against the total deviation of atomic-level pressure in 3d CCAs. (C) Charge distribution in FeNi CCA. The distribution is nearly symmetric and linear.

## 6.4. Experimental measurement of the atomic-level pressure

### 6.4.1. Measurement of volume strain

In Chapter 5, the volume strain is calculated as the standard deviation of the effective atomic sizes of the constituting elements. However, as discussed in section 6.2, the volume strain inside the alloy results from the charge transfer and not from the elastic recovery of compressed/expanded atoms, as described in Eshelby's theory. Thus, the difference between the pure metallic radius and the effective atomic radius reflects the volume strain, as

$$\varepsilon_V = \gamma 3\varepsilon_r = \left(\frac{3(1-v)}{(1+v)}\right) 3\left(\frac{R_e}{R_0}\cdot K - 1\right), \qquad \text{Eq. 6-4}$$

where $\varepsilon_V$ is the volume strain, $\gamma$ is the Eshelby constant ($\frac{3(1-v)}{(1+v)}$) which converts the local volume change into the global volume change, $R_e$ is the effective atomic radius, $R_0$ is the metallic radius of a pure element, and $K$ is the correction factor of the lattice parameter. The metallic radius $R_0$ values of each of the elements are taken from simulated results assuming 12 coordinates (Table 6.1). The effective atomic radii measured by EXAFS in Chapter 5 are used here as the values of $R_e$. $K$ is introduced to consider the unknown additional effects on the lattice parameters, such as the temperature and the packing density, as

$$K \approx \frac{Ideal\ lattice\ parameter}{Real\ lattice\ parameter}, \qquad \text{Eq. 6-5}$$

where ideal refers to the average of the metallic radii and real is the average of the effective atomic radii.

Figure 6.5A shows the measured volume strain according to Eq. 6-4 for each

element in the 3d CCAs. The measured volume strains have a clear tendency in that a larger atomic number, i.e., a higher Fermi energy, leads to a larger the measured volume strain. The volume strains show good linear relationships with the simulated total deviation of the atomic-level pressure. This confirms our suggestion that the volume strain between the pure element and the effective atomic size in Eq.6-7 reflects the atomic-level pressure.

As discussed in Section 6.2, the atomic-level pressure in 3d CCAs originates from the charge transfer between a central atom and the surrounding environments. Given that the charge transfer is caused by the difference in the electronegativity between a center atom and the surrounding environments, the effective charge transfer of an element inside the alloy can be calculated by

$$C_{el} = -\frac{\sum_{i,j,k,l,m} \chi_{1st} \cdot i + \chi_{2nd} \cdot j + \chi_{3rd} \cdot k + \chi_{4th} \cdot l + \chi_{5th} \cdot m - 12 \cdot \chi}{n}, \quad \text{Eq. 6-6}$$

where $C_{el}$ is the charge transfer of the center element and $i, j, k, l,$ and $m$ connectively represent is the number of elements near the center atom ($i + j + k + l + m = 12$). In addition, $\chi_{ith}$ is the electronegativity of the $i$th element on Allen's scale, with the following ratios: Cr:1.65, Mn:1.75, Fe:1.8, Co:1.84, and Ni:1.88, and where $n$ is the total number of possible configuration. We used Allen's electronegativity rather than Pauling's because it reflects the Fermi energy better. Figure 6.5C shows the good agreement between the calculated charge transfer by Eq. 6-6 and the measured volume strain. Hence, the electronegativity difference is an effective tool by which to predict the volume strain and the resultant solid-solution strengthening effects.

**Table 6.1.** Simulated metallic radius of Cr, Mn, Fe, Co, Ni (12 coordinates) [116].

| Element | Cr | Mn | Fe | Co | Ni |
|---|---|---|---|---|---|
| $R_0$ (Å) | 1.28 | 1.27 | 1.26 | 1.25 | 1.24 |

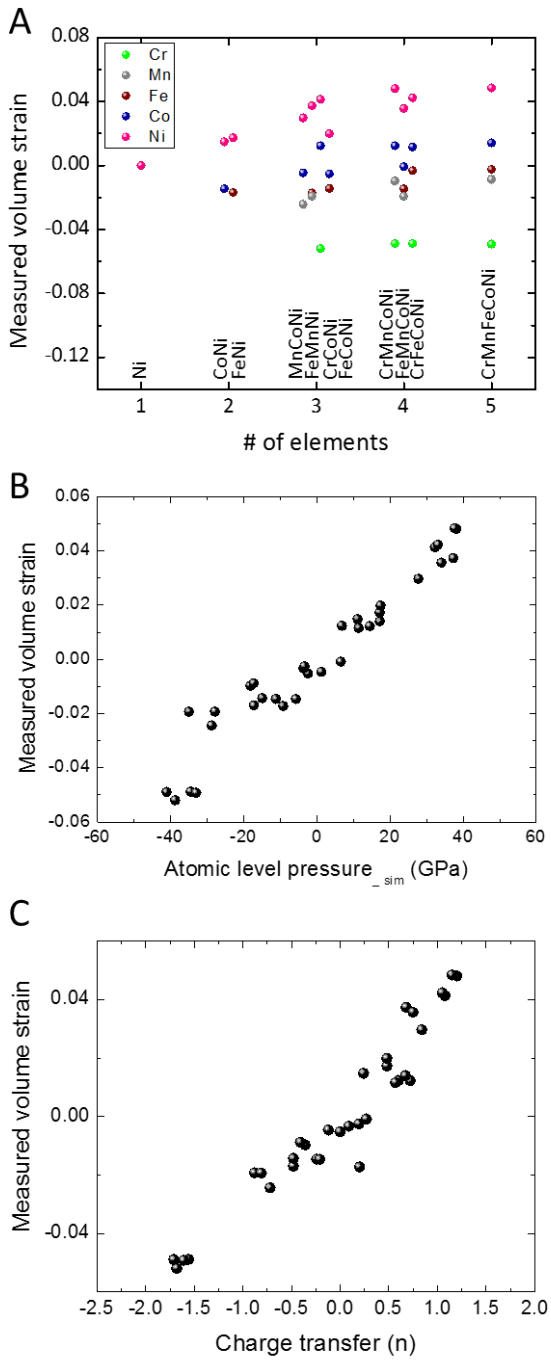


**Figure 6.5.** Experimentally measured volume strain of each element caused by the charge transfer. (A) Measured volume strain versus number of elements. (B) Measured volume strain versus simulated average atomic-level pressure. (C) Measured volume strain versus effective charge transfer.

## 6.4.2. Prediction of the solid-solution strength

In order to predict the solid-solution strengthening, we rewrite Eq. 3-6 using the volume strain concept, as follows:

$$\tau_{y0} = 0.051\alpha^{-\frac{1}{3}}\mu\left(\frac{1+\nu}{1-\nu}\right)^{\frac{4}{3}} f_1(w_c) \times \left(\frac{7}{6}\cdot\frac{{\varepsilon_V}^2}{2}\right)^{\frac{2}{3}}. \qquad \text{Eq. 6-7}$$

In Eq. 6-7, $7/6$ is multiplied to reflect the ratio between the total deviation and the elemental deviation. This prediction is made using the line tension parameter $\alpha$, which is 0.06125 [25]. We then calculated the theoretical solid-solution strengths and compared this outcome with the experimentally measured values (Table 5.1) as shown in Figure 6.6. Both values are plotted against the electronegativity difference to show the contribution of the charge transfer. The electronegativity difference between the constituting elements $\Delta\chi_{Allen}$ is

$$\Delta\chi_{Allen} = \sqrt{\sum_{i=1}^{n} c_i(\chi_i - \bar{\chi})^2}, \qquad \text{Eq. 6-8}$$

where $c_i$ is the composition of the ith element, $\chi_i$ is the electronegativity of the ith element, and $\bar{\chi}$ is the average electronegativity.

As shown in Figure 6.6, the predicted and experimentally measured solid-solution strengths are in good agreement with each other. Furthermore, both values are linearly proportional to $\Delta\chi_{Allen}$ with a high $R^2$ equal to 0.95. Thus, we conclude here that the solid-solution strength effect in 3d CCAs originates from the charge transfers between elements.

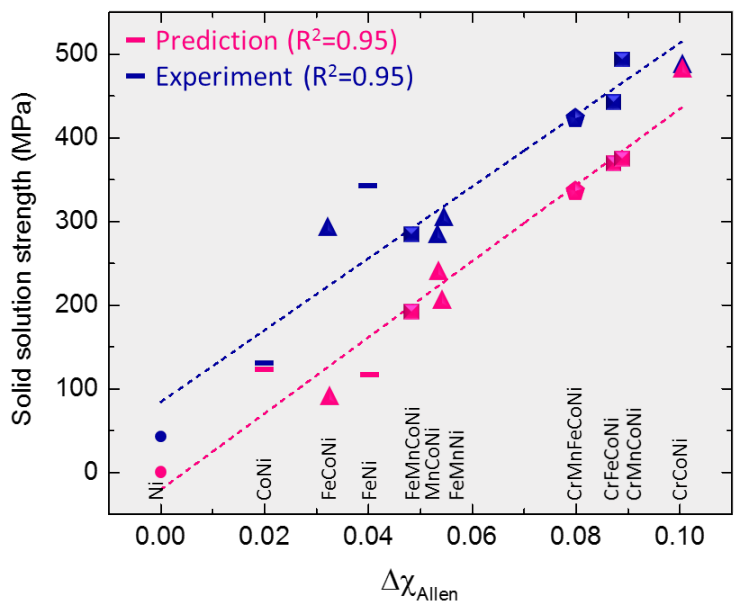


**Figure 6.6.** Theoretically predicted and experimentally measured solid-solution strength versus electronegativity difference. Both show good linear relationship with electronegativity difference with $R^2$ equal to 0.95.

## 6.5. Electronegativity diagram

The causes of the solid-solution strengthening effects in CCAs have been actively investigated by many researchers. However, in order to apply the theory to the actual design an alloy, one needs to devise a simple parameter which can be easily estimated with sufficient accuracy. The oldest and most widely used concept of solid-solution strengthening is the mixing entropy, $\Delta S_{mix}$ [1], which is described as

$$\Delta S_{mix} = -R \sum_{n} x_n ln x_n, \qquad \text{Eq. 6-9}$$

where $x_n$ is the composition of the nth component and $R$ is the gas constant. The concept is simple that chemical complexity of CCAs would introduce fluctuation of lattice potential energies, i.e. complexity of atomic-level pressure.

In order to compare the concepts, which are chemical complexity and complexity of atomic-level pressure, we calculated the electronegativity difference $\Delta\chi_{Allen}$, mixing entropy $\Delta S_{mix}$ and valence electron concentration (VEC) with all possible combinations of 3d transition metal elements (V, Cr, Mn, Fe, Co, Ni) as shown in Table 6.2. The number of possible combinations is 53129. Within these alloys, we utilized the alloys which have VEC values higher than 7.8, for the formation of the FCC phase. This resulted in 19055 combinations.

Figure 6.7 shows an electronegativity diagram of the relationship between electronegativity difference $\Delta\chi_{Allen}$ and the mixing enthalpy $\Delta S_{mix}$ for the solid-solution strengthening. All equi-atomic 3d CCAs consisting of Cr, Mn, Fe, Co, and Ni are marked. In addition, the positions of commercial alloy systems, in this case FeMn steel and FeNiCr steel, and the γ matrix of Ni-based superalloy are shown in

the diagram. There are several interesting points in this diagram.

1. CrCoNi is located at a higher position than CrMnFeCoNi despite its lower mixing entropy. This is consistent with a previous observation that CrCoNi has a higher yield strength and a higher solid-solution strength than CrMnFeCoNi.
2. FeMn, a type of steel used commercially, is located at a very low position. This implies a good potential to develop a new 3d CCA with very strong mechanical properties if we optimize the plasticity mechanism of CCA given the high solid-solution strength.
3. The common view of the effects of the mixing entropy on the solid-solution strengthening holds with regard to binary alloys. However, the mixing entropy is not strongly correlated with the solid-solution strengthening. Furthermore, there is a region in which the mixing entropy should be decreased to obtain greater solid-solution strengthening effects.

In order to verify the benefits implied in the diagram, we developed binary VNi as a model system. The eutectoid point ($V_{36.8}Ni_{63.2}$) is chosen for higher stability of the single FCC phase (Figure 6.8A). The post-processing condition is described in Figure 6.8B. We initially cold-rolled the sample to destroy the eutectoid structure established during the solidification process. The cold-rolled sample was then wrapped in Ta foil and homogenized at 1075°C for 45 hours inside a quartz tube under a high vacuum condition. The homogenized samples are cold-rolled and then undergo recrystallization annealing at 920°C for 3 min. Figure 6.8C-F shows that the fabricated VNi alloy has a single-phase microstructure.

Figure 6.9 shows the representative tensile stress-strain curve of the developed

VNi CCA deformed at a strain rate of $1 \times 10^{-3}$ $s^{-1}$ at room temperature. The inset shows the average grain size of VNi CCA, i.e., 8.3 μm. To emphasize the substantial improvement in the properties, the curves for two other CCAs (CrCoNi [117] and CrMnFeCoNi [3]) are also presented. The yield strength of the VNi CCA is approximately 750 MPa and the ultimate tensile strength (UTS) is close to 1200 MPa. Thus, the VNi CCA notably outperforms previous CCAs with similar grain sizes. This again confirms our conceptualization that an alloy with a large electronegativity difference has higher complex local environments even with low mixing entropy.

**Table 6.2.** Examples of the combinations of 3d elements (V, Cr, Mn, Fe, Co, Ni).

| | V | Cr | Mn | Fe | Co | Ni | $\Delta\chi_{Allen}$ | $\Delta S_{mix}$ | VEC |
|---|---|---|---|---|---|---|---|---|---|
| 1 | 50 | 0 | 0 | 0 | 0 | 50 | 0.175 | 5.763172 | 7.5 |
| 2 | 45 | 0 | 0 | 0 | 0 | 55 | 0.174123 | 5.72153 | 7.75 |
| 3 | 55 | 0 | 0 | 0 | 0 | 45 | 0.174123 | 5.72153 | 7.25 |
| 4 | 50 | 0 | 0 | 0 | 5 | 45 | 0.173208 | 7.114623 | 7.45 |
| 5 | 45 | 0 | 0 | 0 | 5 | 50 | 0.172525 | 7.114623 | 7.7 |
| 6 | 55 | 0 | 0 | 0 | 5 | 40 | 0.172118 | 7.026694 | 7.2 |
| 7 | 50 | 0 | 0 | 5 | 0 | 45 | 0.17184 | 7.114623 | 7.4 |
| 8 | 40 | 0 | 0 | 0 | 0 | 60 | 0.171464 | 5.595756 | 8 |
| 9 | 60 | 0 | 0 | 0 | 0 | 40 | 0.171464 | 5.595756 | 7 |

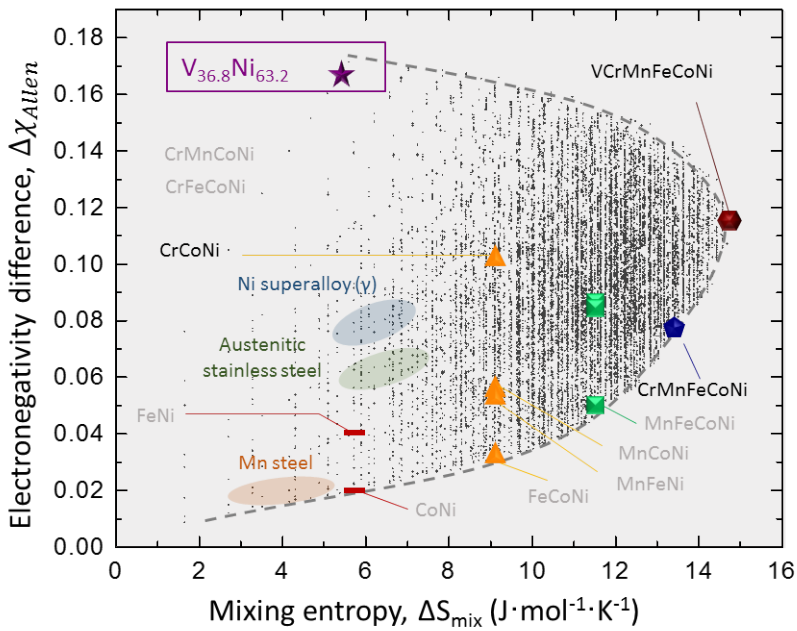


**Figure 6.7.** Electronegativity diagram showing the relationship between electronegativity difference $\Delta\chi_{Allen}$ and the mixing enthalpy $\Delta S_{mix}$ for the solid-solution strengthening. All possible combinations of 3d transition metal elements (V, Cr, Mn, Fe, Co, Ni) with average VEC>7.8 are included. The position of the commercial alloy systems such as FeMn steel, FeNiCr steel, and γ matrix of Ni-based superalloy are shown in the diagram. $V_{36.8}Ni_{63.2}$, a model system of this research, is indicated in purple.

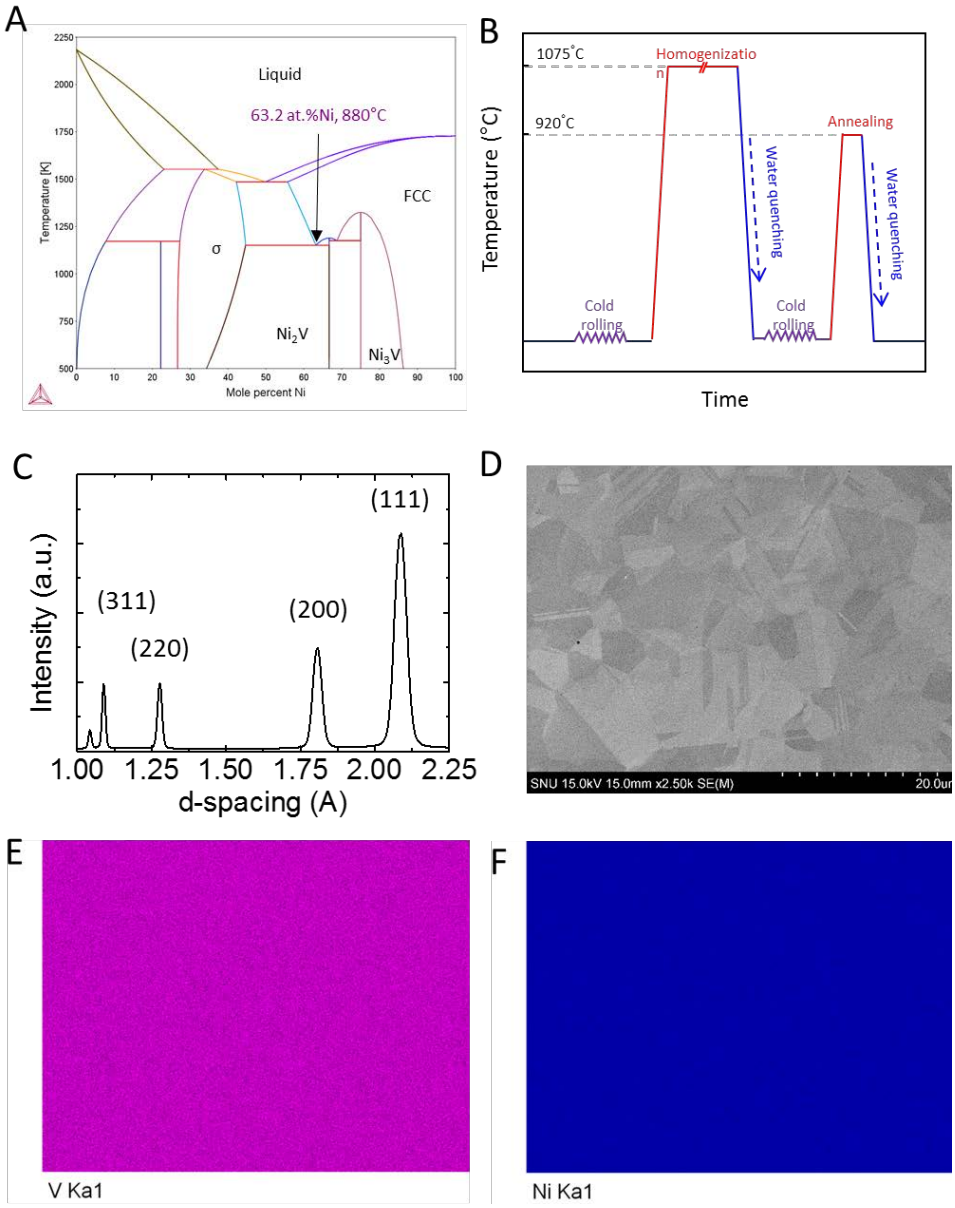


**Figure 6.8.** (A) V-Ni binary phase diagram. (B) Processing condition of current $V_{36.8}Ni_{63.2}$ CCA, (C) High energy XRD pattern showing the single phase FCC, (D) SEM images showing the microstructure, (E-F) EDS results show the homogeneous distribution of elements.

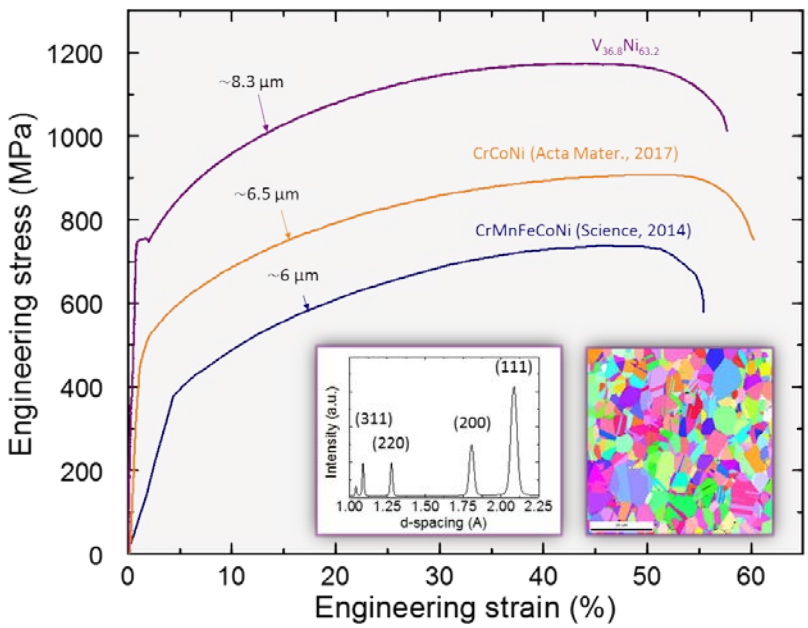


**Figure 6.9.** Tensile behavior of $V_{36.8}Ni_{63.2}$ alloy compared to various single-phase CCAs. Grain sizes are shown in micrometers. The tensile stress-strain curves of single-phase equi-atomic CrCoNi [51] and CrMnFeCoNi [3] are also shown here. The inset shows that $V_{36.8}Ni_{63.2}$ has single FCC phase (high energy XRD pattern) with the average grain size of 8.3µm (IPF map).

## 6.6. Summary

In this chapter, an atomic-level pressure concept is applied to describe the atomic-level complexity of 3d CCAs and the resultant solid-solution strengthening effect. First, we showed that the deviation of atomic-level pressure is closely related to the solid-solution strengthening through the DFT calculation. Second, we then found that the atomic-level pressure and the resultant solid-solution strengthening effects originate from the charge transfer induced by the electronegativity difference of constituent elements. Third, through a statistical approach, we found that both values of 'deviation of average elemental atomic-level pressure' and 'deviation of atomic-level pressure due to the variance in local atomic configurations' are linearly proportional to each other. This makes it possible to estimate a higher degree complexity (configurational deviations) using a lower degree complexity (elemental deviations), which can be identified experimentally. Based on these criteria, an electronegativity-mixing entropy diagram was constructed to clarify the solid-solution strengthening effects in 3d CCAs. The shape of the area of 3d CCAs indicates that there is no strong correlation between the chemical complexity and the deviation (i.e. complexity) of atomic-level pressure in 3d CCAs. The concept of complexity of atomic-level complexity can be applied not only to the solid-solution strengthening, but also to the general properties which are affected by fluctuations of local potential energies, such as sluggish diffusion, transport properties, and lattice distortion, among others. Thus, we concluded that the complexity of atomic-level pressure and the related properties should be distinguished from the chemical complexity in CCAs.

# Chapter 7. Design of CCAs to overcome the strength-ductility trade-off

"The 'cocktail' effect reminds us to remain open to non-linear, unexpected results that can come from unusual combinations of elements and microstructures in the vast composition space of MPEAs." – D.B. Miracle [14]

In Chapter 6, it was shown that the dominant factor for the solid-solution strengthening in 3d CCAs is not the number of elements (chemical complexity) but the deviation (i.e. complexity) of the atomic-level pressures from the charge transfers between adjacent atoms. One may debate that the chemical complexity is no longer important with regard to CCAs, as the complexity of atomic-level pressure is related to lattice distortion and sluggish diffusion, two of the four 'core effects' of CCAs. However, this does not reduce the importance of the chemical complexity in CCAs. The cocktail effect, a phrase describing synergistic response from the chemical complexity, can be found whenever a new CCA is developed.

Plastic deformation mechanisms in CCAs are of particular interest in that they show the synergistic effects of the degree of chemical complexity. Several CCAs, such as CrMnFeCoNi, [3, 118] CrCoNi [4, 119], and FeMnCoCr [120], have been developed, all showing exceptional damage tolerance given the synergy of multiple deformation mechanisms (Table 7.1.), rarely achieved in conventional alloys. However, because it is difficult to control the solid-solution strengthening of these alloy systems, the effects of chemical complexity have not been investigated separately.

In this chapter, a series of new 3d CCAs with twin-induced plasticity (TWIP)

and transformation-induced plasticity (TRIP) is developed by changing the compositions from the CrMnFeCoNi Cantor alloy. It was possible to consider all conditions comprehensively, which are as follows: 1) solid-solution strengthening, 2) stacking fault energy, and 3) phase stability, due to the compositional diversity (i.e. chemical complexity) in this system. This work shows that it is possible to overcome the strength-ductility trade-off [121, 122] in CCAs considering both the complexity of atomic-level pressure (deviation of atomic-level pressure) and the chemical complexity (degree of compositional diversity).

**Table 7.1.** Characteristics of mechanical properties of CCAs.

| | Special feature | Deformation mechanisms |
|---|---|---|
| CrMnFeCoNi [3] | High fracture toughness at both of room and cryogenic temperatures | ▪ The easy motion of Shockley partials<br>▪ Formation of stacking-fault parallelepipeds<br>▪ Arrest of undissociated dislocations at planar slip band<br>▪ Twinned, nanoscale bridges at the crack |
| CrCoNi [4] | Highest combinations of strength and toughness | ▪ Three-dimensional hierarchical twin network |
| FeMnCoCr [54] | Overcoming strength-ductility trade-off | ▪ Interface hardening due to a dual-phase microstructure<br>▪ Transformation induced plasticity<br>▪ Solid-solution strengthening |

## 7.1. Alloy design

### 7.1.1. Stacking fault energy

The plasticity mechanisms of face-centered cubic (FCC) alloys mainly depend on the stacking fault energy (SFE) [123-127]. The SFE dictates the magnitude of dissociation of dislocations into Shockley partials and consequently the secondary deformation mechanisms, including mechanical twinning and/or martensitic transformation. With a high SFE, only dislocation gliding occurs. On the other hand, a low SFE results in a wide dissociation of dislocations, hindering cross-slip and dislocation climbing, and thus favoring secondary deformation mechanisms. In the case of Manganese steel, mechanical twinning forms for intermediate values of the SFE, and α′ or ε-martensite formation becomes the favored deformation mechanism for the lowest SFE.

Olson and Cohen proposed the following equation for the stacking fault energy as, [128]

$$\Gamma = 2\rho\Delta G^{\gamma\rightarrow\varepsilon} + 2\sigma^{\gamma/\varepsilon}, \qquad \text{Eq. 7-1}$$

where $\Gamma$ is the SFE, $\rho$ is the molar surface density along the (1 1 1) planes, $\Delta G^{\gamma\rightarrow\varepsilon}$ is the molar Gibbs energy of the phase transformation from the $\gamma$-austenite to $\varepsilon$-martensite, and $\sigma^{\gamma/\varepsilon}$ is the interfacial energy of boundary between $\gamma$ and $\varepsilon$ phases. The main assumption of the model is that the intrinsic and the extrinsic stacking fault in an FCC crystal structure is a two-plane thin layer of a hexagonal close-packed (HCP) phase. Thus, the tendency of SFEs given compositional changes can be predicted using $\Delta G^{\gamma\rightarrow\varepsilon}$ [129-131].

Figure 7.2 shows the change in $\Delta G^{\gamma\rightarrow\varepsilon}$ with the Cr, Mn, Fe, Co, and Ni

contents in CrMnFeCoNi alloys. The $\Delta G^{\gamma\rightarrow\varepsilon}$ values were calculated using Thermocalc software (TCFE8 database). In order to determine the contribution of each element, one composition is changed and the compositions of the other elements were given a fixed ratio, as shown in Table 7.1.

As clearly indicated in Figure 7.2, Cr, Fe, and Co decrease $\Delta G^{\gamma\rightarrow\varepsilon}$, and thus the SFE. On the other hand, Mn and Ni increase $\Delta G^{\gamma\rightarrow\varepsilon}$. The relationship between $\Delta G^{\gamma\rightarrow\varepsilon}$ and each content level is expressed by the following equation:

$$\Delta G_{hcp-fcc} = -100X_{Cr} + 73X_{Mn} - 22X_{Fe} - 42X_{Co} + 77X_{Ni} + 2186 \quad \text{Eq. 7-2}$$

Thus, the compositional effects on the SFEs of CrMnFeCoNi alloys for different plastic deformation mechanisms can be predicted using Eq. 7-2.

**Table 7.2.** Compositional dependence of $\Delta G^{\gamma \to \varepsilon}$ in CrMnFeCoNi CCA calculated by Thermocalc (database:TCFE8). The examples are the dependence on Cr composition.

| at.% composition | | | | | $\Delta G^{\gamma \to \varepsilon}$ |
|---|---|---|---|---|---|
| Cr | Mn | Fe | Co | Ni | |
| 5 | 23.75 | 23.75 | 23.75 | 23.75 | 3732 |
| 10 | 22.5 | 22.5 | 22.5 | 22.5 | 3175 |
| 15 | 21.25 | 21.25 | 21.25 | 21.25 | 2555 |
| 20 | 20 | 20 | 20 | 20 | 1928 |
| 25 | 18.75 | 18.75 | 18.75 | 18.75 | 1302 |
| 30 | 17.5 | 17.5 | 17.5 | 17.5 | 686 |
| 35 | 16.25 | 16.25 | 16.25 | 16.25 | -87 |
| 40 | 15 | 15 | 15 | 15 | -487 |

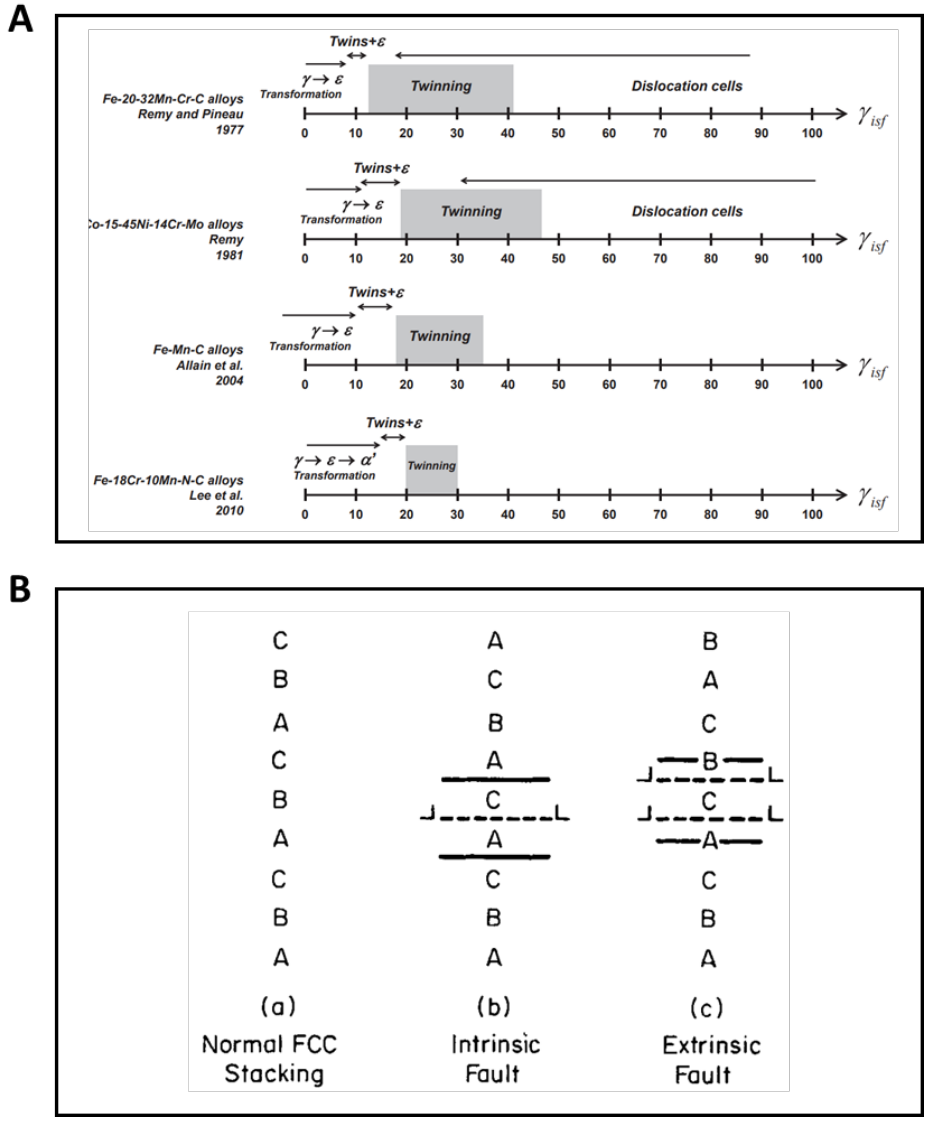


**Figure 7.1.** (A) Ranges of the intrinsic stacking fault energy for phase transformation, deformation twinning, and dislocation glide in FCC Fe alloys reported in the literature. (B) Stacking sequence of close packed planes in FCC stacking fault structures. Reprinted from [127]-(A), [128]-(B) with permission through "Copyright Clearance Center".

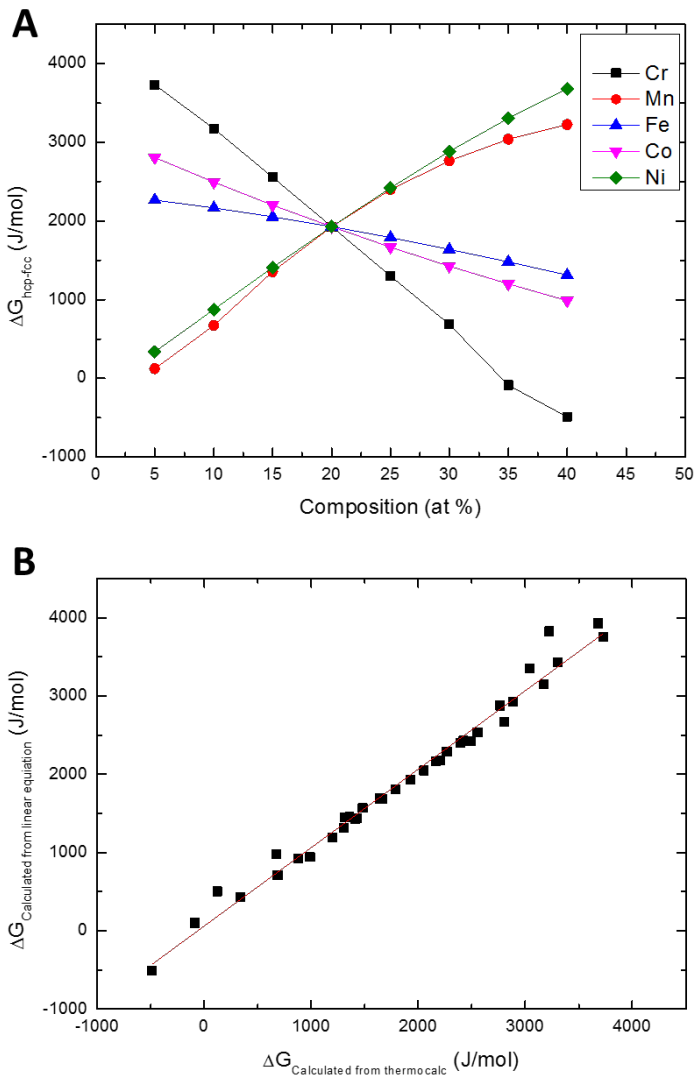


**Figure 7.2.** (A) A graph showing a compositional dependence of $\Delta G^{\gamma \to \varepsilon}$ in CrMnFeCoNi CCAs, calculated by Thermocalc (Database:TCFE8). Contributions of each elements are obtained by linear fitting of each lines as described in Eq. 7-2. (B) The recalculated $\Delta G^{\gamma \to \varepsilon}$ from Eq. 7-2 matches well with the original $\Delta G^{\gamma \to \varepsilon}$ in (A).

### 7.1.2. Solid-solution strengthening

In Chapter 6, the electronegativity difference $\Delta\chi$ is proposed as a dominant parameter of the solid-solution strengthening of 3d CCAs instead of the volume misfit of the constituting elements. However, in addition to the electronegativity difference $\Delta\chi$, the stacking fault energy $\gamma_{SF}$ should be considered because the dissociation of a dislocation into two Shockley partials affects the solid-solution strengthening by changing the geometrical distance between the dislocations and the solutes [25], as shown in Figure 7.3A. Varvenne [25] computed the dimensionless pressure field $f(x_i,y_j)$ as a function of the partial spacing d and the Burgers vector b. Interestingly, when d/b >10, it indicates that the core properties of dislocations do not affect the minimized core coefficients for the solid-solution strengthening as shown in Figure 7.3B. Because d/b can be described by the following equation [92],

$$\frac{d}{b} = \frac{\mu b}{\gamma_{SF}} \frac{(2+\nu)}{24\pi(1-\nu)}, \qquad \text{Eq. 7-3}$$

for general FCC alloys with $\mu$ ~ 100 GPa, $b$ ~ 2.5Å, and $\nu$ ~ 0.3, d/b is larger than 10 when the SFE is less than 100 mJ/m$^2$.

The separation of Shockley partials in CrMnFeCoNi was determined by Okamoto [132] and was reported to be 3.5-4.5 nm near the screw orientation to 5-8nm near the edge, which is sufficiently longer than 10b. Furthermore, the resultant SFE of the CrMnFeCoNi alloy was reported to be 30$\pm$5 mJ/m$^2$. Thus, we conclude that the SFE does not have to be considered with regard to the solid-solution strength for the new CCAs.

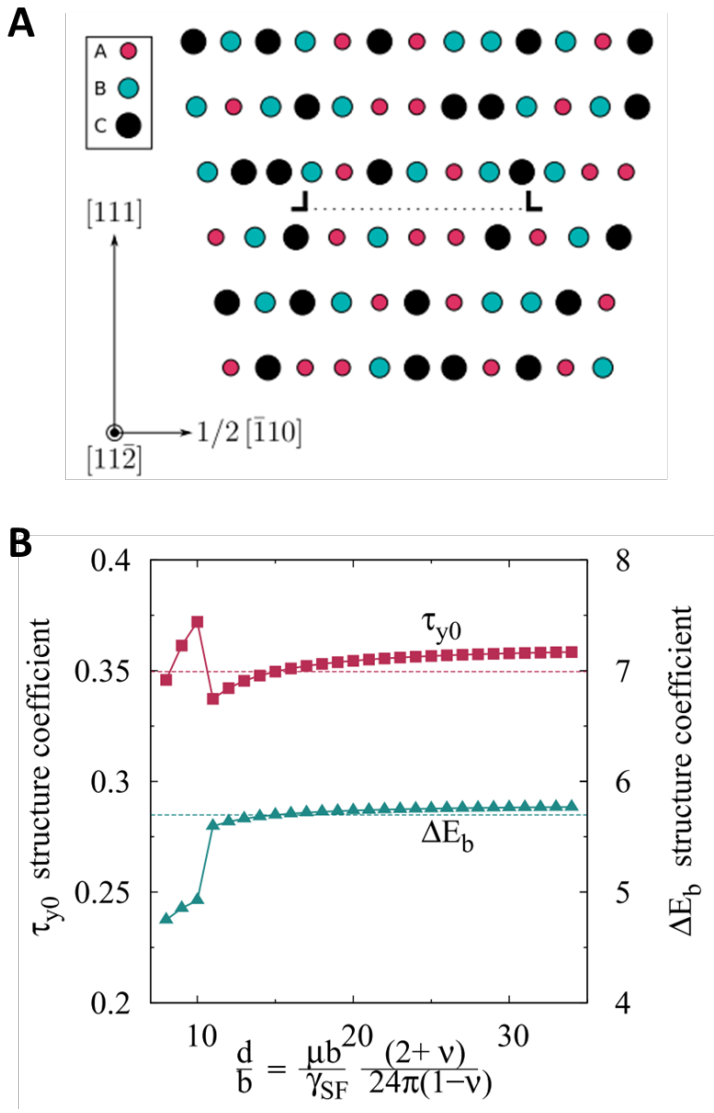


**Figure 7.3.** Relationship between dislocation core structure and solid-solution strengthening effect. (A) Schematic illustration showing the interaction between dissociated dislocation and solutes. Fully random 3-component CCA containing a dissociated edge dislocation. (B) Dependence of strength and energy barrier on dislocation dissociation distance d. Reprinted from [25] with permission through "Copyright Clearance Center".

### 7.1.3. Single-phase formation

In order to design single-phase CCAs, the tendency toward single-phase formation in CCAs is also considered. Although the high configurational entropy of CCAs is known to contribute to the stabilization of high-entropy phases during non-equilibrium solidification, the phase stability of CCAs is complicated. Depending on the post-processing conditions, the compositional complexity can lead to the formation of unexpected phases when diffusion is activated. It has been shown that atomic pairs with positive or negative mixing enthalpies in a complex compositional environment increase the probability of elemental combinations favoring intermetallic compounds or decompositions.

The ratio of $T^{2nd}/T^{s}$, i.e., the ratio between solidus temperature ($T^{s}$) and the 2nd phase formation temperature ($T^{2nd}$) can serve as a parameter of the phase stability. When $T^{2nd}$ is sufficiently low, the diffusivity cannot result in phase decomposition on an experimental time scale. Figure 7.4 shows the change in $T^{2nd}/T^{s}$ with the Cr, Mn, Fe, Co, and Ni contents in CrMnFeCoNi CCAs. The $T^{2nd}/T^{s}$ values were calculated using Thermocalc software (TCFE8 database). In order to find the contribution of each element, one composition is changed and the compositions of the other elements were given a fixed ratio, as shown in Table 7.2.

As clearly indicated in Figure 7.4, Fe, Co, and Ni decrease the value of $T^{2nd}/T^{s}$. On the other hand, Cr and Mn increase $T^{2nd}/T^{s}$. This outcome is consistent with previous results which showed that $Cr_{26}Mn_{20}Fe_{20}Co_{20}Ni_{14}$ has a multi-phase microstructure as the annealing temperature lower than 1000 °C [133]. Therefore, Fe, Co, and Ni have beneficial effects and Cr and Mn have detrimental effects with regard to the formation of single phase.

**Table 7.3.** Compositional dependence of $T^{2nd}/T^{s}$ in CrMnFeCoNi CCA calculated by Thermocalc (database:TCFE8). The examples are the dependence on Cr composition.

| Composition | | | | | $T^{2nd}$ | $T^{s}$ | $T^{2nd}/T^{s}$ | 2nd phase |
|---|---|---|---|---|---|---|---|---|
| Cr | Mn | Fe | Co | Ni | | | | |
| 10 | 22.5 | 22.5 | 22.5 | 22.5 | 780 | 1554 | 0.501 | bcc |
| 12 | 22 | 22 | 22 | 22 | 772 | 1555 | 0.496 | bcc |
| 14 | 21.5 | 21.5 | 21.5 | 21.5 | 770 | 1555 | 0.495 | bcc |
| 16 | 21 | 21 | 21 | 21 | 820 | 1555 | 0.527 | bcc |
| 18 | 20.5 | 20.5 | 20.5 | 20.5 | 870 | 1554 | 0.560 | bcc |
| 20 | 20 | 20 | 20 | 20 | 930 | 1554 | 0.598 | bcc |
| 22 | 19.5 | 19.5 | 19.5 | 19.5 | 990 | 1553 | 0.637 | bcc |
| 24 | 19 | 19 | 19 | 19 | 1060 | 1552 | 0.682 | bcc |
| 26 | 18.5 | 18.5 | 18.5 | 18.5 | 1154 | 1551 | 0.744 | bcc |
| 28 | 18 | 18 | 18 | 18 | 1280 | 1550 | 0.826 | bcc |
| 30 | 17.5 | 17.5 | 17.5 | 17.5 | 1560 | 1560 | 1 | bcc |

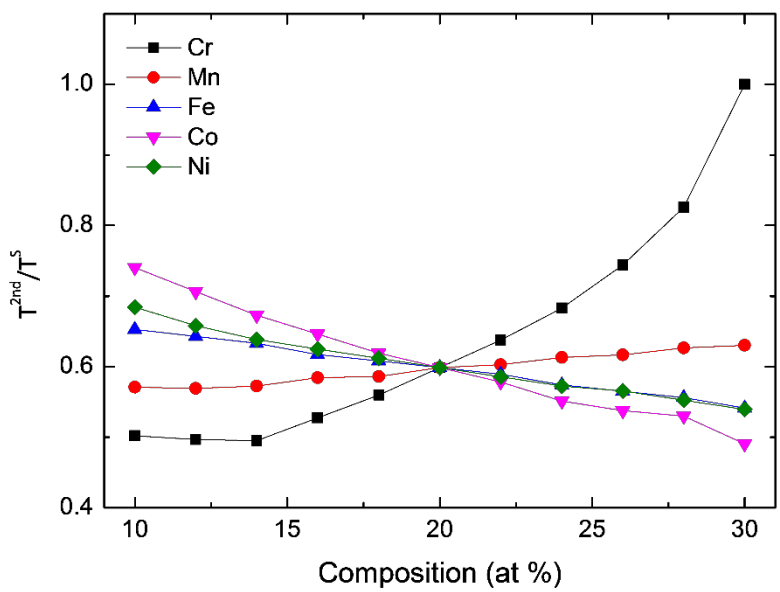


**Figure 7.4.** A graph showing a compositional dependence of $T^{2nd}/T^{s}$ in CrMnFeCoNi CCAs, calculated by Thermocalc (Database:TCFE8).

### 7.1.4. Comprehensive design

Considering Sections 7.1.1 through 7.1.3 together, we established three guidelines for the design of 3d CCAs.

(1) The stacking fault energy decreases with Cr, Fe, and Co and increases with Mn and Ni.
(2) The solid-solution strength increases when the $\Delta\chi$ increases.
(3) The phase stability increases with Fe, Co, and Ni and decreases with Cr and Mn.

Considering the above guidelines, several CCAs were designed, as presented in Table 7.4. The $\Delta G^{\gamma\rightarrow\varepsilon}$ decreases for lower SFEs, and the $\Delta\chi_{Allen}$ values are similar to each other for the maintenance of the solid-solution strength.

**Table 7.4.** Composition of designed CCAs and the corresponding $\Delta G^{\gamma \to \varepsilon}$ and $\Delta\chi_{Allen.}$

| | Composition | $\Delta G_{(hcp\text{-}fcc)}$ (J) | $\Delta\chi_{Allen}$ |
|---|---|---|---|
| 1 | $Cr_{20}Mn_{20}Fe_{20}Co_{20}Ni_{20}$ (CCA20) | 1927.8 | 4.46 |
| 2 | $Cr_{20}Mn_{18}Fe_{22}Co_{22}Ni_{18}$ | 1494.4 | 4.41 |
| 3 | $Cr_{20}Mn_{16}Fe_{24}Co_{24}Ni_{16}$ | 1108.4 | 4.36 |
| 4 | $Cr_{20}Mn_{14}Fe_{26}Co_{26}Ni_{14}$ (CCA14) | 771.0 | 4.31 |
| 5 | $Cr_{20}Mn_{12}Fe_{28}Co_{28}Ni_{12}$ | 482.9 | 4.26 |
| 6 | $Cr_{20}Mn_{10}Fe_{30}Co_{30}Ni_{10}$ (CCA10) | 245.3 | 4.21 |
| 7 | $Cr_{20}Mn_{8}Fe_{32}Co_{32}Ni_{8}$ | 59.4 | 4.21 |

## 7.2. Microstructure prior to the deformation

The designed CCAs were cast in a vacuum induction furnace using pure metals (99.8 wt.%). The as-cast ingot (20×50×150 $mm^3$) was hot-rolled at 900 °C to a thickness reduction of 50% in order to destroy the casting structure. Subsequently, the alloy sheets of 10 mm thickness were homogenized at 1200 °C for 3h in an Ar atmosphere, followed by water-quenching. The homogenized alloys were cold-rolled to a thickness reduction of close to 85% (the thickness changed from 10 to 1.5 mm) and subsequently annealed at a furnace temperature of 900°C in an Ar atmosphere for 3 min followed by water-quenching. The high temperature and short annealing time were used to prevent the effects of the SFE on the grain growth. The final microstructures are measured using multiple techniques.

Figure 7.5 shows the microstructures of the designed CCAs as measured by electron backscatter diffraction (EBSD). Figure 7.5A-C give the phase maps. These data reveal that the CCAs have a single-phase microstructure, specifically FCC γ. The grain sizes of each of the CCAs as calculated from the IPF maps shown in Figure 7.5D-F are 3.8 μm (CCA20), 3.6 μm (CCA14), and 4.3 μm (CCA10), similar to each other. The geometrically necessary dislocation density $\rho_{gnd}$ can be calculated from the Kernal average misorientation map using the equation below [134, 135]

$$\rho_{gnd} = \frac{2\theta}{ub}, \qquad \text{Eq. 7-4}$$

where $\theta$ is the average misorientation; $u$ is the unit length of the EBSD scan (step size), which is 50 nm in this thesis; and $b$ is the magnitude of the Burgers vector. The resultant GND densities are $2.6\times10^{13}$ /$m^2$ in CCA20, $2.8\times10^{13}$ /$m^2$ in CCA14, and $4.0\times10^{13}$ /$m^2$ in CCA10, which are negligibly small.

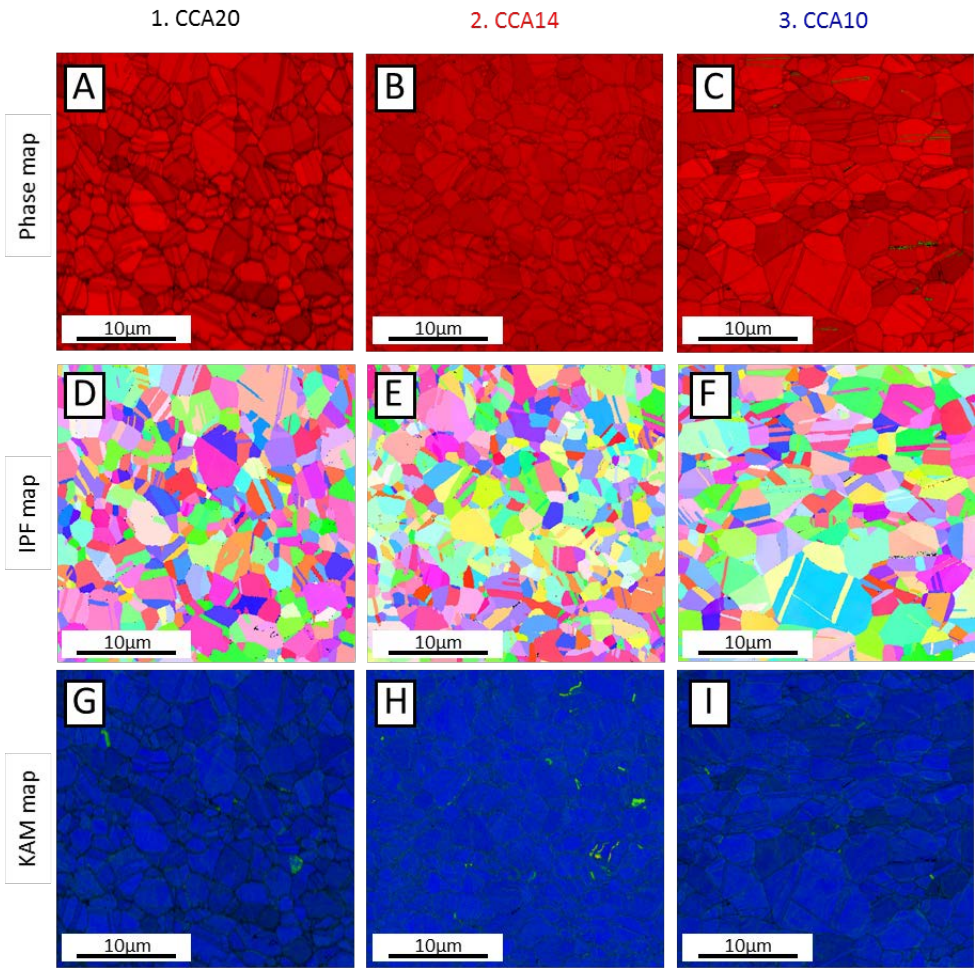


**Figure 7.5.** EBSD maps showing the information of undeformed CCAs. (A-C) Phase maps showing the single phase nature in the present CCAs. (D-E) IPF maps reveal that present CCAs have similar grain sizes. (G-I) KAM maps show that initial dislocation densities are small enough be neglected.

## 7.3. Mechanical properties

Figure 7.6 shows the representative tensile stress-strain curves of the designed CCAs deformed at a strain rate of $1 \times 10^{-3}$ $s^{-1}$ at room temperature. The yield strength ($\sigma_y$) of all developed CCAs with various SFEs are similar to each other (~400MPa). The ultimate tensile strength (UTS) and uniform elongation values of CCA14 and CCA10 increase despite the yield strength being similar to that of CCA20. This is evidence that the strength-ductility trade-off is overcome.

The yield stress is a combination of the frictional stress ($\sigma_{fr}$), or the intrinsic lattice resistance to dislocation motion, plus the various incremental strengthening mechanisms, such as those due to the initial dislocation density ($\Delta\sigma_{\rho i}$), solid-solution strengthening ($\Delta\sigma_{ss}$), precipitation hardening ($\Delta\sigma_{ppt}$) and grain boundary strengthening ($\Delta\sigma_{gb}$). A general expression for the yield strength can therefore be written as follows:

$$\sigma_y = \sigma_{fr} + \Delta\sigma_{\rho i} + \Delta\sigma_{ss} + \Delta\sigma_{ppt} + \Delta\sigma_{gb}. \quad \text{Eq. 7-5}$$

First, due to the low Peierls stress in FCC alloys, $\sigma_{fr}$ can be ignored. Because no precipitates are present in the CCAs as shown in Figure 7.5A-C, $\Delta\sigma_{ppt}$ can be ignored as well. All CCAs would have similar values of $\Delta\sigma_{gb}$ because they have similar grain sizes, as shown in Figure 7.5D-F. $\Delta\sigma_{\rho i}$ can also be ignored owing to the low initial dislocation densities. In consequence, the $\sigma_y$ values of present CCAs depend only on $\Delta\sigma_{ss}$, which are virtually identical, as discussed in Section 7.1.

Figure 7.6A presents the corresponding strain-hardening response with respect to the true strain. The $\sigma_u$ and $\varepsilon_u$ values of all of the developed CCAs

increase as the SFE decreases from 690 MPa and 43% for CCA20 to 850 MPa and 62% for CCA10. With regard to plastic deformation, we observe that the newly developed CCA14 and CCA10 have significantly higher values of $\sigma_u$ (740 MPa at CCA14 and 850 MPa at CCA10) compared to that of CCA20 (690 MPa), although they also have similar yield strengths. We also observe that the $\varepsilon_u$ values of CCA14 (55%) and CCA10 (62%) are much higher than that of CCA20 (43%).

Figure 7.6B reveals the corresponding strain-hardening behavior with respect to the true strain in the CCAs. CCA10 shows significantly higher strain-hardening rates over the entire plastic deformation region compared to those of CCA20 and CCA14. Although CCA14 shows lower strain-hardening rates in the initial deformation states, it shows higher strain-hardening rates again in the medium and later deformation stages, with true strain values exceeding 7%. This suggests that the deformation mechanisms triggered in CCA14 and CCA10 are more capable of inducing strain hardening, hence leading to higher UTS levels and more uniform elongation.

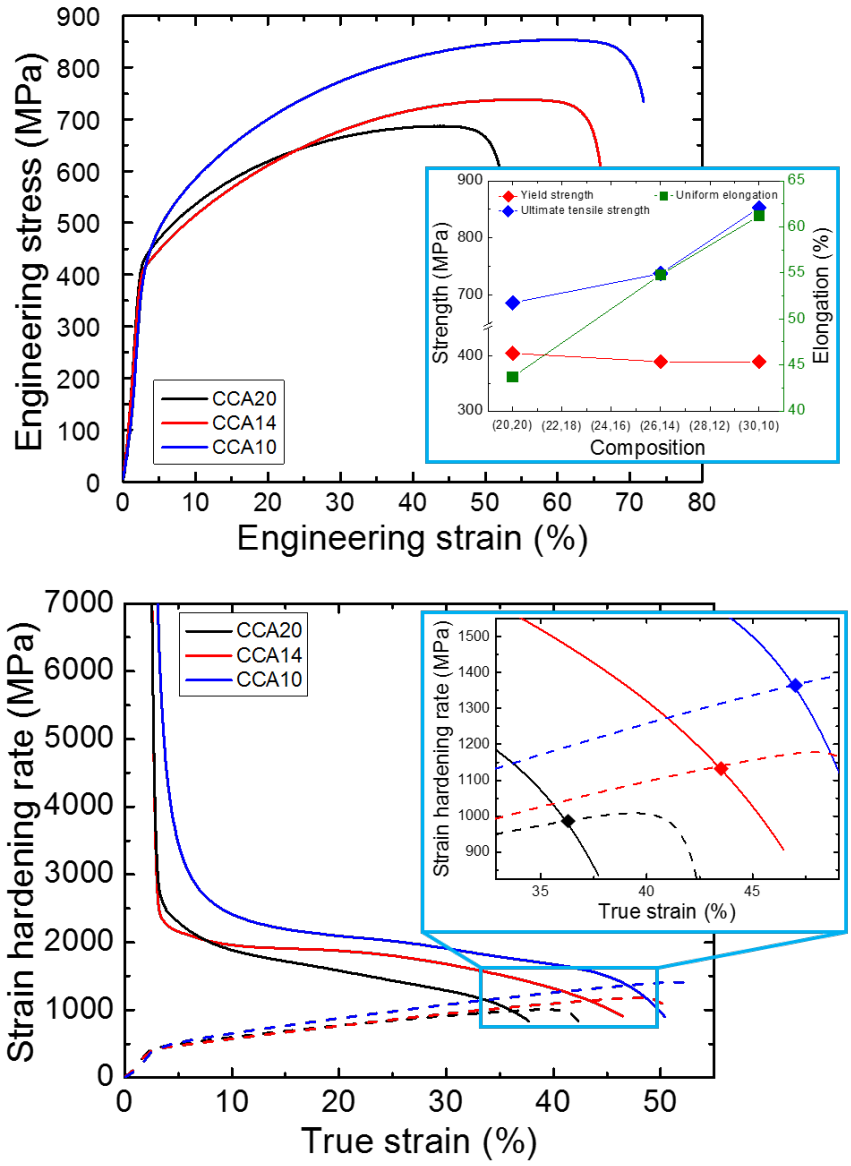


**Figure 7.6.** Comparison of mechanical behaviors between designed CCAs. (A) Typical engineering stress-strain curves; the inset shows the changes in yield strength, ultimate tensile strength, and uniform elongation values of present CCAs. (B) Strain hardening for the same group of alloys.

## 7.4. Microstructural analysis

The significant improvement of the ultimate tensile strength and strain-hardening rate of the developed CCAs is associated with the strengthening mechanisms active in the new CCAs. We reveal this in the following paragraphs by means of correlative EBSD (Figure 7.7) and ECCI (Figure 7.8 and Figure 7.9) analyses. The EBSD phase maps (Figure 7.7) show that twinning was induced in CCA14 and martensitic transformation from the FCC to the HCP phase was induced in CCA10 upon strain loading, acting as primary deformation mechanisms in each CCA. This is consistent with our prediction of SFE in Section 6.1, which holds that the SFE decreases in the order of CCA20, CCA14, and CCA10. Because the EBSD has a resolution of 50 nm, further deformation substructures are analyzed using ECCI observation.

At the early stage of deformation of CCA14, the microstructure mainly consists of dislocation substructures, with very few deformation twins. Parts (a) and (b) in the figure show ECCI images of the deformed microstructure of CCA14 at 15% engineering strain. The micrographs revealed that fewer than 20% of all grains contain deformation twins, which are mainly distributed along a single active twinning system. At this stage of deformation, dislocations randomly arranged as indicated in Figure 7.8. One can observe that dislocations piled up at the twin boundaries, which is evidence of the twin-induced plasticity mechanism in CCA14. In the middle of the stage (30% true strain), the twinning activity increases remarkably, leading to the development of a well-defined twin substructure. At this stage, most of the grains contain deformation twins that are active in several systems. As the strain increases (up to 60% of the true strain), the twin thickness increases to

the extent that EBSD can characterize the twins. Thus, the strain hardening decreases at this stage.

The fraction of the transformed HCP phase in CCA10 increases from 0 to 50 at 60% deformation. Other than the transformed HCP phase, we also observe in the ECCI analysis high numbers of stacking faults in the FCC phase at the early stage of deformation. The low density of dislocations in Figure 7.9 implies that the stacking fault is the effective deformation units inhibiting dislocation motion, resulting in a higher strain rate. The stacking faults observed in the retained non-transformed FCC phase show a crystallographic orientation similar to that of the newly formed HCP phase (Figure 7.9A and B). This is consistent with previous observations of other FCC-HCP TRIP alloys, specifically that thin stacking fault plates consisting of only a few several atomic monolayers of an HCP structure act as the nuclei of the HCP martensite phase [128, 130]. Furthermore, Figure 7.9D shows the stacking fault traces after martensitic transformation and the dislocations which accumulate at the boundaries, resulting in the additional strain hardening in this CCA.

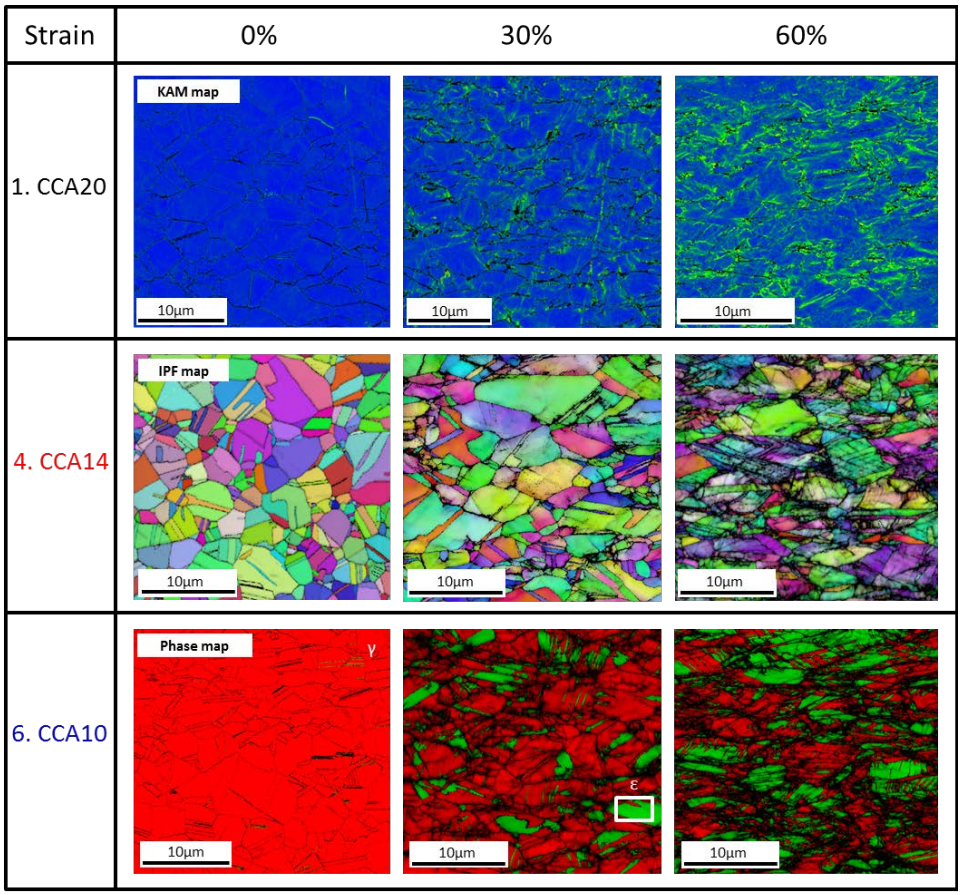


**Figure 7.7.** EBSD maps of present CCAs with increasing tensile deformation at room temperature. (A) The main deformation mechanisms of CCA20 is the dislocation glide as shown in KAM maps. (B) The main deformation mechanisms of CCA14 is TWIP as shown in IPF maps. (C) The main deformation mechanisms of CCA10 is TRIP as shown in phase maps.

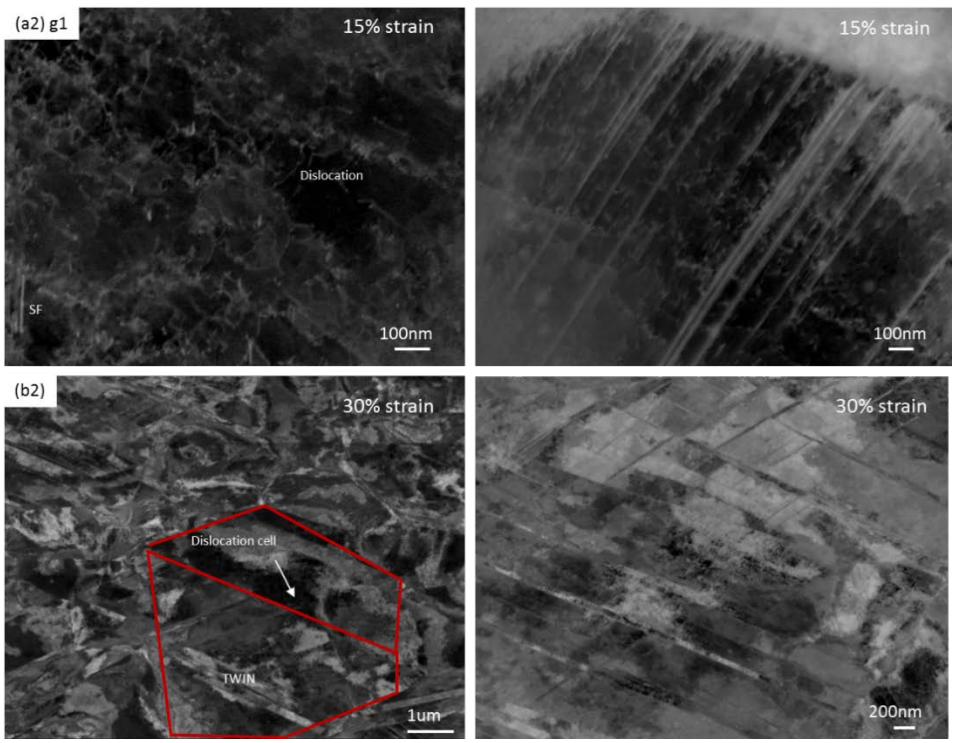


**Figure 7.8.** ECCI analysis of the CCA14 revealing deformation induced twin, stacking faults and dislocations at the local strain levels of (A) 15% and (b) 30%, respectively.

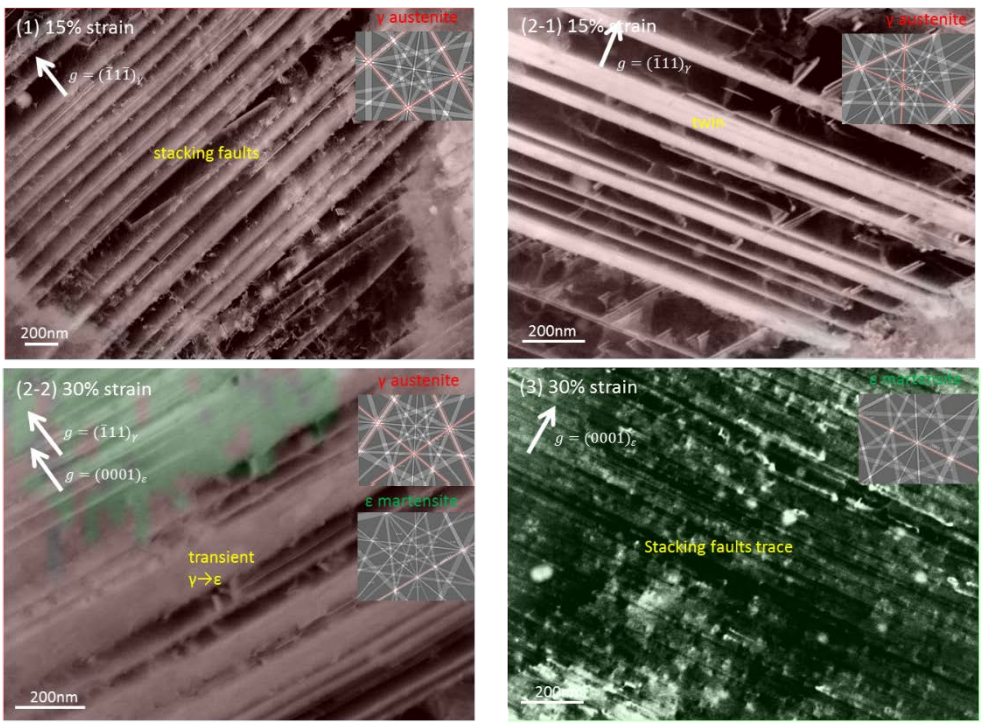


**Figure 7.9.** ECCI analysis of the CCA10 revealing deformation induced (A) stacking faults and twins at the local strain level of 15%, and (B) martensitic transformation and stacking fault traces at the local strain level of 30%, respectively.

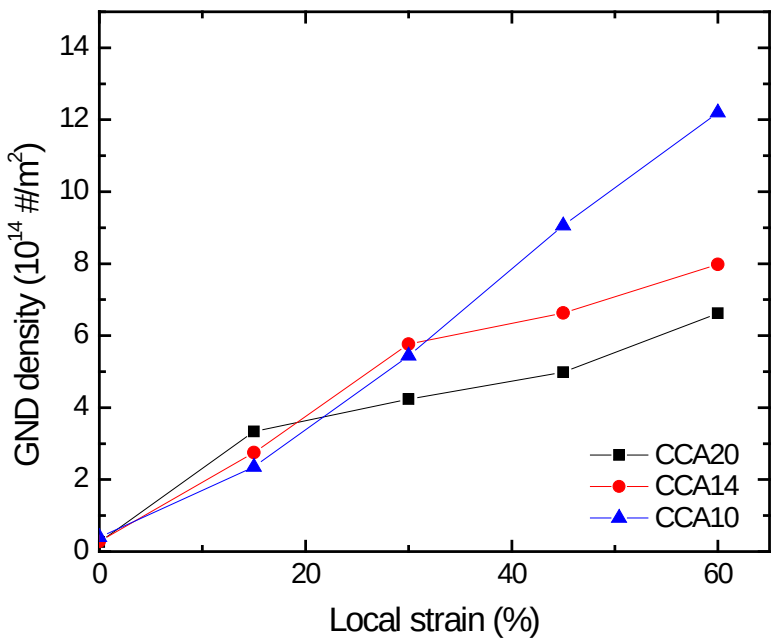


**Figure 7.10.** Geometrically necessary dislocation densities of current CCAs upon local strain levels.

## 7.5. Summary

In this chapter, a new series of 3d CCAs are developed to show that there are many factors that we can manipulate besides complexity from the deviation of atomic-level pressure. Changing the composition from the Cantor alloy, we developed TWIP and TRIP CCAs by decreasing stacking fault energies and maintaining the solid-solution strengthening parameter established in Chapter 6. When all other conditions, such as grain sizes, are made equal, the developed CCAs have the similar yield strengths as the Cantor alloy even if the composition changes by 40%. This implies that these CCAs have the similar complexity of atomic-level pressure. The change of deformation mechanisms from dislocation gliding (CCA20) to TWIP (CCA14) and TRIP (CCA10) increase the strain hardening rate of the CCAs, increasing both of UTS and uniform elongation. This overcoming strength-ductility trade-off occurs within the consistent complexity of atomic-level pressure, clearly showing the importance of considering synergetic effects of consisting elements for the development of a new CCA. Thus, we concluded that chemical complexity, which increase the vastness of composition space, is also important for the design of new CCAs in terms of the freedom in manipulating composition.

# Chapter 8. Asymmetry of the atomic-level pressure-induced element-specific properties in CCAs

Chapters 5~7 discuss how to describe and manipulate the atomic-level complexity of a CCA to provide a guideline for the tailor-made design of new CCAs. We proposed that the deviation of the atomic-level pressure is the origin of the elastic strain energy of the system, resulting in complexity-linked properties such as solid-solution strengthening, lattice distortion, and low transport properties.

In this chapter, we found that the properties related to the atomic-level pressure of CCAs have asymmetrical characteristics which originate from the anharmonicity of the lattice potential energy. This results in different characteristics of each element depending on the atomic-level pressure, including the lattice distortion, the diffusivity, and the solubility of the interstitial solute elements, which are critical for engineering applications. Asymmetry of the atomic-level pressure-induced properties in CCAs is discussed based on simulated results and on a literature review. First, we analyze the asymmetry of atomic displacement depending on atomic-level pressure and discuss the lattice rigidity. Using this concept, we discuss the elemental specific properties related to the lattice rigidity, which are the diffusivity and the preferential sites of interstitial elements. We expect that this research can provide important future research goals pertaining to CCAs from both scientific and engineering points of view. Anharmonicity of the lattice potential is known to affect the behavior of metallic liquids [136-141]. This marks first report to reveal the effects of the anharmonicity of the lattice potential on the properties of CCAs to the best of our knowledge.

## 8.1. Asymmetry of the lattice distortion and atomic-level pressure

The lattice distortion effect of a CCA is discussed in Section 2.2 and Chapter 5. In a dilute alloy, a solute atom is always surrounded by solvent atoms and is fixed at its original lattice position. In this case, lattice distortion occurs due to solvent atoms (Figure 8.1A). In a CCA, all constituent elements are displaced from their original lattice sites (Figure 8.1B). Thus, the sizes of atomic displacements are related to the elastic energy of the system; i.e., atomic-level pressure and the lattice distortion are expected to offer important clues related to the atomic environment of CCAs.

We calculated the atomic displacements of dilute Fe-95 at.%Ni (dilute FeNi, Figure 8.1C) and equiatomic FeNi (Figure 8.1D) by DFT calculations (as described in Section 4.4). The atomic-level pressure values of Fe in dilute FeNi are close to 250 GPa and are one order of magnitude larger than those in equiatomic FeNi. This is due to the large charge transfer between the surrounding Ni to Fe in the dilute FeNi. Atomic displacements of Fe in dilute FeNi are less than 0.05 Å. This shows that in dilute FeNi, the environments surrounding Fe atoms are symmetric with Ni atoms and Fe atoms are fixed at their ideal lattice positions. On the other hand, the atomic displacements of Fe in equiatomic FeNi are close to 0.06 Å, and some parts are even larger than 0.10 Å. Thus, the difference in the atomic displacements between these two alloys clearly shows that the atomic-level pressure of CCAs reflects the fluctuation of the local environments and is related to the atomic displacements, unlike in dilute alloys.

Meanwhile, we found that there is asymmetry of the atomic displacements in

equiatomic FeNi. As shown in Figure 8.1D, the atomic displacements of Fe are larger than those of Ni. In order to observe this trend more clearly, we calculated the atomic displacements of all 3d CCAs from Ni to CrMnFeCoNi (Table 5.1). Figure 8.2A shows the relationship between the DFT calculated atomic displacements and the charge transfers, i.e., the atomic-level pressure, of 3d CCAs. The atomic displacements increase in the order of Ni, Co, Fe, Mn, and Cr, even with fluctuations, consistent with previously reported results [16, 142]. This shows that atomic displacements increase with a decrease in the charge transfer, i.e., atomic-level pressure. Figure 8.2B describes the relationship between the atomic displacements, the atomic-level pressure, and the atomic volume of CrMnFeCoNi CCA. All types of atomic displacements (average, fluctuation, and mean squared) increase with a decrease in the atomic-level pressure. However, this trend does not follow the average atomic volume. This again shows that the classical elastic point of view cannot be applied to CCAs, as discussed in Chapter 6.

The asymmetry of the atomic displacements in 3d CCAs comes from the anharmonicity of the interatomic potential [143]. When the interatomic distance between a central atom and surrounding atoms is longer than the minimum position of the interatomic potential (Figure 8.2C), the atoms attract each other to shorten the bond length and the atomic-level pressure becomes negative according to Eq. 3-10. In this case, the slope of the potential is small and the bond is soft. This indicates that atoms with negative (tensile) pressures can be displaced well by fluctuations in the local environments. On the other hand, when the interatomic distance between a central atom and surrounding atoms is shorter than the minimum position of the interatomic potential (Figure 8.2D), the atoms repulse each other to increase the bond length and the atomic-level pressure becomes positive according to Eq. 3-10. In this

case, the slope of the potential is larger and the bond is rigid, indicating that atoms with positive (compressive) pressures cannot readily be displaced by fluctuations in the local environments. Thus, the average atomic-level pressure of a specific element represents the overall size of the slope of the interatomic potential between the element and the surrounding elements and thus the stiffness of the bond of the element.

Figure 8.3 shows the fluctuation of the bond length of each bond in CrMnFeCoNi CCA in Table 5.6 and the averaged atomic-level pressure of the two elements. The clear trend of the decreasing fluctuation of the bond length against the averaged atomic-level pressure shows that the atomic-level pressure is the signature of the resistance of an element to displacement from its original position. Cr-Cr bonds have the largest fluctuation (3.06 %) and the largest negative averaged atomic-level pressure (-33.0 GPa). Thus, both Cr elements can easily be displaced by fluctuations in the local environments. Ni-Ni bonds have the smallest amounts of fluctuation (0.89 %) and the largest positive averaged atomic-level pressure (37.7 GPa). This stems from the strong tendency of Ni with large positive pressure to be fixed at its original position. Ni-Cr bonds have medium fluctuation (1.38 %) as well as an intermediate averaged atomic-level pressure (2.4 GPa). Thus, the atomic-level pressure can be used as a parameter to indicate the tendency of the displacement of an element, i.e., the lattice rigidity.

In order to investigate the physical meaning of the size of the lattice distortion, we compared the atomic displacements of CoNi and CrMnFeCoNi, as indicated in Figure 8.4A. Both mean values and fluctuation of atomic displacements of CrMnFeCoNi are larger than those of CoNi. Figure 8.4B is the schematic diagram showing the relationship between the atomic-level pressure and the atomic

displacements in CCAs. The fluctuation of the atomic-level pressure is related to the degree of atomic displacements, i.e., the lattice distortion, by two factors. First, the atomic-level pressure is a signature of the fluctuation of the local environment. The mean size and the fluctuation of the atomic displacements would increase with an increase in fluctuation of atomic-level pressure. Second, the atomic-level pressure includes information about the anharmonicity of the lattice potential and the rigidity of the lattice depends on the atomic-level pressure. Great fluctuation of the atomic-level pressure implies that some elements have large negative atomic pressure. The elements with large negative atomic-level pressure are easily displaced, thus increasing the amount of lattice distortion. This means that the degree of lattice distortion increases with an increase in the fluctuation of atomic-level pressure. Figure 8.4C shows the mean squared atomic displacements (MSAD) of 3d CCAs against the standard deviation of the atomic-level pressure ($\sigma(P)$). The MSAD value increases with an increase in $\sigma(P)$. However, except for CoNi with a small MSAD (0.012 Å) and CrMnCoNi with a large MSAD (0.067 Å), the increasing trend is not obvious. Thus, the size of the lattice distortion is related to the fluctuation of the atomic-level pressure. However, this relationship is not strict, and one should carefully use the lattice distortion concept in conjunction with the atomic-level complexity of a CCA.

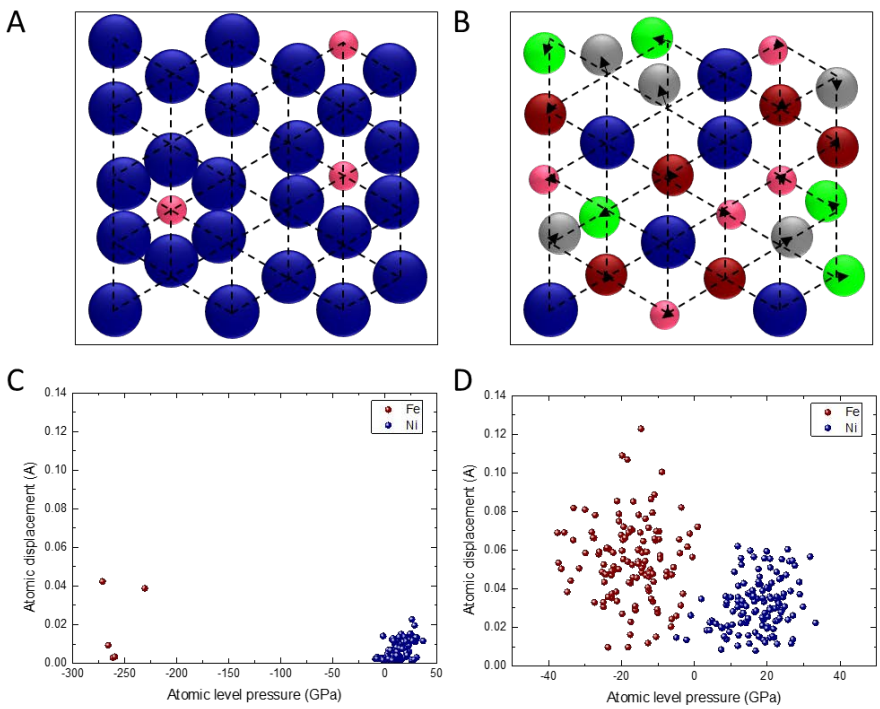


**Figure 8.1.** (A-B) Schematic diagrams showing the lattice distortion of (A) a dilute alloy (B) a CCA. (C-D) DFT calculation results showing the relationship between atomic-level pressure and atomic displacement in (C) Fe-95 at.%Ni, and (D) Equiatomic FeNi.

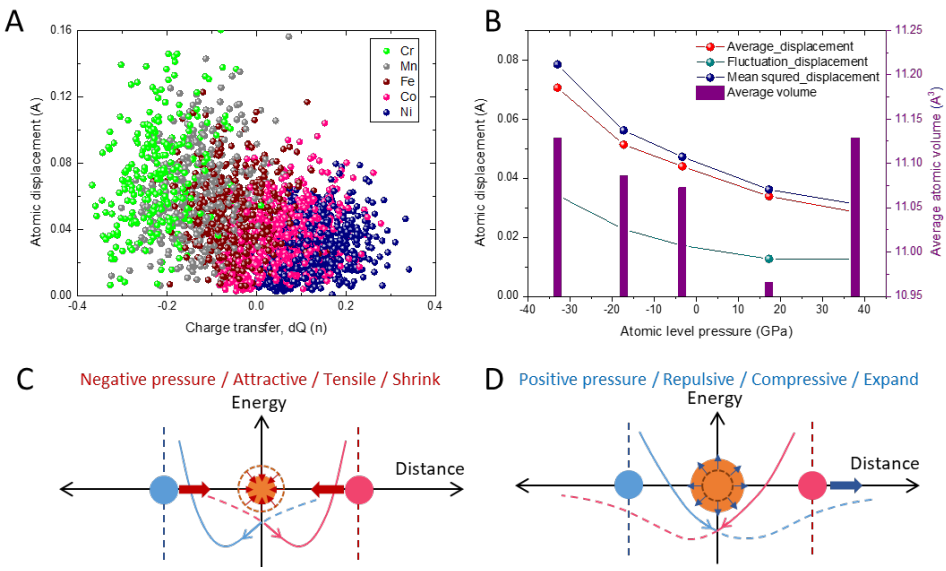


**Figure 8.2.** Asymmetry of atomic displacement in 3d CCAs. (A) Atomic displacements and charge transfer of 3d CCAs. (B) Atomic displacement, average atomic volume, and atomic-level pressure of CrMnFeCoNi CCA. (C-D) Schematic diagram showing anharmonicity of interatomic potential. (C) Negative pressure with small slope of potential. (D) Positive pressure with large slope of potential.

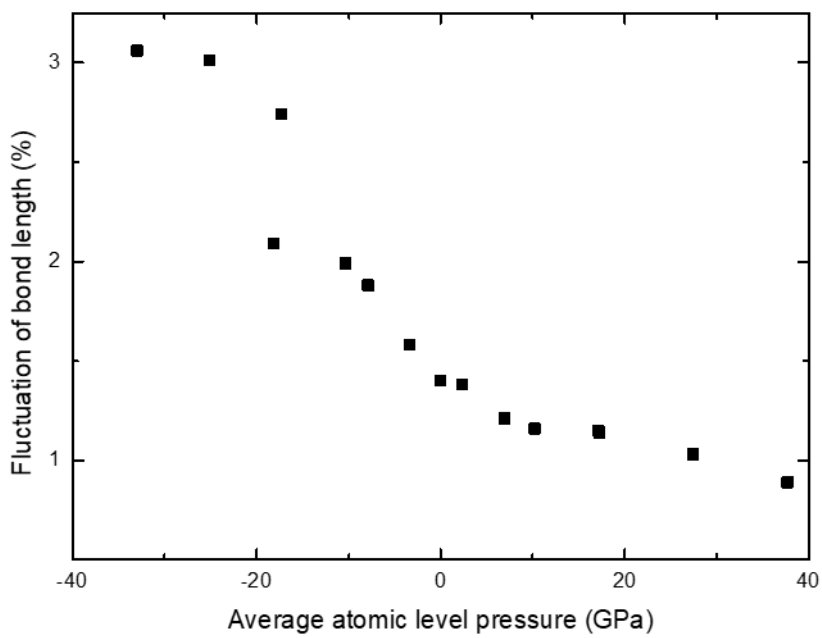


**Figure 8.3.** Fluctuation of each bond length in CrMnFeCoNi in Table 5.6, plotted against average of averaged atomic-level pressure.

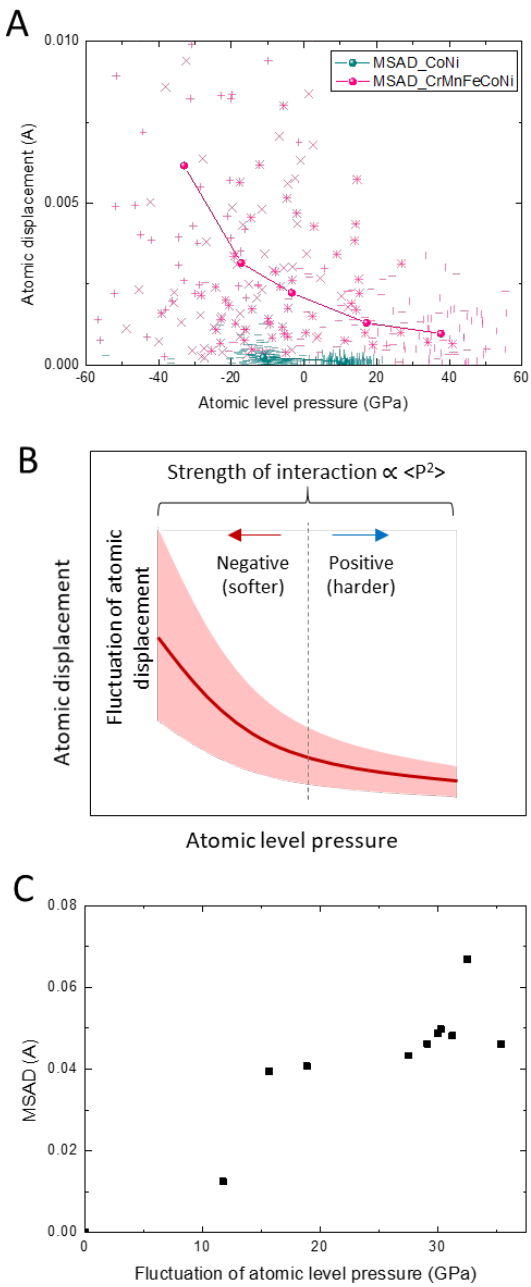


**Figure 8.4.** The relationship between fluctuation of atomic-level pressure and lattice distortion. (A) Atomic displacement and atomic-level pressure of CoNi and CrMnFeCoNi. (B) Schematic diagram showing the relationship between atomic-level pressure and atomic displacement. (C) Mean squared atomic displacement and fluctuation of atomic-level pressure.

## 8.2. Diffusivity of substitutional elements and the atomic-level pressure

The diffusivity of a specific element is affected by the chemical interaction (cohesive energy), elastic interaction, and packing density (See Section 2.3). Because the atomic-level pressure of an element reflects the tendency toward displacement, the atomic-level pressure represents the elastic contribution of the lattice on the diffusivity. Figure 8.5 shows the diffusivity of each element in CrMnFeCoNi CCA [27, 58]. The diffusivity increases in the order of Ni, Co, Fe, Cr, and Mn throughout the temperature range. This indicates that the diffusivity increases in the order of the average atomic-level pressure of the consisting elements, although the positions of Cr and Mn are reversed. Elements with negative atomic-level pressures (Cr, Mn) can easily jump to the nearest vacant site, resulting in high diffusivity. On the other hand, elements with positive atomic-level pressure (Co, Ni) do not readily jump to the nearest vacant site, resulting in the low diffusivity.

This trend is also observable in the serration behavior during tensile testing at high temperatures [17]. As shown in Figure 8.6, CCAs with Cr or Mn show serrated behavior in the high-temperature region (473 ~ 673 K). This dynamic strain aging is known to come from the formation of a Cottrell atmosphere near the dislocation core due to the diffusion of solutes [63, 144, 145]. In CCAs, elements with negative atomic-level pressure have high diffusivity and can easily form a short-range order and Cottrell atmosphere near dislocations. Although previous studies focusing on the Cottrell atmosphere have focused on the size of the solutes [146], the atomic-level pressure mainly affects the diffusivity of the solutes and the stress field near dislocations.

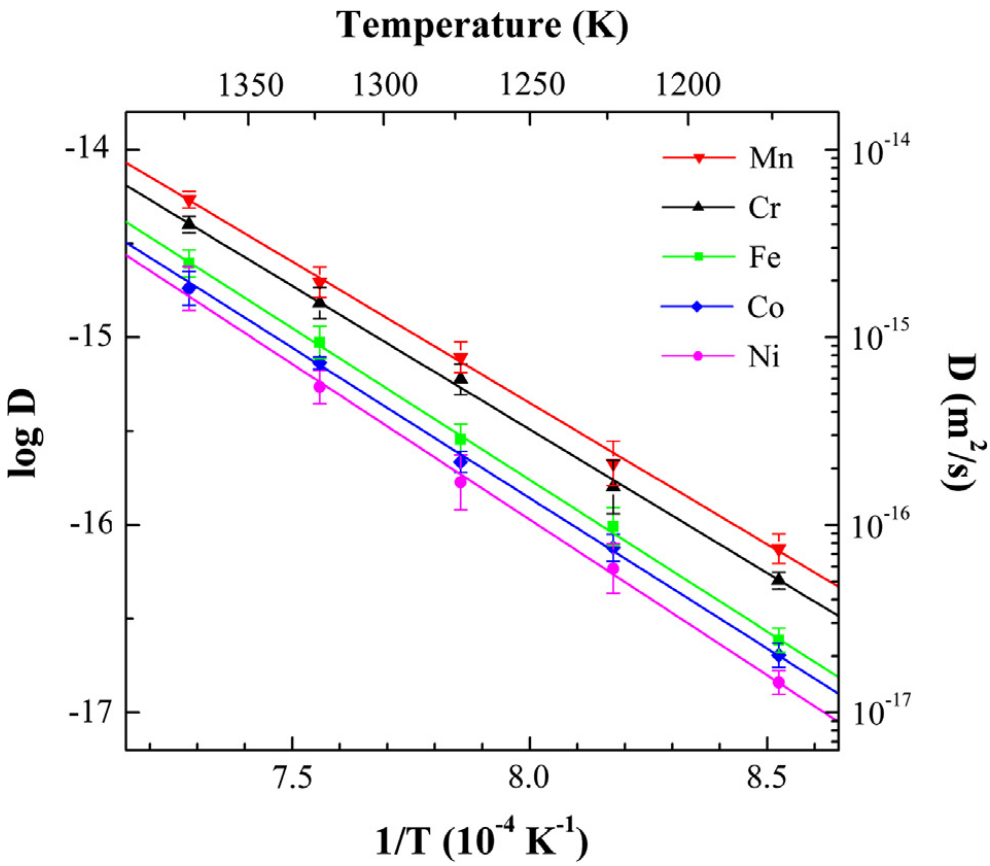


**Figure 8.5.** Temperature dependent diffusivity of each element in CrMnFeCoNi CCA. Reprinted from [27] with permission through "Copyright Clearance Center".

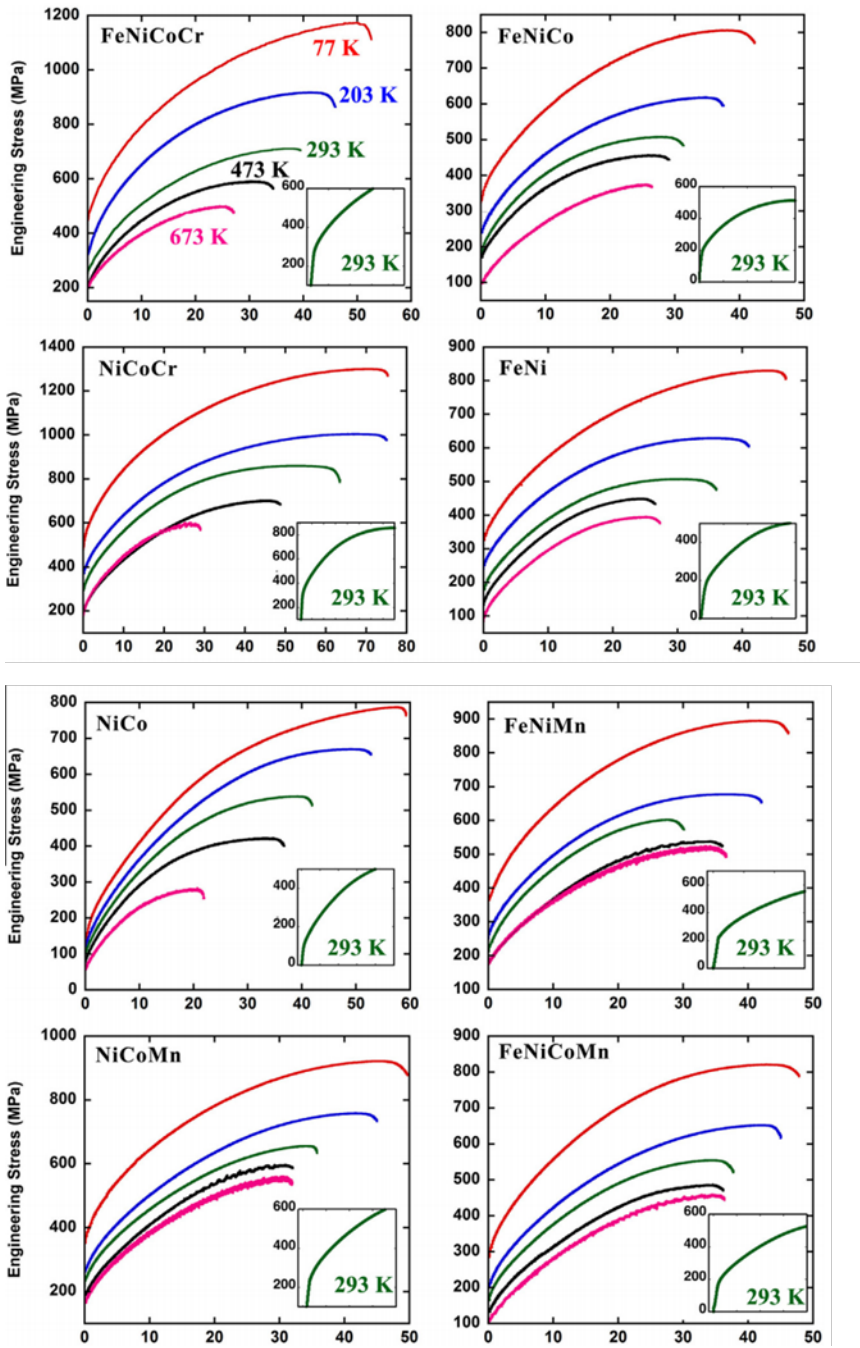


**Figure 8.6.** Temperature dependent tensile behavior of 3d CCAs. CCAs with Cr or Mn shows the serrated behavior during deformation. Reprinted from [17] with permission through “Copyright Clearance Center”.

## 8.3. Preferential site of interstitial solute elements and atomic-level pressure

Alloying an interstitial element is one of the most effective means by which to enhance the properties of alloys [147, 148]. Carbon (C) or nitrogen (N) can significantly increase the strength and ductility of austenitic steels by solid-solution strengthening [92, 149-151] and by changing the stacking fault energy with regard to plasticity mechanisms [131, 152]. Interstitial solutes occasionally have detrimental effects on alloys, such as hydrogen (H) embrittlement [153-160]. Research on the effects of interstitial solutes is also beginning to take place in relation to CCAs [161-168]. Dual-phase non-equiatomic FeMnCoCr with C showed enhanced properties of both the strength and ductility by multiple deformation mechanisms [161]. Hydrogen in CrMnFeCoNi CCA showed enhanced mechanical properties rather than undergoing catastrophic weakening due to hydrogen embrittlement [162]. Thus, understanding the fundamental aspects of interstitial elements in CCAs is crucial for the development of CCAs for engineering applications.

Changes of the local atomic structures by interstitial solutes can be measured in EXAFS experiments [169-171]. Oddershede et al. [171] showed that N atoms tend to become trapped by Cr atoms in expanded austenitic stainless steel (FeNiCr STS) AISI 316. They investigated the local structures of unnitrided, nitrided, and denitrided FeNiCr STS foils by EXAFS experimentation (Figure 8.7). Figure 8.7 shows the pseudo-radial distribution function (pRDF) of unnitrided, nitride and denitrided STS. After nitriding, the degree of the peak shift, i.e., the distortion of the nearest neighbor, increases in the order of Ni, Fe, and Cr. This means that the

introduction of N leads to the greater distortions of the local environment of Cr as compared to those of Ni and Fe. In the denitrited FeNiCr STS, the Fe and Ni peaks recovered back to their original position. This indicates that N atoms near Fe and Ni are removed during the denitriding process. The peak of Cr did not change after denitriding indicating that N atoms cannot be removed and are trapped by Cr atoms.

The preferential site of an interstitial element is usually explained in terms of the chemical affinity, e.g. Mn and C [172]. In addition to the traditional opinions, we propose an additional explanation of this phenomenon using the atomic-level pressure and the lattice rigidity. In the FeNiCr STS, Cr would have negative atomic-level pressure due to its low electronegativity. Thus, Cr may be easy to move to position N atoms at the nearest-neighbor positions. On the other hand, Fe and Ni would have positive atomic-level pressures and would be difficult to move. Thus, N atoms are preferably placed near Cr atoms, increasing the degree of short-range ordering.

The lattice rigidity of CCAs would be related to the solubility of interstitial elements. If the fluctuation of the atomic-level pressure is large, the portion of atoms with large negative atomic-level pressure would increase; i.e. more atoms can easily be displaced and act as trapping sites. As a result, the solubility of interstitial elements would increase and the diffusivity would decrease, which is beneficial for CCAs in engineering applications, e.g., hydrogen embrittlement. Therefore, a better understanding of local atomic environments in a CCA in terms of the atomic-level pressure is crucial for utilizing it with interstitial solutes.

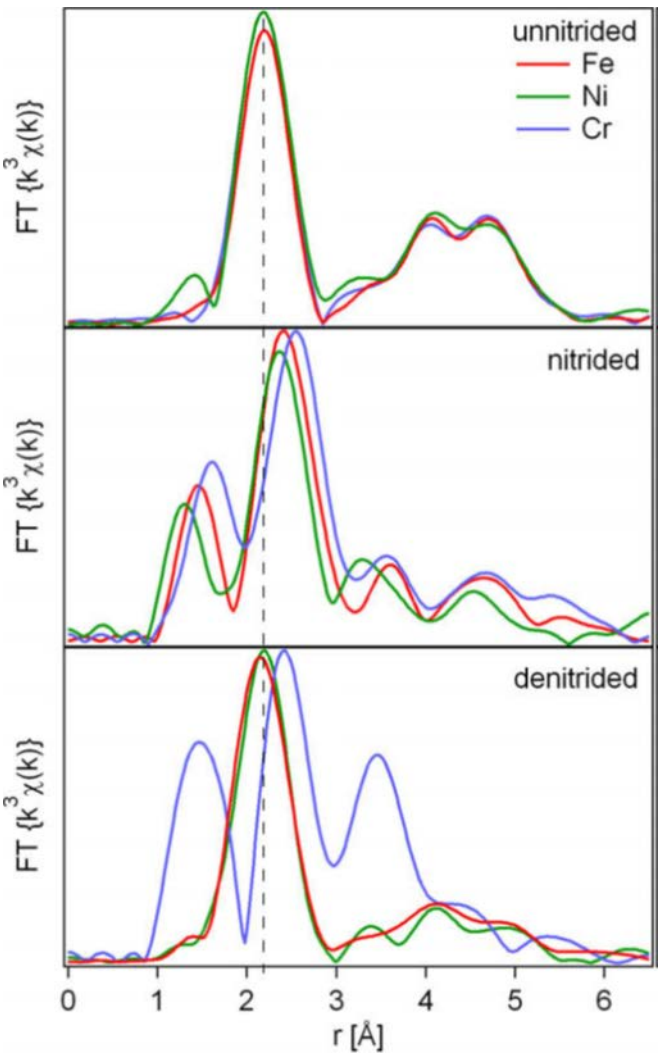


**Figure 8.7.** pRDF of the unnitrided, nitride and dendrited FeNiCr STS. Reprinted from [171] with permission through “Copyright Clearance Center”.

## 8.4. Summary

In this chapter, the asymmetric behaviors of properties induced by the atomic-level pressure are discussed. The atomic-level pressure includes information about the anharmonicity of the lattice potential. Atoms with positive pressures cannot easily be displaced from their ideal lattice positions, while atoms with negative pressures can easily be displaced. This asymmetry of the lattice rigidity on the atomic-level pressure results in element-specific properties, such as atomic displacements, diffusivity, and preferential sites of interstitial elements. As a result, fluctuations of the atomic-level pressure affect the degree of lattice distortion, the diffusivity of substitutional elements, and the solubility of interstitial elements. Therefore, it is essential to understand the local atomic environments in CCAs in terms of the atomic-level pressure for both scientific and engineering purposes.

# Chapter 9. Conclusions and outlook

In order to make a useful guide for designing new CCAs, a comprehensive research on the atomic-level complexity of 3d CCAs is conducted in this study. We first investigated a parameter that describes the local structure of CCAs using atomic-level pressure concept which can be directly related to the core properties of CCAs. We successfully developed new CCAs with outstanding mechanical properties by utilizing the found parameter.

We started by analyzing the local structure of equiatomic 3d CCAs by EXAFS to measure the elemental average atomic sizes of consisting elements. Within the structural information, we predicted the solid-solution strengths by applying the atomic size difference among the constituting elements to the existing model based on the elasticity theory. However, the calculated solid-solution strengths from the structural information do not match with the experimentally measured ones. In order to interpret this mismatch, we calculated the atomic structure of CrMnFeCoNi CCA using DFT and compared the local fluctuation of bond lengths (configurational deviation) and the deviation of macroscopic mean bond lengths of each element (elemental deviation). As a result, the local fluctuations are an order of magnitude larger than the deviation of mean values, indicating that the fluctuation of local bond lengths due to the difference in atomic configurations should not be ignored for the prediction of solid-solution strengthening. We defined the different degrees of complexity in CCAs, which are ‘the difference in the element-specific average property among two (or more) elements in solid solution’ and ‘the variations around the average due to dissimilar local atomic environments (configurations) in one element’. This is considered to be a major feature that distinguishes CCA from

existing dilute alloys.

An atomic-level pressure concept is applied to describe the local complexity of 3d CCAs and the resultant solid-solution strengthening effect. Because 3d CCAs consist of elements with similar atomic sizes, the volume strain, i.e., the atomic-level pressure, and the resultant solid-solution strengthening effects originate from the charge transfer induced by the electronegativity difference. In addition, through a statistical approach, we found that both values of 'difference in average elemental atomic-level pressure' and 'difference in atomic-level pressure due to the variance in local atomic configurations' have fixed ratios of $\sqrt{6}$. This makes it possible to estimate a higher degree complexity (configurational deviations) using a lower level of complexity (elemental deviations), which can be identified experimentally. Based on these criteria, an electronegativity diagram was constructed to clarify the solid-solution strengthening effects in 3d CCAs. The concept of the electronegativity diagram can be applied not only to the solid-solution strengthening, but also to the general properties which result from the fluctuations of local potential energies, such as sluggish diffusion, transport properties, and lattice distortion, among others. Thus, we concluded that deviation of atomic-level pressure can be an indicator of atomic-level complexity and its influence on complexity induced properties of CCAs.

It can be argued that the chemical complexity is no longer important for CCAs as the deviation of atomic-level pressure is related to the lattice distortion effect and the sluggish diffusion effect, which are CCA's two 'core effects' known to be induced by atomic-level complexity. Changing the composition from the Cantor alloy, we developed TWIP and TRIP CCAs by decreasing stacking fault energies and maintaining the solid-solution strengthening parameter to show that there are many factors that we can manipulate besides complexity induced by the deviation of

atomic-level pressure. As a result, the change in deformation mechanisms from dislocation glide to TWIP and TRIP increase the strain hardening rate of the CCAs, enhancing both ultimate tensile strength and the percentage of uniform elongation. The development of these new CCAs was possible due to the freedom in manipulating composition, which implies that both complexities of atomic-level pressure and chemical complexity contribute to the precise design of new CCAs.

In addition, due to the anharmonicity of the lattice potential, atoms with positive pressures cannot easily be displaced from their ideal lattice positions, while atoms with negative pressures can easily be displaced. This asymmetry of the lattice rigidity on the atomic-level pressure results in element-specific properties, such as atomic displacements, diffusivity, and preferential sites of interstitial elements. This means that the concept of atomic-level pressure can be used to interpret the element-specific properties of CCAs. Therefore, it is essential to understand the local atomic environments in CCAs in terms of the atomic-level pressure for both scientific and engineering purposes.

In conclusion, we distinguished the previous concept of complexity in CCAs into two different complexities: chemical complexity and complexity of atomic-level pressure. We believe that the tailor-made design of CCAs is possible when both complexities are investigated well for the desired elemental combinations.

# Bibliography

[1] Y. Zhang, T.T. Zuo, Z. Tang, M.C. Gao, K.A. Dahmen, P.K. Liaw, Z.P. Lu, Microstructures and properties of high-entropy alloys, Progress in Materials Science 61 (2014) 1-93.

[2] J.W. Yeh, S.K. Chen, S.J. Lin, J.Y. Gan, T.S. Chin, T.T. Shun, C.H. Tsau, S.Y. Chang, Nanostructured high‐entropy alloys with multiple principal elements: novel alloy design concepts and outcomes, Advanced Engineering Materials 6(5) (2004) 299-303.

[3] B. Gludovatz, A. Hohenwarter, D. Catoor, E.H. Chang, E.P. George, R.O. Ritchie, A fracture-resistant high-entropy alloy for cryogenic applications, Science 345(6201) (2014) 1153-1158.

[4] B. Gludovatz, A. Hohenwarter, K.V. Thurston, H. Bei, Z. Wu, E.P. George, R.O. Ritchie, Exceptional damage-tolerance of a medium-entropy alloy CrCoNi at cryogenic temperatures, Nature communications 7 (2016) 10602.

[5] Y. Chen, T. Duval, U. Hung, J. Yeh, H. Shih, Microstructure and electrochemical properties of high entropy alloys—a comparison with type-304 stainless steel, Corrosion science 47(9) (2005) 2257-2279.

[6] O. Senkov, G. Wilks, J. Scott, D. Miracle, Mechanical properties of Nb 25 Mo 25 Ta 25 W 25 and V 20 Nb 20 Mo 20 Ta 20 W 20 refractory high entropy alloys, Intermetallics 19(5) (2011) 698-706.

[7] Y. Lu, Y. Dong, S. Guo, L. Jiang, H. Kang, T. Wang, B. Wen, Z. Wang, J. Jie, Z. Cao, A promising new class of high-temperature alloys: eutectic high-entropy alloys, Scientific reports 4 (2014) 6200.

[8] Y. Zhang, G.M. Stocks, K. Jin, C. Lu, H. Bei, B.C. Sales, L. Wang, L.K. Béland, R.E. Stoller, G.D. Samolyuk, Influence of chemical disorder on energy dissipation and defect evolution in concentrated solid solution alloys, Nature communications 6 (2015) 8736.

[9] F. Granberg, K. Nordlund, M.W. Ullah, K. Jin, C. Lu, H. Bei, L. Wang, F. Djurabekova, W. Weber, Y. Zhang, Mechanism of radiation damage reduction in equiatomic multicomponent single phase alloys, Physical review letters 116(13) (2016) 135504.

[10] T. Egami, W. Guo, P. Rack, T. Nagase, Irradiation resistance of multicomponent alloys, Metallurgical and Materials Transactions A 45(1) (2014) 180-183.

[11] C. Lu, L. Niu, N. Chen, K. Jin, T. Yang, P. Xiu, Y. Zhang, F. Gao, H. Bei, S. Shi, Enhancing radiation tolerance by controlling defect mobility and migration

pathways in multicomponent single-phase alloys, Nature communications 7 (2016) 13564.

[12] S. Gorsse, D.B. Miracle, O.N. Senkov, Mapping the world of complex concentrated alloys, Acta Materialia (2017).

[13] Y. Ye, Q. Wang, J. Lu, C. Liu, Y. Yang, High-entropy alloy: challenges and prospects, Materials Today 19(6) (2016) 349-362.

[14] D. Miracle, O. Senkov, A critical review of high entropy alloys and related concepts, Acta Materialia 122 (2017) 448-511.

[15] L.R. Owen, E.J. Pickering, H.Y. Playford, H.J. Stone, M.G. Tucker, N.G. Jones, An assessment of the lattice strain in the CrMnFeCoNi high-entropy alloy, Acta Materialia 122 (2017) 11-18.

[16] N.L. Okamoto, K. Yuge, K. Tanaka, H. Inui, E.P. George, Atomic displacement in the CrMnFeCoNi high-entropy alloy–A scaling factor to predict solid solution strengthening, AIP Advances 6(12) (2016) 125008.

[17] Z. Wu, H. Bei, G.M. Pharr, E.P. George, Temperature dependence of the mechanical properties of equiatomic solid solution alloys with face-centered cubic crystal structures, Acta Materialia 81 (2014) 428-441.

[18] T. Egami, Atomic level stresses, Progress in Materials Science 56(6) (2011) 637-653.

[19] O. Senkov, D. Miracle, A new thermodynamic parameter to predict formation of solid solution or intermetallic phases in high entropy alloys, Journal of Alloys and Compounds 658 (2016) 603-607.

[20] O. Senkov, J. Miller, D. Miracle, C. Woodward, Accelerated exploration of multi-principal element alloys with solid solution phases, Nature communications 6 (2015).

[21] D. King, S. Middleburgh, A. McGregor, M. Cortie, Predicting the formation and stability of single phase high-entropy alloys, Acta Materialia 104 (2016) 172-179.

[22] M.C. Troparevsky, J.R. Morris, P.R. Kent, A.R. Lupini, G.M. Stocks, Criteria for predicting the formation of single-phase high-entropy alloys, Physical Review X 5(1) (2015) 011041.

[23] H.S. Oh, D. Ma, G.P. Leyson, B. Grabowski, E.S. Park, F. Körmann, D. Raabe, Lattice distortions in the FeCoNiCrMn high entropy alloy studied by theory and experiment, Entropy 18(9) (2016) 321.

[24] G. Laplanche, J. Bonneville, C. Varvenne, W. Curtin, E.P. George, Thermal activation parameters of plastic flow reveal deformation mechanisms in the CrMnFeCoNi high-entropy alloy, Acta Materialia 143 (2018) 257-264.

[25] C. Varvenne, A. Luque, W.A. Curtin, Theory of strengthening in fcc high entropy alloys, Acta Materialia 118 (2016) 164-176.

[26] Z. Wu, Y. Gao, H. Bei, Thermal activation mechanisms and Labusch-type strengthening analysis for a family of high-entropy and equiatomic solid-solution alloys, Acta Materialia 120 (2016) 108-119.

[27] K.-Y. Tsai, M.-H. Tsai, J.-W. Yeh, Sluggish diffusion in Co–Cr–Fe–Mn–Ni high-entropy alloys, Acta Materialia 61(13) (2013) 4887-4897.

[28] S.-Y. Chang, C.-E. Li, Y.-C. Huang, H.-F. Hsu, J.-W. Yeh, S.-J. Lin, Structural and thermodynamic factors of suppressed interdiffusion kinetics in multi-component high-entropy materials, Scientific reports 4 (2014).

[29] M.-H. Tsai, Physical Properties of High Entropy Alloys, Entropy 15(12) (2013) 5338-5345.

[30] E.J. Pickering, N.G. Jones, High-entropy alloys: a critical assessment of their founding principles and future prospects, International Materials Reviews 61(3) (2016) 183-202.

[31] M.-H. Tsai, J.-W. Yeh, High-Entropy Alloys: A Critical Review, Materials Research Letters 2(3) (2014) 107-123.

[32] H.K.D.H. Bhadeshia, High entropy alloys, Materials Science and Technology 31(10) (2015) 1139-1141.

[33] R. Kozak, A. Sologubenko, W. Steurer, Single-phase high-entropy alloys – an overview, Zeitschrift für Kristallographie - Crystalline Materials 230(1) (2015).

[34] X. Yang, Y. Zhang, Prediction of high-entropy stabilized solid-solution in multi-component alloys, Materials Chemistry and Physics 132(2-3) (2012) 233-238.

[35] S. Guo, Q. Hu, C. Ng, C.T. Liu, More than entropy in high-entropy alloys: Forming solid solutions or amorphous phase, Intermetallics 41 (2013) 96-103.

[36] S. Guo, C.T. Liu, Phase stability in high entropy alloys: Formation of solid-solution phase or amorphous phase, Progress in Natural Science: Materials International 21(6) (2011) 433-446.

[37] F. Otto, Y. Yang, H. Bei, E.P. George, Relative effects of enthalpy and entropy on the phase stability of equiatomic high-entropy alloys, Acta Materialia 61(7) (2013) 2628-2638.

[38] D.J.M. King, S.C. Middleburgh, A.G. McGregor, M.B. Cortie, Predicting the formation and stability of single phase high-entropy alloys, Acta Materialia 104 (2016) 172-179.

[39] Y. Zhang, Z.P. Lu, S.G. Ma, P.K. Liaw, Z. Tang, Y.Q. Cheng, M.C. Gao, Guidelines in predicting phase formation of high-entropy alloys, MRS

Communications 4(02) (2014) 57-62.

[40] Y. Zhang, Y.J. Zhou, J.P. Lin, G.L. Chen, P.K. Liaw, Solid-Solution Phase Formation Rules for Multi-component Alloys, Advanced Engineering Materials 10(6) (2008) 534-538.

[41] L.M. Martyushev, V.D. Seleznev, Maximum entropy production principle in physics, chemistry and biology, Physics Reports 426(1) (2006) 1-45.

[42] A.L. Greer, Confusion by design, Nature 366 (1993) 303.

[43] D. Ma, B. Grabowski, F. Körmann, J. Neugebauer, D. Raabe, Ab initio thermodynamics of the CoCrFeMnNi high entropy alloy: Importance of entropy contributions beyond the configurational one, Acta Materialia 100 (2015) 90-97.

[44] J.-W. Yeh, S.-Y. Chang, Y.-D. Hong, S.-K. Chen, S.-J. Lin, Anomalous decrease in X-ray diffraction intensities of Cu–Ni–Al–Co–Cr–Fe–Si alloy systems with multi-principal elements, Materials Chemistry and Physics 103(1) (2007) 41-46.

[45] Y.J. Zhou, Y. Zhang, F.J. Wang, G.L. Chen, Phase transformation induced by lattice distortion in multiprincipal component CoCrFeNiCuxAl1－x solid-solution alloys, Applied Physics Letters 92(24) (2008) 241917.

[46] H. Diao, L.J. Santodonato, Z. Tang, T. Egami, P.K. Liaw, Local Structures of High-Entropy Alloys (HEAs) on Atomic Scales: An Overview, Jom 67(10) (2015) 2321-2325.

[47] W. Guo, W. Dmowski, J.-Y. Noh, P. Rack, P.K. Liaw, T. Egami, Local Atomic Structure of a High-Entropy Alloy: An X-Ray and Neutron Scattering Study, Metallurgical and Materials Transactions A 44(5) (2012) 1994-1997.

[48] Z. Wang, W. Qiu, Y. Yang, C.T. Liu, Atomic-size and lattice-distortion effects in newly developed high-entropy alloys with multiple principal elements, Intermetallics 64 (2015) 63-69.

[49] Y.F. Ye, C.T. Liu, Y. Yang, A geometric model for intrinsic residual strain and phase stability in high entropy alloys, Acta Materialia 94 (2015) 152-161.

[50] I. Toda-Caraballo, P.E. Rivera-Díaz-del-Castillo, Modelling solid solution hardening in high entropy alloys, Acta Materialia 85 (2015) 14-23.

[51] T. Egami, M. Ojha, O. Khorgolkhuu, D. Nicholson, G. Stocks, Local electronic effects and irradiation resistance in high-entropy alloys, Jom 67(10) (2015) 2345-2349.

[52] H. Song, F. Tian, Q.-M. Hu, L. Vitos, Y. Wang, J. Shen, N. Chen, Local lattice distortion in high-entropy alloys, Physical Review Materials 1(2) (2017).

[53] W.H. Liu, Y. Wu, J.Y. He, T.G. Nieh, Z.P. Lu, Grain growth and the Hall–Petch relationship in a high-entropy FeCrNiCoMn alloy, Scripta Materialia 68(7) (2013)

526-529.

[54] T. Yang, S. Xia, S. Liu, C. Wang, S. Liu, Y. Fang, Y. Zhang, J. Xue, S. Yan, Y. Wang, Precipitation behavior of AlxCoCrFeNi high entropy alloys under ion irradiation, Scientific reports 6 (2016).

[55] C.-J. Tong, Y.-L. Chen, J.-W. Yeh, S.-J. Lin, S.-K. Chen, T.-T. Shun, C.-H. Tsau, S.-Y. Chang, Microstructure characterization of Al x CoCrCuFeNi high-entropy alloy system with multiprincipal elements, Metallurgical and Materials Transactions A 36(4) (2005) 881-893.

[56] C. Ng, S. Guo, J. Luan, S. Shi, C.T. Liu, Entropy-driven phase stability and slow diffusion kinetics in an Al0.5CoCrCuFeNi high entropy alloy, Intermetallics 31 (2012) 165-172.

[57] S.Y. Chang, C.E. Li, Y.C. Huang, H.F. Hsu, J.W. Yeh, S.J. Lin, Structural and thermodynamic factors of suppressed interdiffusion kinetics in multi-component high-entropy materials, Sci Rep 4 (2014) 4162.

[58] K.Y. Tsai, M.H. Tsai, J.W. Yeh, Sluggish diffusion in Co–Cr–Fe–Mn–Ni high-entropy alloys, Acta Materialia 61(13) (2013) 4887-4897.

[59] M. Vaidya, S. Trubel, B.S. Murty, G. Wilde, S.V. Divinski, Ni tracer diffusion in CoCrFeNi and CoCrFeMnNi high entropy alloys, Journal of Alloys and Compounds 688 (2016) 994-1001.

[60] M. Vaidya, K.G. Pradeep, B.S. Murty, G. Wilde, S.V. Divinski, Radioactive isotopes reveal a non sluggish kinetics of grain boundary diffusion in high entropy alloys, Sci Rep 7(1) (2017) 12293.

[61] S.C. Middleburgh, D.M. King, G.R. Lumpkin, M. Cortie, L. Edwards, Segregation and migration of species in the CrCoFeNi high entropy alloy, Journal of Alloys and Compounds 599 (2014) 179-182.

[62] J.D. Eshelby, The determination of the elastic field of an ellipsoidal inclusion, and related problems, Proceedings of the Royal Society of London A: Mathematical, Physical and Engineering Sciences, The Royal Society, 1957, pp. 376-396.

[63] A.H. Cottrell, B. Bilby, Dislocation theory of yielding and strain ageing of iron, Proceedings of the Physical Society. Section A 62(1) (1949) 49.

[64] F. Nabarro, The theory of solution hardening, Philosophical magazine 35(3) (1977) 613-622.

[65] N. Mott, F.N. Nabarro, An attempt to estimate the degree of precipitation hardening, with a simple model, Proceedings of the Physical Society 52(1) (1940) 86.

[66] R. Fleisgher, Solution hardening, Acta metallurgica 9(11) (1961) 996-1000.

[67] R. Fleischer, Substitutional solution hardening, Acta metallurgica 11(3) (1963) 203-209.

[68] R. Labusch, A statistical theory of solid solution hardening, physica status solidi (b) 41(2) (1970) 659-669.

[69] J. Friedel, R. Smoluchowski, Les dislocations, Physics Today 10 (1957) 36.

[70] P. Jax, P. Kratochvil, P. Haasen, Solid solution hardening of gold and other fcc single crystals, Acta Metallurgica 18(2) (1970) 237-245.

[71] C. Varvenne, G. Leyson, M. Ghazisaeidi, W. Curtin, Solute strengthening in random alloys, Acta Materialia 124 (2017) 660-683.

[72] G.P.M. Leyson, W.A. Curtin, L.G. Hector Jr, C.F. Woodward, Quantitative prediction of solute strengthening in aluminium alloys, Nature materials 9(9) (2010) 750-755.

[73] G. Leyson, W. Curtin, Friedel vs. Labusch: the strong/weak pinning transition in solute strengthened metals, Philosophical Magazine 93(19) (2013) 2428-2444.

[74] A. Argon, Strengthening mechanisms in crystal plasticity, Oxford University Press on Demand2008.

[75] T. Egami, D. Srolovitz, Local structural fluctuations in amorphous and liquid metals: a simple theory of the glass transition, Journal of Physics F: Metal Physics 12(10) (1982) 2141.

[76] V. Vitek, T. Egami, Atomic level stresses in solids and liquids, physica status solidi (b) 144(1) (1987) 145-156.

[77] D. Nicholson, M. Ojha, T. Egami, First-principles local stress in crystalline and amorphous metals, Journal of Physics: Condensed Matter 25(43) (2013) 435505.

[78] M. Newville, IFEFFIT : interactive XAFS analysis and FEFF fitting, Journal of Synchrotron Radiation 8(2) (2001) 322-324.

[79] M. Newville, Fundamentals of XAFS, Reviews in Mineralogy and Geochemistry 78(1) (2014) 33-74.

[80] D.C. Joy, D.E. Newbury, D.L. Davidson, Electron channeling patterns in the scanning electron microscope, Journal of Applied Physics 53(8) (1982) R81-R122.

[81] I. Gutierrez-Urrutia, S. Zaefferer, D. Raabe, Coupling of Electron Channeling with EBSD: Toward the Quantitative Characterization of Deformation Structures in the SEM, Jom 65(9) (2013) 1229-1236.

[82] I. Gutierrez-Urrutia, S. Zaefferer, D. Raabe, Electron channeling contrast imaging of twins and dislocations in twinning-induced plasticity steels under controlled diffraction conditions in a scanning electron microscope, Scripta

Materialia 61(7) (2009) 737-740.

[83] S. Zaefferer, N.-N. Elhami, Theory and application of electron channelling contrast imaging under controlled diffraction conditions, Acta Materialia 75 (2014) 20-50.

[84] G. Kresse, J. Furthmüller, Efficiency of ab-initio total energy calculations for metals and semiconductors using a plane-wave basis set, Computational materials science 6(1) (1996) 15-50.

[85] G. Kresse, J. Furthmüller, Efficient iterative schemes for ab initio total-energy calculations using a plane-wave basis set, Physical review B 54(16) (1996) 11169.

[86] J.P. Perdew, K. Burke, M. Ernzerhof, Generalized gradient approximation made simple, Physical review letters 77(18) (1996) 3865.

[87] P.E. Blöchl, Projector augmented-wave method, Physical Review B 50(24) (1994) 17953-17979.

[88] G. Kresse, D. Joubert, From ultrasoft pseudopotentials to the projector augmented-wave method, Physical Review B 59(3) (1999) 1758.

[89] A. Zunger, S. Wei, L.G. Ferreira, J.E. Bernard, Special quasirandom structures, Phys Rev Lett 65(3) (1990) 353-356.

[90] P. Haasen, Physical Metallurgy, Cambridge University Press, 1996.

[91] D. Hull, D.J. Bacon, Introduction to dislocations, Butterworth-Heinemann2001.

[92] P.M. Anderson, J.P. Hirth, J. Lothe, Theory of Dislocations, Cambridge University Press2017.

[93] I. Toda-Caraballo, A general formulation for solid solution hardening effect in multicomponent alloys, Scripta Materialia 127 (2017) 113-117.

[94] H. King, Quantitative size-factors for metallic solid solutions, Journal of Materials Science 1(1) (1966) 79-90.

[95] V. Lubarda, On the effective lattice parameter of binary alloys, Mechanics of Materials 35(1) (2003) 53-68.

[96] D.-H. Finkler, A. Maurer, S. Campbell, T. Heck, U. Gonser, Precision determination of the lattice parameters of CuAuFe alloys, Physica B+ C 145(3) (1987) 335-341.

[97] N. Chetty, M. Weinert, T.S. Rahman, J.W. Davenport, Vacancies and impurities in aluminum and magnesium, Physical Review B 52(9) (1995) 6313-6326.

[98] N. Papanikolaou, R. Zeller, P. Dederichs, N. Stefanou, Lattice distortion in Cu-based dilute alloys: A first-principles study by the KKR Green-function method, Physical Review B 55(7) (1997) 4157.

[99] N. Papanikolaou, R. Zeller, P. Dederichs, N. Stefanou, Ab initio study of structural distortion and its influence on the magnetic properties of metallic dilute alloys, Computational materials science 8(1-2) (1997) 131-135.

[100] T. Uesugi, M. Kohyama, M. Kohzu, K. Higashi, Ab initio calculation on the structure and elastic properties of a magnesium-lithium alloy, Materials Transactions 42(7) (2001) 1167-1171.

[101] T. Uesugi, Y. Takigawa, K. Higashi, Deformation mechanism of nanocrystalline Al-Fe alloys by analysis from ab-initio calculations, Materials Science Forum, Trans Tech Publ, 2006, pp. 209-214.

[102] Y. Inoue, T. Uesugi, Y. Takigawa, K. Higashi, First-Principles Studies on Grain Boundary Energies of [110] Tilt Grain Boundaries in Aluminum, Materials Science Forum, Trans Tech Publ, 2007, pp. 1837-1840.

[103] T. Wang, L.-Q. Chen, Z.-K. Liu, Lattice Parameters and Local Lattice Distortions in fcc-Ni Solutions, Metallurgical and Materials Transactions A 38(3) (2007) 562-569.

[104] J. Zander, R. Sandström, L. Vitos, Modelling mechanical properties for non-hardenable aluminium alloys, Computational Materials Science 41(1) (2007) 86-95.

[105] S. Ganeshan, S.L. Shang, Y. Wang, Z.K. Liu, Effect of alloying elements on the elastic properties of Mg from first-principles calculations, Acta Materialia 57(13) (2009) 3876-3884.

[106] D. Kim, S.-L. Shang, Z.-K. Liu, Effects of alloying elements on elastic properties of Ni by first-principles calculations, Computational Materials Science 47(1) (2009) 254-260.

[107] G.P.M. Leyson, L.G. Hector, W.A. Curtin, Solute strengthening from first principles and application to aluminum alloys, Acta Materialia 60(9) (2012) 3873-3884.

[108] D. Ma, M. Friák, J. von Pezold, J. Neugebauer, D. Raabe, Ab initio study of compositional trends in solid solution strengthening in metals with low Peierls stresses, Acta Materialia 98 (2015) 367-376.

[109] D. Ma, M. Friák, J. von Pezold, D. Raabe, J. Neugebauer, Computationally efficient and quantitatively accurate multiscale simulation of solid-solution strengthening by ab initio calculation, Acta Materialia 85 (2015) 53-66.

[110] Z. Wu, H. Bei, F. Otto, G.M. Pharr, E.P. George, Recovery, recrystallization, grain growth and phase stability of a family of FCC-structured multi-component equiatomic solid solution alloys, Intermetallics 46 (2014) 131-140.

[111] L. Vegard, Die konstitution der mischkristalle und die raumfüllung der atome,

Zeitschrift für Physik 5(1) (1921) 17-26.

[112] T. Uesugi, K. Higashi, First-principles studies on lattice constants and local lattice distortions in solid solution aluminum alloys, Computational Materials Science 67 (2013) 1-10.

[113] U. Scheuer, B. Lengeler, Lattice distortion of solute atoms in metals studied by x-ray-absorption fine structure, Physical Review B 44(18) (1991) 9883.

[114] F. Otto, A. Dlouhý, K.G. Pradeep, M. Kuběnová, D. Raabe, G. Eggeler, E.P. George, Decomposition of the single-phase high-entropy alloy CrMnFeCoNi after prolonged anneals at intermediate temperatures, Acta Materialia 112 (2016) 40-52.

[115] J. Ding, Y. Cheng, Charge transfer and atomic-level pressure in metallic glasses, Applied Physics Letters 104(5) (2014) 051903.

[116] N.N. Greenwood, A. Earnshaw, Chemistry of the Elements, 2nd ed., Elsevier1997.

[117] Y. Zhao, T. Yang, Y. Tong, J. Wang, J. Luan, Z. Jiao, D. Chen, Y. Yang, A. Hu, C. Liu, Heterogeneous precipitation behavior and stacking-fault-mediated deformation in a CoCrNi-based medium-entropy alloy, Acta Materialia 138 (2017) 72-82.

[118] Z. Zhang, M. Mao, J. Wang, B. Gludovatz, Z. Zhang, S.X. Mao, E.P. George, Q. Yu, R.O. Ritchie, Nanoscale origins of the damage tolerance of the high-entropy alloy CrMnFeCoNi, Nature communications 6 (2015) 10143.

[119] Z. Zhang, H. Sheng, Z. Wang, B. Gludovatz, Z. Zhang, E.P. George, Q. Yu, S.X. Mao, R.O. Ritchie, Dislocation mechanisms and 3D twin architectures generate exceptional strength-ductility-toughness combination in CrCoNi medium-entropy alloy, Nature Communications 8 (2017).

[120] Z. Li, K.G. Pradeep, Y. Deng, D. Raabe, C.C. Tasan, Metastable high-entropy dual-phase alloys overcome the strength–ductility trade-off, Nature 534(7606) (2016) 227-230.

[121] R.O. Ritchie, The conflicts between strength and toughness, Nat Mater 10(11) (2011) 817-22.

[122] Y. Wei, Y. Li, L. Zhu, Y. Liu, X. Lei, G. Wang, Y. Wu, Z. Mi, J. Liu, H. Wang, H. Gao, Evading the strength-ductility trade-off dilemma in steel through gradient hierarchical nanotwins, Nat Commun 5 (2014) 3580.

[123] R.A. Hadfield, Hadfield's manganese steel, Science 12 (1888) 284-286.

[124] O. Grässel, L. Krüger, G. Frommeyer, L. Meyer, High strength Fe–Mn–(Al, Si) TRIP/TWIP steels development—properties—application, International Journal of plasticity 16(10) (2000) 1391-1409.

[125] C. Herrera, D. Ponge, D. Raabe, Design of a novel Mn-based 1GPa duplex stainless TRIP steel with 60% ductility by a reduction of austenite stability, Acta Materialia 59(11) (2011) 4653-4664.

[126] C.C. Tasan, M. Diehl, D. Yan, M. Bechtold, F. Roters, L. Schemmann, C. Zheng, N. Peranio, D. Ponge, M. Koyama, K. Tsuzaki, D. Raabe, An Overview of Dual-Phase Steels: Advances in Microstructure-Oriented Processing and Micromechanically Guided Design, Annual Review of Materials Research 45(1) (2015) 391-431.

[127] B.C. De Cooman, Y. Estrin, S.K. Kim, Twinning-induced plasticity (TWIP) steels, Acta Materialia 142 (2018) 283-362.

[128] G. Olson, M. Cohen, A general mechanism of martensitic nucleation: Part I. General concepts and the FCC→ HCP transformation, Metallurgical Transactions A 7(12) (1976) 1897-1904.

[129] D.T. Pierce, J.A. Jiménez, J. Bentley, D. Raabe, C. Oskay, J. Wittig, The influence of manganese content on the stacking fault and austenite/ε-martensite interfacial energies in Fe–Mn–(Al–Si) steels investigated by experiment and theory, Acta Materialia 68 (2014) 238-253.

[130] Y.-K. Lee, C. Choi, Driving force for γ→ ε martensitic transformation and stacking fault energy of γ in Fe-Mn binary system, Metallurgical and Materials Transactions A 31(2) (2000) 355-360.

[131] A. Saeed-Akbari, J. Imlau, U. Prahl, W. Bleck, Derivation and variation in composition-dependent stacking fault energy maps based on subregular solution model in high-manganese steels, Metallurgical and Materials Transactions A 40(13) (2009) 3076-3090.

[132] N.L. Okamoto, S. Fujimoto, Y. Kambara, M. Kawamura, Z.M. Chen, H. Matsunoshita, K. Tanaka, H. Inui, E.P. George, Size effect, critical resolved shear stress, stacking fault energy, and solid solution strengthening in the CrMnFeCoNi high-entropy alloy, Scientific reports 6 (2016) 35863.

[133] K. Ming, X. Bi, J. Wang, Microstructures and deformation mechanisms of Cr26Mn20Fe20Co20Ni14 alloys, Materials Characterization 134 (2017) 194-201.

[134] E. Demir, D. Raabe, N. Zaafarani, S. Zaefferer, Investigation of the indentation size effect through the measurement of the geometrically necessary dislocations beneath small indents of different depths using EBSD tomography, Acta Materialia 57(2) (2009) 559-569.

[135] L. Kubin, A. Mortensen, Geometrically necessary dislocations and strain-gradient plasticity: a few critical issues, Scripta materialia 48(2) (2003) 119-125.

[136] C. Bennett, D. Polk, D. Turnbull, Role of composition in metallic glass

formation, Acta Metallurgica 19(12) (1971) 1295-1298.

[137] R. Casalini, C.M. Roland, Why liquids are fragile, Physical review. E, Statistical, nonlinear, and soft matter physics 72(3 Pt 1) (2005) 031503.

[138] J. Mattsson, H.M. Wyss, A. Fernandez-Nieves, K. Miyazaki, Z. Hu, D.R. Reichman, D.A. Weitz, Soft colloids make strong glasses, Nature 462(7269) (2009) 83-6.

[139] K. Ngai, Relaxation and diffusion in complex systems, Springer Science & Business Media2011.

[140] J. Krausser, K.H. Samwer, A. Zaccone, Interatomic repulsion softness directly controls the fragility of supercooled metallic melts, Proceedings of the National Academy of Sciences 112(45) (2015) 13762-13767.

[141] C.E. Pueblo, M. Sun, K.F. Kelton, Strength of the repulsive part of the interatomic potential determines fragility in metallic liquids, Nat Mater 16(8) (2017) 792-796.

[142] Z. Wu, M. Troparevsky, Y. Gao, J. Morris, G. Stocks, H. Bei, Phase stability, physical properties and strengthening mechanisms of concentrated solid solution alloys, Current Opinion in Solid State and Materials Science (2017).

[143] D. Reith, M. Pütz, F. Müller- Plathe, Deriving effective mesoscale potentials from atomistic simulations, Journal of computational chemistry 24(13) (2003) 1624-1636.

[144] R.E. Reed-Hill, R. Abbaschian, R. Abbaschian, Physical metallurgy principles, Van Nostrand New York1973.

[145] J. Robinson, M. Shaw, Microstructural and mechanical influences on dynamic strain aging phenomena, International Materials Reviews 39(3) (1994) 113-122.

[146] Y. Wang, D. Srolovitz, J. Rickman, R. Lesar, Dislocation motion in the presence of diffusing solutes: a computer simulation study, Acta materialia 48(9) (2000) 2163-2175.

[147] V.G. Gavriljuk, Austenite and martensite in nitrogen-, carbon- and hydrogen-containing iron alloys: Similarities and differences, Materials Science and Engineering: A 438-440 (2006) 75-79.

[148] V.G. Gavriljuk, V.N. Shivanyuk, B.D. Shanina, Change in the electron structure caused by C, N and H atoms in iron and its effect on their interaction with dislocations, Acta Materialia 53(19) (2005) 5017-5024.

[149] K. Irvine, T. Gladman, F. Pickering, The strength of austenitic stainless steels, J Iron Steel Inst 207(7) (1969) 1017-1028.

[150] M. Byrnes, M. Grujicic, W. Owen, Nitrogen strengthening of a stable austenitic

stainless steel, Acta Metallurgica 35(7) (1987) 1853-1862.

[151] J. Simmons, Overview: high-nitrogen alloying of stainless steels, Materials Science and Engineering: A 207(2) (1996) 159-169.

[152] P. Brofman, G. Ansell, On the effect of carbon on the stacking fault energy of austenitic stainless steels, Metallurgical and Materials Transactions A 9(6) (1978) 879-880.

[153] C. Zapffe, C. Sims, Hydrogen embrittlement, internal stress and defects in steel, Trans. AIME 145(1941) (1941) 225-271.

[154] R. Oriani, Hydrogen embrittlement of steels, Annual review of materials science 8(1) (1978) 327-357.

[155] A.R. Troiano, The role of hydrogen and other interstitials in the mechanical behavior of metals, Metallography, Microstructure, and Analysis 5(6) (2016) 557-569.

[156] H.K. Birnbaum, P. Sofronis, Hydrogen-enhanced localized plasticity—a mechanism for hydrogen-related fracture, Materials Science and Engineering: A 176(1-2) (1994) 191-202.

[157] G. Lovicu, M. Bottazzi, F. D'Aiuto, M. De Sanctis, A. Dimatteo, C. Santus, R. Valentini, Hydrogen Embrittlement of Automotive Advanced High-Strength Steels, Metallurgical and Materials Transactions A 43(11) (2012) 4075-4087.

[158] K. Takai, H. Shoda, H. Suzuki, M. Nagumo, Lattice defects dominating hydrogen-related failure of metals, Acta Materialia 56(18) (2008) 5158-5167.

[159] I. Robertson, H. Birnbaum, An HVEM study of hydrogen effects on the deformation and fracture of nickel, Acta Metallurgica 34(3) (1986) 353-366.

[160] K. Takai, R. Watanuki, Hydrogen in trapping states innocuous to environmental degradation of high-strength steels, ISIJ international 43(4) (2003) 520-526.

[161] Z. Li, C.C. Tasan, H. Springer, B. Gault, D. Raabe, Interstitial atoms enable joint twinning and transformation induced plasticity in strong and ductile high-entropy alloys, Sci Rep 7 (2017) 40704.

[162] H. Luo, Z. Li, D. Raabe, Hydrogen enhances strength and ductility of an equiatomic high-entropy alloy, Sci Rep 7(1) (2017) 9892.

[163] Z. Wang, I. Baker, Z. Cai, S. Chen, J.D. Poplawsky, W. Guo, The effect of interstitial carbon on the mechanical properties and dislocation substructure evolution in Fe 40.4 Ni 11.3 Mn 34.8 Al 7.5 Cr 6 high entropy alloys, Acta Materialia 120 (2016) 228-239.

[164] N.D. Stepanov, D.G. Shaysultanov, R.S. Chernichenko, N.Y. Yurchenko, S.V.

Zherebtsov, M.A. Tikhonovsky, G.A. Salishchev, Effect of thermomechanical processing on microstructure and mechanical properties of the carbon-containing CoCrFeNiMn high entropy alloy, Journal of Alloys and Compounds 693 (2017) 394-405.

[165] N.D. Stepanov, N.Y. Yurchenko, M.A. Tikhonovsky, G.A. Salishchev, Effect of carbon content and annealing on structure and hardness of the CoCrFeNiMn-based high entropy alloys, Journal of Alloys and Compounds 687 (2016) 59-71.

[166] Z. Wu, C.M. Parish, H. Bei, Nano-twin mediated plasticity in carbon-containing FeNiCoCrMn high entropy alloys, Journal of Alloys and Compounds 647 (2015) 815-822.

[167] L.B. Chen, R. Wei, K. Tang, J. Zhang, F. Jiang, L. He, J. Sun, Heavy carbon alloyed FCC-structured high entropy alloy with excellent combination of strength and ductility, Materials Science and Engineering: A (2018).

[168] Z. Wang, I. Baker, Interstitial strengthening of a f.c.c. FeNiMnAlCr high entropy alloy, Materials Letters 180 (2016) 153-156.

[169] K. Oda, N. Kondo, K. Shibata, X-ray Absorption Fine Structure analysis of interstitial (C, N)-substitutional (Cr) complexes in austenitic stainless steels, ISIJ International 30(8) (1990) 625-631.

[170] J. Oddershede, T.L. Christiansen, K. Ståhl, M.A.J. Somers, Extended X-Ray Absorption Fine Structure Investigation of Carbon Stabilized Expanded Austenite and Carbides in Stainless Steel AISI 316, steel research international 82(10) (2011) 1248-1254.

[171] J. Oddershede, T.L. Christiansen, K. Ståhl, M.A.J. Somers, Extended X-ray absorption fine structure investigation of nitrogen stabilized expanded austenite, Scripta Materialia 62(5) (2010) 290-293.

[172] N.I. Medvedeva, M.S. Park, D.C. Van Aken, J.E. Medvedeva, First-principles study of Mn, Al and C distribution and their effect on stacking fault energies in fcc Fe, Journal of Alloys and Compounds 582 (2014) 475-482.

# Abstract in Korean

## 초 록

# 컴플렉스 고용 합금의 특성 맞춤형 합금 설계법 개발

오 현 석
서울대학교 공과대학
재료공학부

컴플렉스 고용 합금은 2원계 농축 합금부터 5성분계 이상의 원소가 유사한 비율로 혼합된 고농축 합금을 통칭하는 용어로써, 주원소에 소량의 첨가원소를 혼합하여 제조하는 전통적인 합금설계 패러다임에서 벗어난 새로운 종류의 고용체 합금을 의미한다. 이러한 컴플렉스 고용 합금은 극저온, 상온, 및 고온에서의 우수한 물성과 방사선 조사 환경에서의 우수한 저항성 등으로 인해, 기존의 합금들 수용하지 못했던 다양한 산업 환경에서 적용될 수 있을 것으로 기대가 되어, 활발한 개발 연구가 진행되고 있다.

현재까지 컴플렉스 고용 합금의 우수한 성능들은 다양한 원소들로 구성된 원자 단위 배열의 복잡성으로 인해 나타나는 것으로 알려져 있다. 이러한 국부적인 원자 배열의 복잡성은 높은 고용강화 효과, 격자 비틀림 효과, 낮은 확산 효과 등을 수반하여 합금의 우수한 성능에 기여하는 것으로 예측되고 있다. 하지만 현재까지는 이러한 원자 배열의 복잡성과 그로 인한 특성들의 상관관계가 밝혀지지 않은 상태로, 정량적인 특성 예측과 새로운 합금설계 전략으로 활용할 수는 없는 상황이다.

한편, 컴플렉스 고용 합금의 모든 원소는 용질 혹은 용매로 작용하며, 각 원소는 전위의 압력장과 상호작용을 하여 고용강화를 유발한다. 따라서 컴플렉스 고용 함금에서의 고용강화 효과는 이종 원소로 인해 발생하는 원자 단위 복잡성을 반영하는 대표적인 인자이며, 동시에 거시적 물성과 직접적으로 연관되는 특성이라는 점에서 심도 있는 연구가 요구되고 있다. 본 연구에서는 컴플렉스 고용 합금의 원자 단위 복잡성과 그로 인한 특성의 상관관계를 규명하고, 새로운 맞춤형 합금설계 전략으로 활용하고자 하였다. 특별히, 현재 가장 활발한 연구가 진행되고 있고, 철강, 니켈기 초합금 기지 등 상용합금들이 포함되어 있는, 3주기 전이원소 기반 컴플렉스 고용 합금군을 선정하여 체계적인 연구를 진행하였다.

먼저, 본 연구에서는 해당 합금들의 합금 내부의 각 원소의 평균 크기를 X-ray Diffraction(XRD)와 Extended X-ray Absorption Fine structure (EXAFS) 분석을 통해 측정하고 원소 간의 평균크기 차이를 계산하였다. 기존의 컴플렉스 고용 합금의 고용강화 이론에서는, 고전적인 탄성학적 관점에서 합금 내부의 원자 간 크기 차이가 고용강화를 유발하는 것으로 제시하고 있다. 하지만 본 연구에서 측정된 원소 간 평균 크기의 차이는 각 합금의 고용강화 경향성과 맞지 않았다. 이를 보완하기 위해 밀도함수이론 계산을 통하여 각 원자 간 크기 변화를 계산하였고, 같은 원소이더라도 주변의 원자배열에 따라 원자 크기가 변화하며, 이러한 편차는 각 원소 별 평균 크기의 편차보다 약 5~10배 이상 큰 것을 확인하였다. 이는 컴플렉스 고용 합금에서 복잡성을 '각 원소의 평균적인 특성과 그 특성의 편차로 인해 발생하는 복잡성' 과, '주변 원자배열의 차이로 인해 발생하는 복잡성' 의 두 단계로 구분하는 것이 필요함을 의미한다.

다음으로, 이러한 원자 간 크기 차이 및 압력장이 발생하는 원인을 파악하기 위해, 밀도함수이론 계산을 통해 각 원자에서 주변 환경으로의 전하 이동으로 인해 압력장이 발생함을 확인하였다. 이를 실험적으로 확인하기 위해, 합금화 이후 원자 크기를 순원소의 원자크기로 나누어

부피 변화율을 계산하였고, 이 부피변화율이 전기음성도로 계산된 전하 이동량과 비례함을 확인할 수 있었다. 이는 합금 내부에서 발생하는 원자 크기 변화와 압력장이, 탄성 상호작용보다는 전기적인 상호작용으로 인해 발생함을 의미하고, 고용강화 계산 시, 원소 간 크기 차이가 아닌 각 원소의 크기 변화를 고려해야 함을 의미한다.

이를 합금 설계의 측면에서 응용하기 위하여, 앞에서 정의한 2단계의 복잡성 측면에서, 복잡성의 단계를 감소할 수 있는지 여부를 확인하였다. 그 결과 합금의 평균 원소 압력장의 편차 (Difference in average elemental atomic pressure)와 각 원소 별 압력장 편차 (Difference in atomic-level pressure due to the variance in local atomic configurations) 가 약 $\sqrt{6}$의 크기 비율을 가짐을 확인하였다. 이는 컴플렉스 고용 합금에서 압력장에 기반하여 특성을 예측한다면, 원자배열의 복잡성을 고려하지 않더라도 각 원소의 평균적인 특성을 통해 합금 전체의 특성을 예측할 수 있다는 것을 의미한다. 이상의 내용들을 종합적으로 고려하여, 본 연구에서는 3주기 전이원소 기반 컴플렉스 고용 합금의 고용강화 효과와 구성원소 간 전기음성도 편차가 비례관계를 가짐을 확인할 수 있었다.

본 연구에서는 위의 발견에 기반하여 컴플렉스 고용 합금에서 원소 종류의 복잡성과 원자단위 압력의 복잡성 (즉, 고용강화) 의 상관관계를 보여주는 전기음성도-혼합엔트로피 도표를 제작하였다. 이를 위해 V, Cr, Mn, Fe, Co, Ni로 구성할 수 있는 모든 조합의 합금에서 전기음성도 편차를 계산하였고, FCC 상이 형성되는 조건인 원자가전자가 7.8이상의 합금들을 도표에 수록하였다. 수록된 합금들은 역 C자 형태의 경계선을 갖는 모양의 영역으로 도시가 되었다. 이는 1. 혼합엔트로피, 즉 원소의 종류 자체의 복잡성은 고용강화와 큰 상관관계를 갖지 않는다는 것과, 2. 더 높은 고용강화 효과를 얻기 위해서는 오히려 더 작은 혼합엔트로피를 갖는 합금 시스템을 설계해야 하는 것을 의미한다. 즉, 합금 시스템 내부의 원자 단위 압력의 복잡성은 원소 종류의 다양성 (화학적 복잡성)이 아닌 전기음성도의

편차로 결정된다는 결론을 얻었다.

이에, 컴플렉스 고용 합금에서 원소 종류의 다양성이 갖는 의미를 재확인하기 위하여 원자 단위 압력의 복잡성을 유지시킨 상태에서, 즉 일정한 고용강화를 갖는 합금들에서 나타날 수 있는 소성변형의 차이점을 고찰하였다. 이를 위해 CrMnFeCoNi 합금에서 조성변화를 통해 고용강화를 일정하게 유지하고 적층결함에너지가 감소된 합금들을 개발하였다. 개발된 합금들은 원 합금과 동일한 항복강도를 지니고 있지만, 각각 쌍정유기소성과 변태유기소성 특성을 통해 향상된 소성변형능과 인장강도를 보였다. 이러한 개발은 다양한 원소의 종류로 인해 조성 제어의 자유도가 높아 가능하였으며, 이는 컴플렉스 고용 합금의 개발 시 원소 종류의 다양성이 개발의 자유도 및 시너지 효과를 내는 요인으로서 여전히 중요함을 의미한다.

추가적으로, 본 연구에서는 원자의 압력장에 의해 원소별 비대칭성이 나타나는 특징들에 대하여 조사하였다. 격자 포텐셜에너지는 척력과 인력의 비조화성이 있기 때문에 압력장의 부호는 격자의 비조화성 정보를 함유하고 있다. 이에 원소 별 격자비틀림, 원소별 확산계수, 그리고 침입형 고용체의 원소 선호도는 원자의 압력장으로 표현할 수 있고, 압력장의 편차는 합금의 격자비틀림의 총량, 확산 효과, 그리고 침입형 고용체의 고용도에 주된 영향을 줄 수 있음을 제시하였다.

결론적으로, 본 연구에서는 컴플렉스 고용 합금에서 기존에 제시되었던 복잡성의 개념을 합금 설계의 자유도를 의미하는 ‘원소 종류의 다양성’과 미시 단위에서 구조 및 응력 분포의 복잡성을 나타내는 ‘원자 단위 압력의 복잡성’으로 분리하였고, 3주기 전이원소계열 합금에서 위 두 가지 복잡성을 활용하여 합금 개발을 수행하였다. 결론적으로, 컴플렉스 고용 합금의 맞춤형 합금 설계는, 목표로 하는 원소들의 조합에서 상기 두 가지 복잡성들을 종합적으로 파악하였을 때 가능하며, 앞으로도 다양한 시스템에서 많은 연구가 필요하다고 사료된다.